Examining Topological Insulators and Topological Semimetals Using First Principles Calculations

John W. D. Villanova

Dissertation submitted to the Faculty of the
Virginia Polytechnic Institute and State University
in partial fulfillment of the requirements for the degree of

Doctor of Philosophy
in
Physics

Kyungwha Park, Chair
Sophia Economou
Jean J. Heremans
Chenggang Tao

March 19, 2018
Blacksburg, Virginia

Keywords: density functional theory, topological insulators, Dirac semimetals, Weyl semimetals, Wannier functions

Examining Topological Insulators and Topological Semimetals Using First Principles Calculations

John W. D. Villanova

(ABSTRACT)

The importance and promise that topological materials hold has been recently underscored by the award of the Nobel Prize in Physics in 2016 "for theoretical discoveries of topological phase transitions and topological phases of matter." This dissertation explores the novel qualities and useful topologically protected surface states of topological insulators and semimetals.

Topological materials have protected qualities which are not removed by weak perturbations. The manifestations of these qualities in topological insulators are spin-momentum-locked surface states, and in Weyl and Dirac semimetals they are unconventional open surface states (Fermi arcs) with anomalous electrical transport properties. There is great promise in utilizing the topologically protected surface states in electronics of the future, including spintronics, quantum computers, and highly sensitive devices. Physicists and chemists are also interested in the fundamental physics and exotic fermions exhibited in topological materials and in heterostructures including them.

Chapter 1 provides an introduction to the concepts and methods of topological band theory. Chapter 2 investigates the spin and spin-orbital texture and electronic structures of the surface states at side surfaces of a topological insulator, Bi_2Se_3, by using slab models within density functional theory. Two representative, experimentally achieved surfaces are examined, and it is shown that careful consideration of the crystal symmetry is necessary to understand the physics of the surface state Dirac cones at these surfaces. This advances the existing literature by properly taking into account surface relaxation and symmetry beyond what is contained in effective bulk model Hamiltonians.

Chapter 3 examines the Fermi arcs of a topological Dirac semimetal (DSM) in the presence of asymmetric charge transfer, of the kind which would be present in heterostructures. Asymmetric charge transfer allows one to accurately identify the projections of Dirac nodes despite the existence of a band gap and to engineer the properties of the Fermi arcs, including spin texture. Chapter 4 investigates the effect of an external magnetic field applied to a DSM. The breaking of time reversal symmetry splits the Dirac nodes into topologically charged Weyl nodes which exhibit Fermi arcs as well as conventionally-closed surface states as one varies the chemical potential.

Examining Topological Insulators and Topological Semimetals Using First Principles Calculations

John W. D. Villanova

(GENERAL AUDIENCE ABSTRACT)

The importance and promise that topological materials hold has been recently underscored by the award of the Nobel Prize in Physics in 2016 "for theoretical discoveries of topological phase transitions and topological phases of matter." This dissertation explores the novel qualities and useful topologically protected surface states of topological insulators and semimetals.

Topological materials have protected qualities which are not removed by weak perturbations to the system. The manifestations of these qualities in topological insulators are spin-momentum-locked surface states which can be used to develop spin-polarized currents in electronics. Further, these states have linear dispersion at a special momentum point, called the Dirac cone. Conventionally these surface states form closed loops in momentum space. But in two other species of topological materials, Weyl and Dirac semimetals, the surface states form open arcs (called Fermi arcs) and these cause anomalous electrical transport properties including Hall conductivity and Nernst effect. Weyl and Dirac semimetals also have special momentum points (nodes) at which the bulk conduction and valence bands touch with linear dispersion. There is great promise in utilizing the topologically protected surface states in the electronics of the future, including spintronics, quantum computers, and highly sensitive devices. Physicists and chemists are also interested in the fundamental physics and exotic fermions exhibited in topological materials and in heterostructures including them.

Chapter 1 provides an introduction to the concepts and methods of topological band theory. Chapter 2 investigates the spin and spin-orbital texture and electronic structures of the surface states of a topological insulator, Bi_2Se_3, at its side surfaces (beyond the familiar cleaving surface). We use slab models within density functional theory (DFT) to investigate two representative, experimentally achieved surfaces, and it is shown that careful consideration of the threefold rotational crystal symmetry is necessary to understand the physics of the surface state Dirac cones at these surfaces. The differing atomic orbital and cationic/anionic characters of the topological states are examined. This advances the existing literature by properly taking into account how the atoms at the surface relax at the interface with the vacuum and the full symmetry beyond what is contained in effective bulk model Hamiltonians.

Chapter 3 examines the Fermi arcs of a topological Dirac semimetal (DSM) in the presence

of asymmetric charge transfer at only one surface, of the kind which would be present in heterostructures comprised of DSMs and topologically-trivial materials. We use a thin slab model within DFT to calculate the electronic structure of the DSM. Asymmetric charge transfer allows one to accurately identify the projections of the linearly dispersing Dirac nodes despite the existence of a bulk band gap and to engineer the properties of the surface Fermi arcs, including their spin texture. Chapter 4 investigates the effect of an external magnetic field applied to a DSM. The breaking of time reversal symmetry splits the Dirac nodes into topologically charged Weyl nodes which exhibit Fermi arcs as well as conventionally-closed surface states as one varies the chemical potential. The topological charge of the Weyl nodes is what makes them, and their Fermi arcs, robust against weak perturbations such as strain. Meticulously determining the topological index, or Chern number, of Fermi surface sheets demonstrates the bulk-boundary correspondence between the Weyl nodes and their Fermi arcs, and provides evidence for the existence of multiple-charge double Weyl nodes which, until now, have only been discussed sparingly in the literature on topological DSMs.

Dedicated to
my parents, Barbara and Peter,
and my brother Daniel,
whose love, encouragement,
and ruthless support,
propelled me through this journey of discovery.

Acknowledgments

I thank my advisor, Professor Kyungwha Park, for her support, advice, and generous devotion of her time. I could not have asked for a better mentor, and I am a better researcher due to her driving direction and expertise. Among so many experiences which I greatly valued and enjoyed as a part of Professors Park's group, the "fifteen minute discussions" which often lasted an hour testify to her commitment to my education and development as a physicist.

I also thank the other committee members Professor Sophia Economou, Professor Jean Heremans, and Professor Chenggang Tao, and the chair of the graduate committee, Professor Eric Sharpe. Aside from their service directly on my committee, whether in class or out of class, I thank them for helpful discussion and consideration which has contributed to my progress as a graduate student.

I am grateful for the advice and administrative finesse of Betty Wilkins, Katrina Loan, and Michele Strauss, who all made it a pleasure to be a part of the Department of Physics. I thank Roger Link for his alacrity and diligence regarding all things IT, which I have certainly benefited from.

Thanks also to my friends from Virginia Tech: Dr. Rebecca Rabino, Dr. Hiba Assi, Sheng Chen, Shadi Esmaeili, Harshwardhan Chaturvedi, Guangpu Luo, Bart Brown, Jacob Carroll, and Yichul Choi for making Virginia Tech a great place to work and for helpful and jovial discussions.

I owe great thanks to my brother, Daniel Villanova, and his fiancée, Rhiannon Grabus. There is hardly anything I could write to explain the support and rewarding nature of progressing through this graduate program with my brother by my side. Finally, I am indebted to my parents, Peter Villanova and Barbara Zaitzow, who have loved and encouraged me through every circumstance, and who prepared me in the most meaningful ways to pursue and complete this Ph.D.

Contents

List of Figures

List of Tables

Attributions

Chapter 2 was previously published. Reprinted with permission from John W. Villanova and Kyungwha Park, "Spin textures of topological surface states at side surfaces of Bi_2Se_3 from first principles," *Physical Review B* **93**, 085122, 2016. DOI:10.1103/PhysRevB.93.085122. Copyright 2016 by the American Physical Society. K. P. wrote much of the first draft, and K. P and J. V. edited and completed the final version. J. V. performed all calculations and produced all figures.

Chapter 3 was previously published. Reprinted with permission from John W. Villanova, Edwin Barnes, and Kyungwha Park, "Engineering and probing topological properties of Dirac semimetal films by asymmetric charge transfer," *Nano Letters* **2017**, *17(2)*, pp. 963-972 DOI:10.1021/acs.nanolett.6b04299. Copyright 2017 American Chemical Society. K. P. and J. V. wrote the first draft, and E. B. edited the final version, as well as making the final manuscript more rigorous and precise. K. P. performed supercell calculations and initially composed the numerical solution for the surface states of the model Hamiltonian. J. V. performed the remaining calculations and produced all figures.

Chapter 4 is substantially based on a manuscript in progress. K. P. wrote a portion of the introduction and generated the final iteration of Wannier functions. J. V. performed all of the other calculations and produced all figures.

Chapter 1

Introduction

1.1 Density Functional Theory

Paul Dirac summarized the necessity of density functional theory (DFT) in 1929,

> The general theory of quantum mechanics is now almost complete...The underlying physical laws necessary for the mathematical theory of a large part of physics and the whole of chemistry are thus completely known, and the difficulty is only that the exact application of these laws leads to equations much too complicated to be soluble. [1]

Of course Dirac did not have DFT exactly in mind at the time, but over the ensuing decades, considerable effort from physicists and chemists produced an approximate, though stunningly accurate, means by which to solve the complicated problem. The last three decades have truly been a heyday for DFT, with the development of more accurate density functionals, the bestowing of a Nobel prize, and essentially exponential growth in publications arising from its use [2]. DFT has become a widely used predictive tool which regularly supports experimental efforts, and hundreds of scientists have promulgated dozens of codes implementing DFT. In this section, the general problem which Hohenburg, Kohn, Sham, and others faced is detailed, as well as the great strides they made toward making the problem computationally tractable.

1.1.1 The Many-body Hamiltonian

The Hamiltonian operator for a system of electrons and nuclei is given by

$$H_{tot} = -\sum_i \frac{\hbar^2}{2m_e}\nabla^2_{\mathbf{r}_i} - \sum_I \frac{\hbar^2}{2m_I}\nabla^2_{\mathbf{R}_I} + \frac{e^2}{4\pi\epsilon_0}\left(\sum_{\substack{i,j \\ j>i}} \frac{1}{|\mathbf{r}_i - \mathbf{r}_j|} + \sum_{\substack{I,J \\ J>I}} \frac{Z_I Z_J}{|\mathbf{R}_I - \mathbf{R}_J|} - \sum_{i,J} \frac{Z_J}{|\mathbf{r}_i - \mathbf{R}_J|}\right), \tag{1.1}$$

where the subscripts i, j and I, J refer to the electrons and nuclei, respectively, m_e and $\mathbf{r}$ are the mass and position of an electron, and m_I and $\mathbf{R}$ are the mass and position of a nucleus. The first term is the kinetic energy of the electrons. The second term is the kinetic energy of the nuclei. The third term is the electron-electron Coulomb interaction with a condition to avoid double-counting. The fourth term is the nucleus-nucleus interaction, and the fifth term is the electron-nucleus interaction.

A major simplification comes from applying the Born-Oppenheimer approximation to separate the electronic degrees of freedom from the nuclear degrees of freedom. This is sensible since the nuclei are much heavier than the electrons and so move much slower; the electrons are as if they are moving in a potential created by fixed nuclei. The wavefunction is considered a product of a nuclear function (ψ_N) and an electron function (Φ) with fixed nuclear positions,

$$\Psi_{tot}(\{\mathbf{r}_i\}, \{\mathbf{R}_I\}) = \psi_N(\{\mathbf{R}_I\})\Phi(\{\mathbf{r}_i\}; \{\mathbf{R}_I\}). \tag{1.2}$$

With this approximation, the Schrödinger equation separates into electronic and nuclear pieces,

$$H_e = -\sum_i \frac{\hbar^2}{2m_e}\nabla^2_{\mathbf{r}_i} + \frac{e^2}{4\pi\epsilon_0}\left(\sum_{\substack{i,j \\ j>i}} \frac{1}{|\mathbf{r}_i - \mathbf{r}_j|} - \sum_{i,J} \frac{Z_J}{|\mathbf{r}_i - \mathbf{R}_J|}\right) \tag{1.3}$$

and

$$\left[-\sum_I \frac{\hbar^2}{2m_I}\nabla^2_{\mathbf{R}_I} + \varepsilon_e(\{\mathbf{R}_I\}) + \sum_{\substack{I,J \\ J>I}} \frac{Z_I Z_J}{|\mathbf{R}_I - \mathbf{R}_J|}\right] \psi_N(\{\mathbf{R}_I\}) = E\ \psi_N(\{\mathbf{R}_I\}), \tag{1.4}$$

where $\varepsilon_e(\{\mathbf{R}_I\})$ is found by solving the eigenvalue problem

$$H_e\ \Phi(\{\mathbf{r}_i\}; \{\mathbf{R}_I\}) = \varepsilon_e(\{\mathbf{R}_I\})\ \Phi(\{\mathbf{r}_i\}; \{\mathbf{R}_I\}).$$

Then the nuclear function can be determined; it is as if the electrons felt an external potential caused by the nuclei, and the solution to this simpler problem is used to update the nuclear positions. In the next section attention to this external potential will be the prime mover in the development of density functional theory as a powerful method to address the intractability of the many-body Schrödinger equation.

1.1.2 The Hohenberg-Kohn Theorems

The Hohenberg-Kohn (HK) theorems [3] state

1. The ground state electron density uniquely determines the external potential, except up to a constant.
2. There exists a functional of the density which can be variationally minimized to give the exact ground state energy when the input is the exact ground state electron density.

For such an important result, the first theorem has a surprisingly tractable proof in the case of nondegenerate ground states. Suppose that there are two external potentials which differ by more than just a constant, $V_{ext}(\vec{r})$ and $V'_{ext}(\vec{r})$, yet result in the same ground state density, $n(\vec{r})$. Yet there are two distinct Hamiltonians, $H(\vec{r})$ and $H'(\vec{r})$, to which the variational principle of the energy still applies,

$$\begin{aligned} E &= \langle\Psi|H(\vec{r})|\Psi\rangle < \langle\Psi'|H(\vec{r})|\Psi'\rangle, \\ E' &= \langle\Psi'|H'(\vec{r})|\Psi'\rangle < \langle\Psi|H'(\vec{r})|\Psi\rangle, \end{aligned} \tag{1.5}$$

where $|\Psi\rangle$ and $|\Psi'\rangle$ are the ground state wavefunctions for their respective Hamiltonians. Since the external potentials are associated with the same ground state density, we can rewrite this as

$$\begin{aligned} \langle\Psi|H(\vec{r})|\Psi\rangle &= \langle\Psi|H'(\vec{r})|\Psi\rangle + \langle\Psi|H - H'(\vec{r})|\Psi\rangle \\ &= \langle\Psi|H'(\vec{r})|\Psi\rangle + \int d\vec{r}\,[V_{ext}(\vec{r}) - V'_{ext}(\vec{r})]\; n(\vec{r}) \\ \langle\Psi'|H'(\vec{r})|\Psi'\rangle &= \langle\Psi'|H(\vec{r})|\Psi'\rangle + \int d\vec{r}\,[V'_{ext}(\vec{r}) - V_{ext}(\vec{r})]\; n(\vec{r}) \\ E + E' &< E + E' \end{aligned} \tag{1.6}$$

with the numbered line being the sum of the above two lines. This is also a contradiction, so these different external potentials must *not* give rise to the same ground state density.

The second theorem follows by writing the energy from the first theorem,

$$\langle\Psi'|H(\vec{r})|\Psi'\rangle = T[n'(\mathbf{r})] + V_{ee}[n'(\mathbf{r})] + \int d\vec{r}\, V_{ext}\; n'(\mathbf{r}) = E[n'(\mathbf{r})] < E[n(\mathbf{r})] = \langle\Psi|H(\vec{r})|\Psi\rangle, \tag{1.7}$$

where T is the kinetic energy, V_{ee} is the electron-electron interaction energy and the functional dependence on the electron density is explicit. The inequality follows immediately from the variational principle of the wavefunction. The term depending on the external potential is system-dependent, but the sum of the kinetic and electron-electron interaction energies should have the same treatment no matter the system. These latter two terms are usually denoted $F[n(\mathbf{r})]$ and termed the *universal* functional.

These form the basis for density functional theory (DFT) and establish its rigor for the ground state of a system. The HK theorems are extremely important in that they establish the existence of the universal functional and the dependency of the ground state on the ground state electron density, but they do not provide any prescription for how to calculate the universal functional and solve the many-body problem.

1.1.3 Kohn-Sham Density Functional Theory

The treatment of the external potential and universal functional by Kohn and Sham (KS) was a real breakthrough into using DFT in a computationally tractable way [4]. Walter Kohn (with John A. Pople) was awarded the Nobel Prize in Chemistry in 1998 for this, among his other contributions to the development of DFT. They treated the system as if it were non-interacting, yet having the identical ground state density as the interacting problem of interest. The details of the problem are not important so long as the ground state density is correct. The HK-theorems guarantee that the ground state can be fully determined from the ground state density.

KS considered a non-interacting system, described by the Schrödinger equation for the i^{th} orbital,

$$\hat{H}_{KS}\ \phi_i(\mathbf{r}) = \left[-\frac{\hbar^2}{2m_e}\nabla^2 + V_{KS}(\mathbf{r})\right]\phi_i(\mathbf{r}) = \varepsilon_i\ \phi_i(\mathbf{r}). \tag{1.8}$$

$V_{KS}(\mathbf{r})$ is the Kohn-Sham potential, and it is important to note that the kinetic energy written here is the non-interacting particle kinetic energy, T_s. The wavefunction in the non-interacting case is the Slater determinant,

$$\Psi_s = \frac{1}{\sqrt{N}}\det[\phi_1\phi_2...\phi_N], \tag{1.9}$$

over the N lowest KS orbitals of the KS Hamiltonian, H_{KS}. The density follows as

$$n(\mathbf{r}) = \sum_{i=1}^{N}|\phi_i(\mathbf{r})|^2, \tag{1.10}$$

with the only condition that the volume integral of this density be identically the number of electrons. Now we can write the *universal* functional, $F[n(\mathbf{r})]$, the sum of the kinetic and electron-interaction energies, explicitly as functionals of the density,

$$F[n(\mathbf{r})] = T[n(\mathbf{r})] + V_{ee}[n(\mathbf{r})] = T_s[n(\mathbf{r})] + E_H[n(\mathbf{r})] + E_{XC}[n(\mathbf{r})]. \tag{1.11}$$

with $T_s[n(\mathbf{r})]$ the sum of the independent-particle kinetic energies, $E_H[n(\mathbf{r})]$ the Hartree energy of the electrons, borne from our use of the Slater determinant as the total wavefunction,

and a third term $E_{XC}[n(\mathbf{r})]$ discussed momentarily. Explicitly, the Hartree energy is given by

$$E_H[n(\mathbf{r})] = \frac{1}{2}\int d\mathbf{r}\; d\mathbf{r}' \frac{n(\mathbf{r})\; n(\mathbf{r}')}{|\mathbf{r}-\mathbf{r}'|}. \tag{1.12}$$

The remaining term, $E_{XC}[n(\mathbf{r})]$, is the exchange-correlation energy, which includes both the non-classical part of the electron-electron interactions and the kinetic energy difference between the interacting system and our choice to treat the system as non-interacting, i.e.,

$$E_{XC}[n(\mathbf{r})] = T[n(\mathbf{r})] - T_s[n(\mathbf{r})] + V_{ee}[n(\mathbf{r})] - E_H[n(\mathbf{r})]. \tag{1.13}$$

Then the total energy functional is finally given by

$$E[n(\mathbf{r})] = F[n(\mathbf{r})] + \int d\mathbf{r}\; V_{ext}(\mathbf{r})\; n(\mathbf{r}) \tag{1.14}$$

where we see the external potential enters again (this is the statement of HK-theorem 2), and whose variation with respect to the density is set to zero:

$$\begin{aligned} \frac{\delta E[n(\mathbf{r})]}{\delta n(\mathbf{r})} = 0 &= \frac{\delta T_s[n(\mathbf{r})]}{\delta n(\mathbf{r})} + V_{KS}[n(\mathbf{r})] \\ V_{KS}[n(\mathbf{r})] &= V_{ext}(\mathbf{r}) + \frac{\delta E_H[n(\mathbf{r})]}{\delta n(\mathbf{r})} + \frac{\delta E_{XC}[n(\mathbf{r})]}{\delta n(\mathbf{r})}. \end{aligned} \tag{1.15}$$

Finally, with the Schrödinger equation dependent on the KS-potential [Eq. (1.8)], the density-functional expression for the KS-potential dependent on the XC-potential [Eq. (1.15)], and the expression for the density itself [Eq. (1.10)], the problem is well-posed. These three equations must be solved self-consistently due to the mutual dependencies, and the only intricacy avoided so far has been explicitly writing the XC-potential. In fact the XC-potential is the most difficult piece of the puzzle, and the development of better approximations for it has been decades in the making. Two common approximations for the XC-potential are the *local density approximation* (LDA) and the *generalized gradient approximation* (GGA). GGA takes into account the density and the density gradient in order to compute the XC-energy. Two popular GGAs were developed by Perdew-Wang (PW91) [5, 6] and Perdew-Burke-Ernzerhof (PBE) [7].

1.1.4 Pseudopotential Methods

Rather than solving an all-electron problem within KS-DFT, it is faster and usually still an excellent approximation to utilize pseudopotentials to simplify the problem. It is in many cases just the valence electrons which are important for bonding and other properties in solids, but the DFT wavefunction of the valence electrons will vary rapidly in the region of

the core electrons in order to maintain its orthogonality to those states. The pseudopotential replaces the potential of the core electrons with a smooth effective potential to make these valence electron states more tractable. This is subject to the constraint that the pseudowavefunction and pseudopotential match the wavefunction and potential beyond a certain cutoff radius. Lowering the cutoff radius makes the pseudopotential "harder" (vs. "softer", see [8, 9]), convergence is slower but the result is that much closer to the precise all-electron result. There are various extra conditions one can impose, one being that the norm of the pseudowavefunction be identical to the norm of the all-electron wavefunction within the cutoff radius [10].

The pseudowavefunction can then be written as a linear combination of plane-waves in a basis which is truncated by a cutoff energy. This further reduces the computational cost of solving the problem and lends itself to using Fourier transform methods to evaluate quantities of interest on a momentum-space grid, exactly what one desires in crystals. The *projector augmented-wave* method (PAW) [11] is one means to implement the plane-wave basis, and the two DFT codes used in this work, VASP and QUANTUM ESPRESSO, both use PAW pseudopotentials. When relativistic effects need to be considered, for example with spin-orbit coupling (SOC), the KS-orbitals are promoted to spinors. The KS-equations are transformed into the Dirac-KS equations. VASP uses the Dirac-KS equations to fully treat the core electrons but makes a scalar relativistic approximation to treat the valence electrons (that is, it treats one component of the spinor as dominant by neglecting SOC compared to the other relativistic terms) [12]. SOC is added via a second-variational method thereafter [13–15].

1.2 Wannier Functions

DFT calculations can be performed using periodic boundary conditions to reproduce a perfect crystal. Due to translational symmetry, Bloch's theorem states that the single electron wave functions can be written as a product of a plane wave and a function ($u_{n\mathbf{k}}$) with the periodicity of the Hamiltonian (and the periodicity of the crystal lattice):

$$\psi_{n\mathbf{k}}(\mathbf{r}) = u_{n\mathbf{k}} e^{i\mathbf{k}\cdot\mathbf{r}}, \tag{1.16}$$

where $\mathbf{k}$ is the crystal momentum. Wannier functions (WFs) are Fourier transforms of these Bloch states, and they should be somewhat localized in a unit cell. Explicitly, the WF for band n in cell $\mathbf{R}$ is

$$|\mathbf{R}n\rangle = \frac{V}{(2\pi)^3} \int_{BZ} d\mathbf{k}\ e^{-i\mathbf{k}\cdot\mathbf{R}} |\psi_{n\mathbf{k}}\rangle, \tag{1.17}$$

with V the real-space primitive cell volume and the integral is performed over the full BZ. The WFs comprise a complete and orthogonal basis set, but they are not unique due to the

existence of a gauge freedom,

$$|\tilde{\psi}_{n\mathbf{k}}\rangle = \sum_{m=1}^{J} U_{mn}^{(\mathbf{k})} |\psi_{n\mathbf{k}}\rangle, \tag{1.18}$$

where J denotes the number of a subset of separated bands and $U_{mn}^{(\mathbf{k})}$ is a unitary matrix which is periodic in reciprocal space. When $U_{mn}^{(\mathbf{k})}$ is diagonal, each element takes the form of a $\mathbf{k}$-dependent phase factor, and that is what is meant by the gauge freedom. So the WFs are not unique, and choices of $U_{mn}^{(\mathbf{k})}$ can smooth out $\tilde{\psi}_{n\mathbf{k}}$ in k-space such that their replacement in Eq. (1.17) results in well-localized WFs in real-space. How "well-localized" the WFs are is measured by a spread functional: the sum of the squares of their spread in the home unit cell ($\mathbf{R} = \mathbf{0}$),

$$\Omega = \sum_{n} \langle \mathbf{0}n|r^2|\mathbf{0}n\rangle - \langle \mathbf{0}n|\mathbf{r}|\mathbf{0}n\rangle^2. \tag{1.19}$$

This is a functional in the sense that it depends on the choice of unitary transformation among the Bloch states (which specifies the WFs). This can also be broken into a term which remains gauge invariant (Ω_I) under any of the choices of the unitary transformation of the Bloch states, and two other terms which are not gauge invariant. These represent the band-diagonal (Ω_D) and band-off-diagonal (Ω_{OD}) contributions to the the non-invariant part of the spread functional. Ω_D vanishes for inversion-symmetric WFs.

$$\Omega = \Omega_I + \Omega_D + \Omega_{OD} \tag{1.20}$$

$$\Omega_I = \sum_{n} \left[\langle \mathbf{0}n|r^2|\mathbf{0}n\rangle - \sum_{\mathbf{R}m} |\langle \mathbf{R}m|\mathbf{r}|\mathbf{0}n\rangle|^2 \right] \tag{1.21}$$

$$\Omega_D = \sum_{n} \sum_{\mathbf{R}\neq\mathbf{0}} |\langle \mathbf{R}n|\mathbf{r}|\mathbf{0}n\rangle|^2 \tag{1.22}$$

$$\Omega_{OD} = \sum_{m\neq n} \sum_{\mathbf{R}} |\langle \mathbf{R}m|\mathbf{r}|\mathbf{0}n\rangle|^2 \tag{1.23}$$

The procedure for minimizing this localization functional is detailed in Refs [16–18] and implemented in WANNIER90 [19]. The resulting WFs are "maximally localized" (MLWF). All one needs is the output of a ground-state electronic structure code from which to calculate the overlaps of the periodic parts of the Bloch functions and their projections onto a set of initial trial functions. The spread functional does not have to be chosen as in Equation (1.19) and can depend on what properties one wants to achieve. The MLWF spread functional is popular and well-justified, but another well-justified choice consists of "symmetry-adapted" or "selectively localized" WFs which uses nearly the same functional on a subset of the target WFs and adds a Lagrange multiplier to constrain the Wannier centers to target positions (e.g. atomic positions) [20, 21]. The resulting WFs may not be "maximally localized," but they are guaranteed to respect the crystal symmetry by construction of the functional.

In Chapter 3, we construct a WF-based tight-binding model for a topological Dirac semimetal. We did not minimize the spread functional in order to find maximally localized WFs as there is a topological obstruction to finding exponentially localized WFs in insulators with nonzero Chern number [22–25]. The same obstruction exists in topological insulators unless one allows the resultant WFs to break time reversal symmetry [26]. Instead, in our semimetallic system, we performed disentanglement (discussed next) without the maximal localization procedure.

1.2.1 Disentanglement

It is common that one desires to form a WF basis from a set of bands which is not strictly separated by a gap from all other bands (as in a metal), or to downfold a set of bands into a WF basis for the development of a low-energy Hamiltonian. In general the number of WFs is necessarily less than or equal to the number of bands contained in the unseparated set of bands at every k-point ($J \leq \mathcal{J}_{\mathbf{k}}$), though the difference in basis size need not be a constant at every k-point. One needs a *disentangling* procedure to accomplish this. As detailed in Ref. 16, for a set of J localized initial orbitals, $g_n(\mathbf{r})$, each is projected onto each band in the entangled set,

$$|\phi_{n\mathbf{k}}\rangle = \sum_{m=1}^{\mathcal{J}_{\mathbf{k}}} |\psi_{m\mathbf{k}}\rangle\langle\psi_{m\mathbf{k}}|g_n\rangle, \tag{1.24}$$

which is the same procedure as was used for separated bands but abandoning square matrices when $J \neq \mathcal{J}_{\mathbf{k}}$. The set of J states, $|\phi_{n\mathbf{k}}\rangle$, are then orthonormalized and used in place of $|\psi_{n\mathbf{k}}\rangle$ in Eq. (1.17). Marzari and Vanderbilt state that this accomplishes the subspace and gauge selections necessary to achieve the desired smoothly varying Bloch functions, though not optimally [16]. The same localization procedure can be performed to minimize the gauge-dependent piece of the spread functional. A further constraint is often necessary: one can apply a "frozen window" in energy in which the Bloch states achieved through projection must match the Bloch states before the Wannierization procedure. The bands comprising the "frozen window" are a subset of the $\mathcal{J}_{\mathbf{k}}$ bands. The energy range is system- and purpose-specific; reasonable choices of bands to freeze could include all bands up to the Fermi level, or all bands within a relevant range around the Fermi level.

1.2.2 Tight-Binding Model from Wannier Functions

The localized feature of the WFs naturally lends itself to the development of a tight-binding Hamiltonian for future calculative simplicity. This is given below, a Fourier transform of the real-space Hamiltonian which is straighforwardly computed from the WFs,

$$H_{mn}(\mathbf{k}) = \frac{1}{N}\sum_{\mathbf{R}} e^{i\mathbf{k}\cdot\mathbf{R}}\, t_{mn}(\mathbf{0}-\mathbf{R}), \tag{1.25}$$

with the hopping parameters given by

$$t_{mn}(\mathbf{0}-\mathbf{R}) = \langle \mathbf{0}m|H|\mathbf{R}n\rangle. \tag{1.26}$$

The hopping parameters can be properly symmetrized for the particular problem, and since they decay with increasing $|\mathbf{R}-\mathbf{0}|$, perhaps only a small set of hopping parameters need to be considered in the first place. (See for example, Ref. 27 in graphene or Ref. 28 in the MoS_2 family.)

1.3 Topological Insulators

In only the last fifteen years, a new class of materials called topological insulators (TIs) exhibiting unique quantum-mechanical properties has begun to be studied rigorously [29–34]. The famous integer quantum Hall effect (QHE) was the first instance of a topological quantum state [35–37]. In a perpendicular magnetic field, non-interacting electrons confined to two-dimensions have an equally-spaced energy spectrum consisting of Landau levels (LLs), which have a degeneracy proportional to the strength of the magnetic field. The Hall conductance is quantized, proportional to the number of filled LLs, ν, which also gives the number of edge-propagating states present. In fact, ν is a topological number called the Chern number which can be calculated from the band structure [37], and the Chern number will be discussed in Section 1.5.1. Topological insulators strongly connect the band theory of solids to the mathematical study of topology in a similar way; the novel features of TIs which we will discuss are robust and guaranteed so long as the mechanism of topological protection is preserved. While insulating in the bulk, when TIs interface with non-topological (trivial) insulators or the vacuum, gapless conducting states arise on the interface in order to connect the two topologies. The existence of topologically protected surface states has garnered much attention for their promise in the development of spintronics [38–42], massive spin transfer torques [43–46], and the possibility of accessing other novel quantum states including Majorana fermions [47–50] and Weyl fermions [51]. In this section, we will discuss time reversal symmetry as the mechanism of topological protection, the assignment of a topological number to discern topological systems from trivial systems, and what role SOC plays in the latter. Finally, we will comment on topological surface states and apply these principles to a prototypical topological insulator, Bi_2Se_3.

1.3.1 Time Reversal Symmetry

A key ingredient in the assignment of a topological index in topological insulators is time reversal symmetry (TRS). Time reversal results in the reversal of momentum and flipping of spin, and its manifestation as a quantum operator is given by $\Theta = i\sigma_y K$, where σ_y is the Pauli spin matrix and K is an operator which performs complex conjugation. The TRS operator is antiunitary (as can be seen from it being the product of a unitary operator and the complex conjugation operator) and has the property that $\Theta^2 = -1$, as is necessary for systems of half-integer spin.

TRS and the Bloch Hamiltonian For a periodic electronic system, from Bloch's theorem we have the cell-periodic Schrödinger equation,

$$H(\boldsymbol{k})|u_{n\boldsymbol{k}}\rangle = E_{n\boldsymbol{k}}|u_{n\boldsymbol{k}}\rangle, \tag{1.27}$$

which satisfies TRS if

$$H(-\boldsymbol{k}) = \Theta H(\boldsymbol{k})\Theta^{-1}. \tag{1.28}$$

Immediately one sees that at particular momenta in the Brillouin zone (BZ) where $\boldsymbol{k} = -\boldsymbol{k} + \boldsymbol{G}$, with $\boldsymbol{G}$ a reciprocal lattice vector, an energy band and its time-reversed partner have the same energy. Each of these special momenta is called a time-reversal-invariant momentum (TRIM) and the two time reversal partner states at the TRIM are called a Kramers pair. This is a statement of the Kramers degeneracy theorem, that in systems of half-integer spin, $|\Psi\rangle$ and $\Theta|\Psi\rangle$ are orthogonal quantum states which have the same energy so that at least double degeneracy is enforced. In periodic systems with inversion symmetry, the Kramers pair of bands is degenerate not only at TRIMs but throughout the entire BZ.

1.3.2 Development of the Topological Invariant

Fu and Kane [52] then defined a unitary matrix, $w_{mn}(\boldsymbol{k}) = \langle u_{-\boldsymbol{k}m}|\Theta|u_{\boldsymbol{k}n}\rangle$, which is antisymmetric at TRIMs (Λ_i) and indicates the overlaps of the occupied Kramers pairs. This means that $w_{mn}(\Lambda_i)$ is an even-dimensional antisymmetric matrix, and so it can be brought into a block-diagonal form by an orthogonal transformation [53], with each block being a 2×2 antisymmetric matrix itself. Only the elements $w_{2j-1,2j}$ for $j \in 1...N$ are nonzero, making explicit that the matrix only connects Kramers pairs. The antisymmetric property allows one to calculate the Pfaffian of the matrix,

$$\mathrm{Pf}[w(\Lambda_i)] = w_{12}(\Lambda_i)w_{34}(\Lambda_i)...w_{2N-1,2N}(\Lambda_i), \tag{1.29}$$

$$\mathrm{Pf}[w(\Lambda_i)]^2 = \det[w(\Lambda_i)]. \tag{1.30}$$

We can write a compact expression for a factor of the topological index using the Pfaffian of the $w(\Lambda_i)$ matrix,

$$\delta(\Lambda_i) = \frac{\mathrm{Pf}[w(\Lambda_i)]}{\sqrt{\det[w(\Lambda_i)]}}. \tag{1.31}$$

Because of Equation (1.30) it is apparent that these factors and their product, which gives the invariant, can only take values of ± 1. A single Z_2 bulk topological invariant is defined for a two-dimensional (2D) system. Moore and Balents [54] showed that four independent Z_2 invariants are defined for a three-dimensional (3D) system. For 3D insulators, the Z_2 indices are

$$(-1)^{\nu_0} = \prod_{n_i=0,\pi} \delta(\Lambda_{n_1,n_2,n_3}) \tag{1.32}$$

$$(-1)^{\nu_i} = \prod_{\substack{n_i=\pi \\ n_{j\neq i}=0,\pi}} \delta(\Lambda_{n_1,n_2,n_3}), \tag{1.33}$$

so that ν_0, the so-called "strong index," is unique to a 3D system and the three ν_i's are each associated with a 2D plane of the BZ. This is commonly written as (ν_0; ν_1, ν_2, ν_3). For example, in a cubic BZ with indices (0; 0,0,1), the strong index is zero and topological surface states associated with the nontrivial index can be expected on the (001) surface. These indices are topological in the sense that no smooth deformation to the Hamiltonian which preserves the insulating bandgap and TRS will change these integers, which were calculated by considering the full set of occupied bands.

1.3.3 The Topological Invariant for Inversion Symmetric Systems

In inversion symmetric (IS) systems, there is a simplification which makes the calculation of the invariant much easier and led to the prediction and detection of a basket of topological insulators [55–57]. The inversion operator, Π, reverses the position and momentum, but leaves the spin untouched. In contrast to time reversal, $\Pi^2 = 1$, and inversion symmetric Hamiltonians satisfy $\Pi H(\boldsymbol{k})\Pi^{-1} = H(\boldsymbol{k})$. The parity eigenvalues of Kramers pairs are identical, and so a single eigenvalue associated with each pair is written ξ_{2n}. Ando [32] inserts the parity operator into the $w_{mn}(\boldsymbol{k})$ matrix,

$$\begin{aligned} w_{mn}(\Lambda_i) &= \langle u_{-\Lambda_i,m}|\Pi^2\Theta|u_{\Lambda_i,n}\rangle \\ &= \xi_m(\Lambda_i)\langle u_{\Lambda_i,m}|\Pi\Theta|u_{\Lambda_i,n}\rangle \\ &= \xi_m(\Lambda_i)v_{mn}(\Lambda_i). \end{aligned} \tag{1.34}$$

Now the Pfaffian of the antisymmetric matrix is

$$\mathrm{Pf}[w(\Lambda_i)] = \mathrm{Pf}[v(\Lambda_i)] \prod_{n=1}^{N} \xi_{2n}(\Lambda_i). \tag{1.35}$$

It is possible to adjust the phase of the periodic part of the Bloch functions such that $\mathrm{Pf}[v(\Lambda_i)] = 1$, thus the topological indices may be written as the product of the parity eigenvalues of occupied Kramers pairs at TRIMs,

$$\delta(\Lambda_i) = \prod_{n=1}^{N} \xi_{2n}(\Lambda_i). \tag{1.36}$$

This is a much simpler prescription for systems with inversion symmetry, and will now assist in demonstrating why topological insulators have primarily been discovered in materials containing heavy elements.

1.3.4 Spin-orbit Coupling and Band Inversion

The spin-orbit coupling (SOC) is given by

$$H_{soc} = \frac{\hbar}{4m^2c^2}(\nabla V \times \vec{p}) \cdot \vec{\sigma} = \frac{\hbar}{4m^2c^2}\frac{1}{r}\frac{\partial V}{\partial r}\vec{L} \cdot \vec{\sigma} = \lambda \vec{L} \cdot \vec{\sigma} \tag{1.37}$$

where m is the mass of the electron, V is the spherically symmetric electric potential, $\vec{p}$ is the linear momentum, and $\vec{\sigma}$ is the vector of Pauli matrices. When one evaluates the matrix elements directly using the Coulomb potential, we have that the expectation value of the radial piece is,

$$\left\langle \frac{Z}{r^3} \right\rangle_{nl} = \frac{Z^4}{a_0^3 n^3} \frac{1}{l(l+1/2)(l+1)}, l \neq 0, \tag{1.38}$$

with a_0 the Bohr radius. Heavier elements exhibit a greater spin-orbit interaction since $\lambda \propto Z^4$, and this can have a significant impact on the band structure of an insulator. Specifically, in an insulator SOC may shift the ordering of the bands to the point that they invert at some points in the BZ. In common semiconductors, the lowest conduction band has positive parity and the highest valence band has negative parity. SOC can push these bands into each other, and with an avoided crossing, the insulating nature is maintained while the parities (and orbital characters) of the conduction and valence bands are exchanged. A normal insulator without spin-orbit coupling can become a topological insulator with sufficiently strong spin-orbit coupling via a band inversion which exchanges the parities of the conduction and valence bands. This makes it easy to see for systems with inversion symmetry and thus well-defined parities how the band inversion yields a nontrivial topological index: consider a trivial insulator with conventional band ordering at every TRIM in the absence of SOC. When SOC is considered, if a band inversion occurs at an odd number of TRIMs, the product of parity eigenvalues in Equation (1.36) switches sign an odd number of times, and the Z_2 invariant is nontrivial.

1.3.5 Surface States

The important and exciting consequence of this bulk topological property of TIs is the existence of conductive states at the surface. Due to the strong SOC, there is also a relationship between the spin and momentum, called spin-momentum-locking, which is discussed in the next section and in Chapter 2. Consider a band structure involving two pairs of spin-polarized surface states. These states of course still must satisfy the Kramers degeneracy, in particular $E(\Lambda_i, \uparrow) = E(\Lambda_i, \downarrow)$, and can do so in two ways: (0, trivial) each pair stays

separately with its own partner across the BZ, so that the chemical potential can be tuned where it crosses an even number of surface states between TRIMs or (1, nontrivial) each pair switches partners between TRIMs so that the chemical potential must necessarily cross an odd number of surface states. This is the manifestation of the bulk topological nature at the surface, called *bulk-boundary correspondence*.

1.4 Bi_2Se_3 as a Topological Insulator

The first proposed 3D topological insulator was a $Bi_{1-x}Sb_x$ alloy, which experiences a band inversion for certain concentrations, $0.09 < x < 0.18$ [58]. There is a bulk gap of only 30 meV at the TRIM L point in the BZ, and the observed topological surface states have a complex nonmonotonic dispersion connecting the projected bulk bands at TRIMs L and Γ [55]. So when Bi_2Se_3 (and its family of rhombohedral chalcogenides) was proposed to be a topological insulator with a single Dirac cone at the Γ point, with a bulk gap of 300 meV [59], and with an easily exfoliated surface on which to detect topological surface states, there was a great deal of excitement and characterization of this material.

Let us turn to Bi_2Se_3 as a prototypical example of a topological insulator. Bi_2Se_3 crystallizes in a rhombohedral structure ($R\bar{3}m$, space group No. 166) whose relevant symmetries are a three-fold rotation, a mirror plane, inversion, and time reversal. The atomic layers have ABC-stacking along the crystal c-axis, and the crystal structure is a layer structure in which five atomic layers form a covalently bonded unit, a quintuple layer (QL). See also Fig. 1.1. Successive QLs are only weakly bonded via the van der Waals interaction. Thus there is a natural cleaving plane between QLs which makes Bi_2Se_3 attractive to investigate in the search for topological surface states. The natural cleaving plane is the (111) surface (in Miller indices corresponding to the rhombohedral primitive cell vectors), and this section discusses Bi_2Se_3 generally as well as this surface. Other surfaces will be discussed in Chapter 2.

The necessary strong SOC derives from the heavy Bi atoms, and this results in a band inversion at the Γ point. The relevant bands come from p-orbitals, specifically $\{|P1^+, \pm\frac{1}{2}\rangle$, $|P2^-, \pm\frac{1}{2}\rangle\}$, where $P1$ and $P2$ denote orbitals arising from bismuth and selenium, respectively, the superscript denotes the parity, and the fraction is the z-component of the total angular momentum. The opposite parity states from each atomic species are formed by taking linear combinations of the p-orbitals on inversion-pair atomic sites, i.e. the sum (difference) gives the positive (negative) parity state. These $m_j = +(-)\frac{1}{2}$ states are themselves linear combinations of the states $|p_z, \uparrow (\downarrow)\rangle$ and $|p_{+(-)}, \downarrow (\uparrow)\rangle$, but the p_z-orbital is the dominant contributor, as emphasized in Ref. [59].

Liu *et al.* [60] carefully construct the minimal four-band $\mathbf{k} \cdot \mathbf{p}$ bulk Hamiltonian for the definite-parity $m_j = \pm\frac{1}{2}$ states of each atomic species by considering what terms are allowed by the bulk symmetries of Bi_2Se_3. This procedure is called the method of invariants (see also [61]). Appendix A.1 describes how to construct the transformation matrix for a rotation

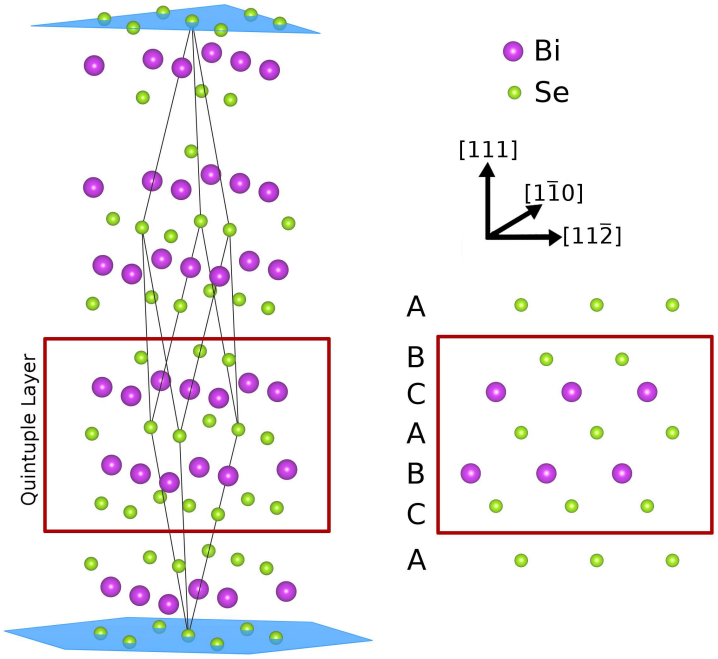

Figure 1.1: Geometry of bulk Bi_2Se_3 in the R$\bar{3}$m structure (space group No. 166). The rhombohedral unit cell is shown, and a single quintuple layer (QL) is emphasized in red. The (111) plane is shown in blue, and the ABC-stacking is shown at right.

about an arbitrary axis using the Wigner D-matrix (in this case specifically, the rotation matrix takes a simple form since the rotational axis coincides with the z-axis). The effective Hamiltonian so derived is given by,

$$\hat{H}_{eff} = \varepsilon(\mathbf{k})\mathbf{I_4} + \sum_i d_i(\mathbf{k})\Gamma_i + \sum_{ij} d_{ij}(\mathbf{k})\Gamma_{ij}, \tag{1.39}$$

where $\mathbf{I_4}$ is the 4×4 identity matrix, Γ_i are the five Dirac Γ matrices satisfying the Clifford algebra, and $\Gamma_{ij} = [\Gamma_i, \Gamma_j]/(2i)$ are the ten commutators of the Γ matrices. $\varepsilon(\mathbf{k})$, $d_i(\mathbf{k})$, and $d_{ij}(\mathbf{k})$ can be expanded in powers of the momentum and must belong to the same symmetry representation under the bulk crystal symmetries as the corresponding Γ_i and Γ_{ij} matrices. Liu *et al.* [60] are meticulous about this procedure and listing the representations of the Γ matrices and momentum polynomials.

The (111) surface Hamiltonian can be derived from this bulk Hamiltonian by making the replacement $k_z \to -i\partial_z$ and applying the open boundary condition $\psi(0) = 0$ for the semi-infinite slab occupying $z > 0$. Naturally the resulting surface Hamiltonian respects all of the 2D symmetries of the surface,

$$H(\vec{k}) = E_0(k) + v(k_x\sigma_y - k_y\sigma_x) + \frac{R}{2}(k_+^3 + k_-^3)\sigma_z, \tag{1.40}$$

where $E_0(k)$ contains only even terms of the 2D-momentum k, v is the Fermi velocity of the surface states, $k_\pm = k_x \pm ik_y$, σ_i are the Pauli matrices, and the R-term reduces the overall rotational symmetry from circular to C_3. The lowest order terms are linear in k and yield circular equal-energy-contours (a Dirac cone around the TRIM). The Dirac cone has circulating in-plane spin texture which is always perpendicular to the momentum; the latter feature is called spin-momentum locking. This is where the promise of using TIs in modern spintronics arises: the perpendicular spin-momentum-locking of the surface states, the only existing surface states in the middle of the bulk gap, guarantees that an applied current is spin-polarized on a given surface. This is without an applied magnetic field, and the TRS forbids perfect backscattering of transport electrons; the spin-momentum-locking associates the spin with the transport direction, so without a mechanism to flip the spin, there is a zero matrix element between oppositely propagating states.

The higher-order SOC term, the R-term, gives rise to "hexagonal warping" [62]. It lowers the symmetry of the energy contours to appear sixfold symmetric (the combination of the C_3 and mirror symmetries) and permits a small out-of-plane spin component at nonzero momenta. It will be shown in Chapter 2 that the correct and complete consideration of all the surface symmetries is necessary to understand the shape of the energy contours and spin texture of the surface states of terminations of Bi_2Se_3 other than the easy (111) plane.

1.5 Weyl and Dirac Semimetals

In the previous section, we considered the bulk topological nature of an insulator with TRS which gave rise to gapless states (the Dirac cone) on the surface. It was stated that if the bulk insulating gap (or TRS) is not preserved, the insulator returns to a normal insulating state, losing its topological properties. What happens at the phase transition point: when the bulk gap is closed at a point and gapless states exist in the bulk crystal? To that end, we now turn to the Weyl and Dirac semimetals which exhibit such Dirac dispersion in the bulk.

The fermion whose motion is described by the massless Dirac equation is called a Weyl fermion, after Hermann Weyl, and it has a definite chirality [63]. Although there are no discovered Weyl fermions in particle physics today, they have recently been realized in solid-state systems [64–66] and experiments have explored some of the novel physics arising from their existence. Solid-state systems can thus be a playground of sorts for particle physics and beyond, albeit constrained by the conservation of charge [67] and lacking Lorentz invariance (type II Weyl semimetals) [68]. Weyl fermions have a definite chirality, and so the Adler-Bell-Jackiw chiral anomaly [69, 70] is observed in materials exhibiting Weyl fermions

(previously, the chiral anomaly was observed via pion lifetime measurements [71]). The anomalous current is proportional to $\mathbf{E}\cdot\mathbf{B}$, so it is susceptible to a strongly angle-dependent measurement, and there is expected to be negative magnetoresistance when the electric field $\mathbf{E}$ is parallel to the magnetic field $\mathbf{B}$ [72].

In solid-state physics, Weyl fermions are observed in Weyl semimetals (WSMs), in which the bulk conduction and valence bands touch at an even number of momenta within the BZ, called Weyl nodes. The bands have linear dispersion in at least one direction [73], or in every direction for the conventional Weyl fermion envisioned by Weyl. Taking as an example the system of two Weyl nodes separated in momentum space which linearly disperse in all directions, the low-energy Hamiltonian around one Weyl node is $H(\mathbf{k}) = \mathbf{d}(\mathbf{k})\cdot\sigma$, where $\mathbf{d}$ is a vector of momentum-dependent functions, the lowest order linear term of which is the Fermi velocity, and σ is the vector of Pauli matrices. The Weyl node is considered at the origin. Because this Hamiltonian involves all of the Pauli matrices, there is no means by which to add a mass term which would gap the Weyl node. Any mass term which one could add would merely shift the position or energy of the Weyl node, and in this sense the Weyl node is robust. There is a topological number (chirality, chiral charge, or Chern number) associated with this robustness, here given by $\operatorname{sgn}\left(\left|\frac{\partial d_i}{\partial k_j}\right|\right) = \pm\chi$, where the argument of the signum function is the Jacobian. It is necessary that either TRS or IS or both be broken so that the two Weyl cones of opposite chirality do not overlap and annihilate each other. The special case when two Weyl cones overlap and do not annihilate is called a topological Dirac semimetal, discussed later in 1.5.4. For now, we will discover the origin of this topological number.

1.5.1 The Chern Number

The topological number for the Weyl node is calculated as a property of the band structure. One calculates the Berry connection [74] of the periodic part of the Bloch states,

$$\mathbf{A}(\mathbf{k}) = \sum_{n=1}^{N} i\langle u_{n\mathbf{k}}|\nabla_{\mathbf{k}}|u_{n\mathbf{k}}\rangle, \tag{1.41}$$

where N is the number of occupied bands, and the Berry curvature as the curl of the connection,

$$\boldsymbol{\Omega}(\mathbf{k}) = \nabla_{\mathbf{k}}\times\mathbf{A}(\mathbf{k}). \tag{1.42}$$

The Berry connection serves as a vector potential for the Berry curvature, justifying the description of the Berry curvature as a momentum-space magnetic field deriving from the band structure. Just as Gauss's Law for magnetism demands that the magnetic flux vanish, the corresponding requirement in the solid-state is that the Berry curvature flux through the entire BZ boundary also vanish. However, one can select other closed surfaces inside of the BZ through which the Berry curvature in some systems in fact does not vanish, which

indicates the existence of an uncompensated set of Berry curvature poles inside the enclosing surface. This is the topological number, called the Chern number,

$$\chi = \frac{1}{2\pi} \oint_S dS \; \hat{\boldsymbol{n}} \cdot \boldsymbol{\Omega}(\boldsymbol{k}). \tag{1.43}$$

Here the surface, S, is chosen to enclose a single Weyl node, with its unit normal vector pointing out from the center of the sphere. The Chern number is the chiral charge of the Weyl node. To make a connection to the physics of another topological state, this formulation of the Chern number is identical to that employed by Thouless, Kohmoto, Nightingale, and den Nijs (TKNN) to demonstrate the quantized conductance in the integer QHE; the Berry curvature was a function of the 2D-momentum and the integral was performed over the closed, toroidal surface of the full 2D-BZ. This gave an integer, the Chern number, equivalent to the number of occupied Landau levels, ν [37]. Each Weyl node which is a source of $2\pi\chi$ Berry curvature flux; when $\chi > 1$, it is called a multiple Weyl node (e.g. single or double for $\chi = 1$ or $\chi = 2$, respectively) [73].

As already mentioned, the number of Weyl points must be even to ensure that the total Berry curvature flux through the BZ boundary vanishes. The minimum number of Weyl points one can achieve in a crystal with only broken TRS is two, while with only broken IS it is four. Weyl nodes cannot exist in a mirror plane as the mirror operation would reverse the Berry curvature and yet leave the Weyl node in the same position ("annihilating" with itself). Table 1.1 lists some common crystal symmetry operations and their effects on the Berry curvature; it is apparent that in systems with both TRS and IS, the Berry curvature vanishes at every momentum and the Weyl semimetal state cannot be supported.

Table 1.1: Action of symmetry operations on the Berry curvature.

Symmetry	Operation	Result
TRS	$\Theta\ \boldsymbol{\Omega}(\mathbf{k})$	$-\boldsymbol{\Omega}(-\mathbf{k})$
IS	$\mathcal{I}\ \boldsymbol{\Omega}(\mathbf{k})$	$\boldsymbol{\Omega}(-\mathbf{k})$
Mirror	$\mathcal{M}_x\ \boldsymbol{\Omega}(\mathbf{k})$	$-\boldsymbol{\Omega}_{y,z}(-k_x, k_y, k_z), \boldsymbol{\Omega}_x(-k_x, k_y, k_z)$
Rotation	$\mathcal{C}_n(z)\ \boldsymbol{\Omega}(\mathbf{k})$	$\mathcal{R}_n\boldsymbol{\Omega}(\mathcal{R}_n k_x, \mathcal{R}_n k_y, k_z)$

1.5.2 Fermi Arcs

As in TIs, the bulk-boundary correspondence demanded surface states which reveal the bulk topological nature. This is also the case for WSMs, which is a departure from the analogy to Weyl fermions of particle physics. The argument of Wan *et al.* [64] is particularly instructive: consider a cylinder which encloses a single Weyl point at $E = 0$, with its axis aligned with the surface-normal. There exists a gap everywhere on the surface of this cylinder, and its

surface comprises a 2D BZ with nontrivial Chern number due to the Berry curvature flux. The surface of the cylinder is a quantum Hall insulator, and so there must be a chiral edge state with $E = 0$ somewhere on the cylindrical surface. Now one can vary the radius of this cylinder and plot the point at which there is the chiral edge state with $E = 0$ for each choice of radius, gradually drawing a curve which terminates on the projection of the enclosed Weyl point. Just when the radius is large enough to enclose both Weyl points, there is no longer a chiral edge state with $E = 0$, and so this curve also terminates at the projection of the partner Weyl point. The final result is an open curve (Fermi arc) on the surface which connects Weyl points of opposite chirality. It is also apparent that if there are multiple Weyl points which project to the same point in the surface BZ, this argument guarantees a number of Fermi arcs commensurate with the enclosed chiral charge.

The open Fermi arcs are predicted to have a novel response to an external magnetic field; the electron magnetic orbits, rather than being closed on one surface, "close" through the bulk of the material. The Weyl orbit consists of traveling along the Fermi arc, tunneling through the projection of the Weyl node to the opposite surface, continuing along that opposite surface's Fermi arc, and again tunneling through the projection of the partner Weyl node (see Fig. 1.2). The inclusion of part of the orbit through the bulk crystal involves a thickness dependence which is unique to systems with Weyl nodes [75–77].

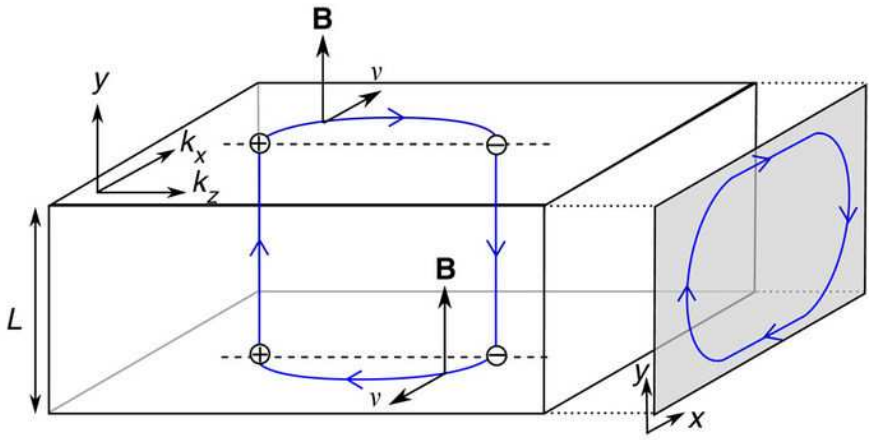

Figure 1.2: Schematic of the semiclassical Weyl orbit formed by Fermi arcs in a magnetic field directed along $\hat{\mathbf{y}}$ which gives rise to quantum oscillations in a finite thickness slab. The image is in a mixed real-and-momentum space system, showing how an electron moves along the surface Fermi arcs connecting Weyl points in momentum-space and through the slab in real-space to form a closed orbit. (The inset shows the corresponding real-space trajectory.) Reprinted by permission from Springer Nature: Nature Communications, "Quantum oscillations from surface Fermi arcs in Weyl and Dirac semimetals," A. C. Potter, I. Kimchi, and A. Vishwanath, copyright 2014 [75].

1.5.3 An Expanding Field

Weyl semimetals were first predicted to occur in the TRS-breaking pyrochlore iridiates, but with 24 Weyl points [64], the electronic structure and Fermi arc connectivity is complicated. Without experimental confirmation of the WSM state in the TRS-breaking pyrochlore iridate, it was very attractive to discover a naturally IS-breaking WSM instead. Experimentalists would not have to apply a strain or external magnetic field to achieve the WSM state or tuning elemental composition in alloys to the topological phase transition point. And it is easier to use ARPES to study the surface states without having to worry about the magnetic order of the TRS-breaking WSM. In March 2015, TaAs (with TaP, NbAs, and NbP) was predicted to be such an IS-breaking WSM with 24 Weyl points by using DFT [78], however, many of these were related to each by rotational and mirror symmetries of the crystal. The Fermi arcs were predicted to extend over a significant region in the BZ. Just four months later, two experimental groups observed Fermi arcs in TaAs using angle-resolved photoemission spectroscopy (ARPES) [65, 66], and a third group [79] observed angle-dependent magnetoresistance and deduced a π Berry phase for these magnetic orbits in TaAs. This flurry of experimental evidence confirming the undergirding theoretical prediction of WSMs in real materials stoked the flames of research into an ever-growing menu of topological semimetals: type I Weyl (Mn_3Ge/Sn [80–82]), type II Weyl ($MoTe_2$ [83–85], WTe_2 [86–88], $TaIrTe_4$ [89–91]), multi-Weyl ($HgCr_2Se_4$ [92]), nodal-line ([93], Ca_3P_2 [94, 95]), and nodal-chain (IrF_4 [96], HfC [97]) among others. The type II WSMs have received significant attention because the Weyl nodes occur at band touching points between electron- and hole-pockets; therefore the Fermi velocity of the bands forming the Weyl node have the same sign in at least one direction. The WSM state has been observed in many of the preceding materials, though not all. DFT is leading the way as a tool to predict the topological nature in many of these proposed systems.

1.5.4 Dirac Semimetals

Conspicuously absent from the preceding list is a class of semimetals which has interested scientists for some years before the discovery of WSMs. They exhibit much of the same novel physical phenomena including the chiral anomaly and Fermi arcs and hold the promise of being driven into the WSM state by breaking either IS or TRS; these are the Dirac semimetals (DSMs). DSMs are inversion- and time-reversal-symmetric with four-fold band touching points (Dirac nodes) at a discrete number of momenta in the 3D-BZ. It was theoretically proposed that a DSM could occur in BiO_2 with the Dirac node at a TRIM [98]. But the first experimentally confirmed DSMs were actually *topological* Dirac semimetals: Na_3Bi [99–101] and Cd_3As_2 [76, 102, 103]. These materials have a rotational symmetry which protects two four-fold band crossing points along the rotation axis and a mirror plane perpendicular to the axis which has a nontrivial 2D topological invariant. Since the Dirac nodes occur away from the BZ boundary, each can be considered as a crystal-symmetry-stabilized superposition of

opposite chirality Weyl nodes. Breaking bulk IS or TRS can split the Dirac node into multiple Weyl nodes of various chiral charge, provided the total chiral charge in the BZ remains zero. The argument for the existence of Fermi arcs presented in 1.5.2 does not provide a guarantee for these surface states in DSMs despite them being observed via ARPES. There have been some recent developments questioning the robustness of the experimentally observed Fermi arcs in DSMs [104–106], and this will be discussed in Chapter 3. Topological DSMs have been predicted in elemental α-Sn [107] and LiZnBi [108], as well as type II DSMs in VAl_3-family [109] and $PtSe_2$ [110]. Excellent reviews on the topic of Dirac and Weyl semimetals have been disseminated as interest in topological semimetals has steadily grown [111–115]. Finally, topological DSMs are discussed in greater detail in Chapters 3 and 4, using Na_3Bi as a prototypical system.

Chapter 2

Topological surface states at side surfaces of Bi_2Se_3

This chapter was previously published. Reprinted with permission from John W. Villanova and Kyungwha Park, "Spin textures of topological surface states at side surfaces of Bi_2Se_3 from first principles," Physical Review B ***93***, *085122, 2016. DOI:10.1103/PhysRevB.93.085122.*

2.1 Introduction

Symmetry-protected topological phases are interesting due to robustness of boundary states within a bulk band gap as long as a given symmetry is preserved. Two well-known examples are topological insulators (TIs) in the presence of time-reversal symmetry [29, 30] and topological crystalline insulators with mirror symmetry [117]. One class of the most studied three-dimensional TIs is the rhombohedral Bi_2Se_3 family with strong spin-orbit coupling (SOC). Along the crystal c axis, i.e., the [111] direction, atomic layers are arranged in units of quintuple layers (QLs) consisting of Se-Bi-Se-Bi-Se with ABC stacking [Fig. 2.1(a)] [59]. The thickness of one QL is about 1 nm. Neighboring QLs are bonded via weak van der Waals interactions, which facilitates exfoliation to create a (111) surface (or (0001) surface in the hexagonal lattice structure) and allows one to intercalate various neutral atoms within the van der Waals gap. Therefore, most studies of topologically protected surface states in the Bi_2Se_3 family have been carried out for the (111) surface. The previous theoretical and experimental works show an in-plane Rashba spin texture with interesting spin-orbital correlation in the vicinity of the Dirac point at Γ for the (111) surface [118–121].

Recently, nanoribbons and nanowires of Bi_2Se_3 family have been grown along the $[1\bar{1}0]$ direction (i.e., $[11\bar{2}0]_{\text{hex}}$), or along the [111] direction [122–125]. In the former case, the top and bottom surfaces correspond to (111) surfaces, while the side surfaces are $(11\bar{2})$ surfaces,

where the $[11\bar{2}]$ direction corresponds to $[1\bar{1}00]_{\text{hex}}$. In the latter case, the top and bottom surfaces are $(1\bar{1}0)$ surfaces, and the side surfaces are $(11\bar{2})$ surfaces. See Fig. 2.1(a)-(c) for the overall directions and top views of the $(1\bar{1}0)$ and $(11\bar{2})$ surfaces, respectively. In addition, nanoplates of Bi_2Se_3 family have been fabricated with facets other than (111) [126]. Films of Bi_2Se_3 family with a (221) surface were also synthesized and their transport properties have been measured [127, 128]. Measurements of transport properties of the nanoribbons, nanowires, and nanoplates have shown strong anisotropy in electrical conductivity and in response to an external magnetic field, which is distinct from corresponding experiments on the (111) surface. Furthermore, at the side surfaces the outermost atomic layer contains both Bi and Se atoms, which would facilitate the possibility of either hole or electron doping by adsorption, whereas at the (111) surface adsorption mostly likely gives rise to electron doping due to the anionic nature of the outermost Se atomic layer.

Despite the interesting experiments on the side surfaces of the Bi_2Se_3 family, there are much fewer theoretical studies on those side surfaces than on the (111) surface. The previous works [129–131] based on the effective model Hamiltonian treated all the normal surfaces to the (111) surface to be equivalent, and thus the spin textures of the $(1\bar{1}0)$ and $(11\bar{2})$ surfaces were shown to be identical. In these works, exclusion of higher order terms in the bulk Hamiltonian imparted continuous rotational symmetry to the (111) surface rather than the discrete symmetries actually present, and the surface reconstruction effect was absent.

In this work, we examine the spin and spin-orbital textures and electronic structures of topological surface states at the side or normal surfaces, such as $(1\bar{1}0)$ and $(11\bar{2})$ surfaces, by using relaxed slab models within density-functional theory (DFT). We find that the topological Dirac surface states for the two side surfaces have entirely different spin and spin-orbital textures from each other and from those of the (111) surface due to different symmetries of those side surfaces and the surface reconstruction. Our results are distinct from those of the literature [129–131]. For the $(1\bar{1}0)$-surface slab, a topological surface-state Dirac cone is formed at Γ ($k = 0$) with strongly anisotropic Fermi velocity, and the spin texture of the Dirac cone reveals Rashba-type features combined with Dresselhaus-type SOC. For the $(11\bar{2})$-surface slab, a Dirac point at either the Γ or Y point appears below the Fermi level E_{F}. Additionally, the spin texture of the Dirac cone for the $(11\bar{2})$ surface near Γ distinctively differs from that of the (111) and $(1\bar{1}0)$ surfaces: (i) The spin polarization is dominantly normal to the mirror symmetry axis; (ii) The upper Dirac cone reveals Dresselhaus-like spin texture, whereas the lower Dirac cone does not; (iii) There is a significant out-of-plane spin polarization except for the mirror symmetry axis. Our findings can be observed in spin-resolved angle-resolved photoemission spectroscopy.

We describe the symmetries of the $(1\bar{1}0)$ and $(11\bar{2})$ surfaces and reiterate the main differences between our approach and the method used in the literature, Refs. 129–131, in 2.2. Then our slab geometries and the calculation method follow in 2.3. The calculated results and analysis for the $(1\bar{1}0)$ and $(11\bar{2})$ slabs are separately presented in 2.4 and 2.5, respectively, since they show different spin textures and electronic structures. The differences between our results and the literature are also mentioned in 2.4 and 2.5, followed by conclusions in

2.6.

2.2 Symmetries of Side Surfaces

To cleave the $(1\bar{1}0)$ and $(11\bar{2})$ surfaces, the chemical bonding between neighboring Bi and Se atoms must be broken. There is only one kind of surface termination for each side surface. For both $(1\bar{1}0)$- and $(11\bar{2})$-surface slabs, the supercell or unit cell consists of two Bi and three Se atoms per atomic layer, as shown in the area confined by the lattice vectors (white arrows) in Fig. 2.1(b) and (c), respectively. Since the chemical bonding is broken, the surface reconstruction effect may be significant. However, each side surface is neutral in charge and thus passivating layers are not added to the slabs. Both slabs maintain time-reversal symmetry and inversion symmetry. Henceforth, the (x, y, z) coordinates are local coordinates rather than the crystal coordinates, unless specified otherwise; the z axis is selected to be perpendicular to the surface of interest.

The $(1\bar{1}0)$ slab has stacking in units of two atomic layers, as illustrated in Fig. 2.1(a). The x axis is chosen to be parallel to the [111] direction, as shown in Fig. 2.1(b). The $(1\bar{1}0)$ surface has C_2 symmetry about the z axis ($x \to -x$, $y \to -y$) and it lies in the mirror plane. The un-optimized $(1\bar{1}0)$ slab has perfect C_2 symmetry, which is only slightly broken upon surface reconstruction. For the $(11\bar{2})$ slab, we choose the y axis to be parallel to the [111] direction and the x axis to align along the $[\bar{1}10]$ direction, as shown in Fig. 2.1(c). The $(11\bar{2})$ slab has stacking in units of six atomic layers, as illustrated in Fig. 2.1(a). The $(11\bar{2})$ surface has mirror symmetry across the y axis ($x \to -x$, $y \to y$), and this symmetry is retained even after geometry relaxation. Therefore, the $(1\bar{1}0)$ and $(11\bar{2})$ surfaces have distinct spatial symmetries.

We now compare the above spatial symmetries of the side surfaces with symmetries considered in the previous theoretical works [129–131]. In the literature, the spin textures of the side surfaces were derived starting from the effective bulk model Hamiltonian consisting of only linear and quadratic terms in momentum k. Higher-order terms than the quadratic terms were neglected in the model Hamiltonian. This simplification allows continuous rotational symmetry about the crystal c axis for the bulk and the (111) surface, implying that all normal surfaces to the (111) surface are identical in terms of symmetry. However, the bulk has only discrete symmetries [59] (rather than the continuous rotational symmetry), such as C_3 symmetry about the c axis, C_2 symmetry about the $[1\bar{1}0]$ direction, and mirror symmetry about the $(1\bar{1}0)$ plane. See Fig. 2.1(a). The crystal symmetries can be properly addressed and incorporated in the side surfaces only when the higher-order terms in k are included in the model Hamiltonian prior to rotations of the spatial and spin coordinates. In contrast to the literature, our DFT calculations of the $(1\bar{1}0)$ and $(11\bar{2})$ slabs include the aforementioned correct discrete symmetries of the side surfaces as well as the surface reconstruction effect.

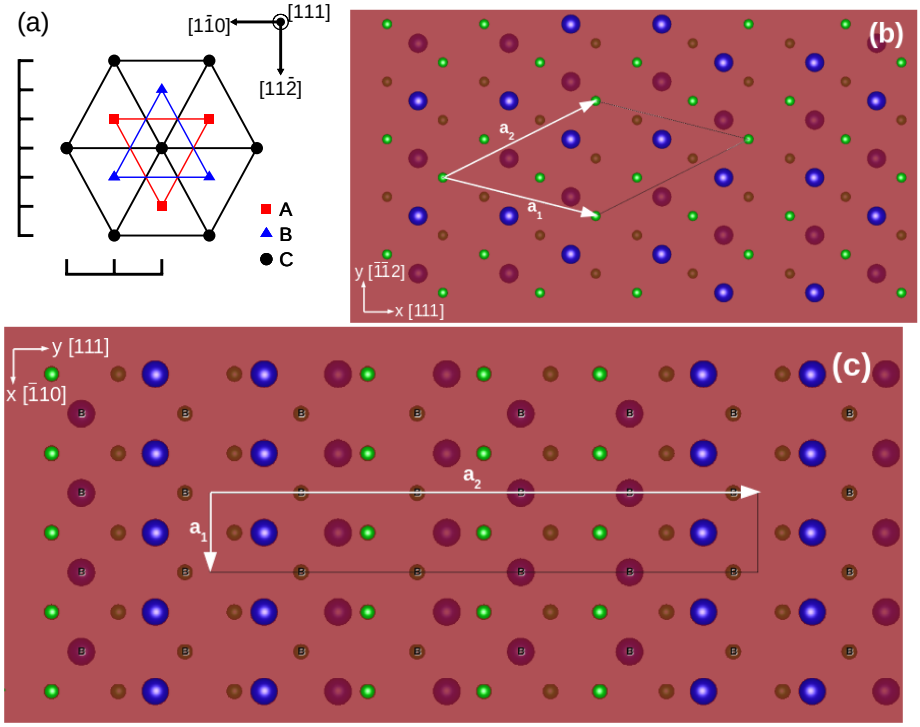

Figure 2.1: Geometry of bulk Bi_2Se_3 and its side surfaces. (a) Top view of bulk Bi_2Se_3 crystal along the crystal c axis. The bulk rhombohedral structure has ABC stacking that organizes into quintuple-layers Se-Bi-Se-Bi-Se. The stacking of the normal surfaces is emphasized by the hashed rulers on the left half of the figure. (b)-(c) Top views of $(1\bar{1}0)$ and $(11\bar{2})$ surfaces of Bi_2Se_3, which are normal to the (111) surface. Here $(1\bar{1}0)$ and $(11\bar{2})$ surfaces are equivalent to $(11\bar{2}0)$ and $(1\bar{1}00)$ in the hexagonal lattice, respectively. Large, blue circles are Bi and small, green circles are Se. $(1\bar{1}0)$ stacks with two inequivalent atomic layers in the unit cell and $(11\bar{2})$ stacks with six inequivalent atomic layers in the unit cell. In both cases, the topmost atomic layer is brightly colored, and in the latter case the second atomic layer is dull and labeled while the third atomic layer is merely dull. For $(11\bar{2})$, the three other inequivalent atomic layers are accessible by repeating the three shown atomic layers, but with a shift of $\frac{1}{2}\mathbf{a}_1$. In (b) and (c) the lattice vectors $\mathbf{a}_1$ and $\mathbf{a}_2$ are shown with the local x and y axes in the plane. (b) and (c) are drawn by using visualization program VESTA [132].

2.3 Slab Geometries and Calculation Method

We first construct the $(1\bar{1}0)$ and $(11\bar{2})$ slabs with thicknesses of 29 and 49 atomic layers, respectively, by using the bulk experimental lattice constants $a = 4.143$ and $c = 28.636$ Å [133]. For the $(1\bar{1}0)$ and $(11\bar{2})$ slabs, the distances between adjacent atomic layers are $a/2$ =2.0715 Å and $\sqrt{3}a/6$ =1.196 Å, respectively, before the geometry optimization or surface reconstruction. These slabs are equivalent to the $(1\bar{1}0)$ slab consisting of 14 units and an additional atomic layer and to the $(11\bar{2})$ slab comprising 8 units and one more atomic layer, respectively. We choose these thicknesses in order to keep inversion symmetry and to reduce the surface hybridization. Since both slabs have non-polar surfaces, we do not include passivating layers in the slabs. A vacuum layer of $4a$ (16.6 Å) is included in the supercell in order to avoid artificial interactions between neighboring supercells. The relaxed $(1\bar{1}0)$ and $(11\bar{2})$ slabs have thicknesses of 5.87 nm and 5.80 nm, respectively.

To relax the geometry and obtain band structures, we use a DFT code, VASP [134], within the Perdew-Burke-Ernzerhof generalized-gradient approximation (GGA) [7] for an exchange-correlation functional, with the projector-augmented-wave (PAW) pseudopotentials [11]. We take into account SOC in a self-consistent manner within DFT. A cutoff kinetic energy is set to 250 eV and the total energy converges down to 1×10^{-5} eV. For the $(1\bar{1}0)$ slab, the geometry is optimized by allowing the top nine and bottom nine atomic layers to relax until the maximum residual force is less than 0.1 eV/Å. The k-points of $7\times7\times1$ are sampled including Γ within the Monkhorst-Pack scheme. For the $(11\bar{2})$ slab, the geometry is optimized by allowing the top seven and bottom seven atomic layers to relax to the same force criterion. The k-points of $11\times3\times1$ are sampled including Γ within the Monkhorst-Pack scheme. For both surfaces, we check that our findings are not affected by further geometry relaxation with a more stringent force criterion, by relaxing more atomic layers, or by increasing the number of sampled k-points. At the examined thicknesses, hybridization between the top and bottom surface states is small, i.e. on the order of meV, for both slabs (for details, see 2.4 and 2.5).

The surface states are identified from our calculated band structures by examining electron density localization as a function of the z coordinate normal to a given surface. Surface states have electron density localized at the top or bottom surface within fifteen atomic layers by more than 80% for the $(1\bar{1}0)$ slab, or within ten atomic layers by more than 60% for the $(11\bar{2})$ slab. Small changes of these criteria do not change our identification of the surface states.

2.4 Results and Discussion for $(1\bar{1}0)$ Surface

2.4.1 Electronic Structure: $(1\bar{1}0)$ Surface

Figure 2.2(a) shows our calculated band structure of the un-optimized $(1\bar{1}0)$ slab. The surface Brillouin zone is shown as the inset of Fig. 2.2(b). The large residual forces are found at the z components of the atoms close to the surface and they are on the order of 1 eV/Å. The band structure does not show a well-defined Dirac cone in the vicinity of Γ and E_F. The Dirac-cone candidate bands have quadratic dispersion near Γ, and there are several bands bunched together right below E_F. The candidate bands for the lower Dirac cone have their charge densities strongly localized at the surface within three atomic layers, or 4.143 Å. This is different in character from the candidate band for the upper Dirac cone and implies that these bunched bands derive their surface state nature from the unrelaxed surface structure rather than a topological invariant. The inversion symmetry and time-reversal symmetry dictate that the band structure of the slab must have at least double degeneracy for all momenta.

Upon the geometry relaxation [Fig. 2.2(b)], a doubly degenerate Dirac cone near E_F is clearly identified, with the Dirac point located at Γ. The energy gap between the upper and lower Dirac cone is 3.2 meV at Γ due to the hybridization between the top and bottom surface states. Now the previously bunched bands right below E_F are shifted out of the bulk gap as expected. The decay length of both top-surface and bottom-surface Dirac states is about 30 Å, as shown in Fig. 2.2(c), which is about twice as long as that for the Bi_2Se_3 (111) surface. In both the upper and lower Dirac-cone surface states, Se contributions are dominant over Bi at a ratio of roughly 2.5:1, in contrast to the case of the (111) surface where Bi contributes more than Se at a ratio of 1.5:1 [135]. The dominant orbitals are p_x orbitals corresponding to p_z orbitals in the bulk crystal coordinates. Henceforth in this subsection, we discuss characteristics of the Dirac surface states for the optimized slab only.

The effective Hamiltonian for the p_x-dominated surface states localized at the $(1\bar{1}0)$ surface, in the vicinity of Γ, up to quadratic order is given by

$$\mathcal{H}_1(k) \;=\; E_0(k)I + [v_x k_x \sigma_y - v_y k_y \sigma_x] + \{\alpha_x k_x \sigma_x - \alpha_y k_y \sigma_y\} \tag{2.1}$$

where I is a 2×2 identity matrix, $E_0(k)$ contains a constant term and quadratic terms in k with effective masses, and v_x and v_y are the Fermi velocities along the x and y axes. This Hamiltonian satisfies time-reversal symmetry and the C_2 symmetry ($k_{x,y} \to -k_{x,y}$, $\sigma_{x,y} \to -\sigma_{x,y}$, and $\sigma_z \to \sigma_z$) of the $(1\bar{1}0)$ surface. The square-bracketed terms are Rashba-type SOC terms, and the braced terms are Dresselhaus-type SOC terms that are additionally allowed by the C_2 symmetry. Note that Rashba [136] and Dresselhaus [137] SOC terms are conventionally defined with isotropic coefficients such as $v_x = v_y$ and $\alpha_x = \alpha_y$.

The band structure, Fig. 2.2(b), and the constant energy contours, Fig. 2.3, unambiguously show strong anisotropy in the Fermi velocity. The Fermi velocities along the x and y axes

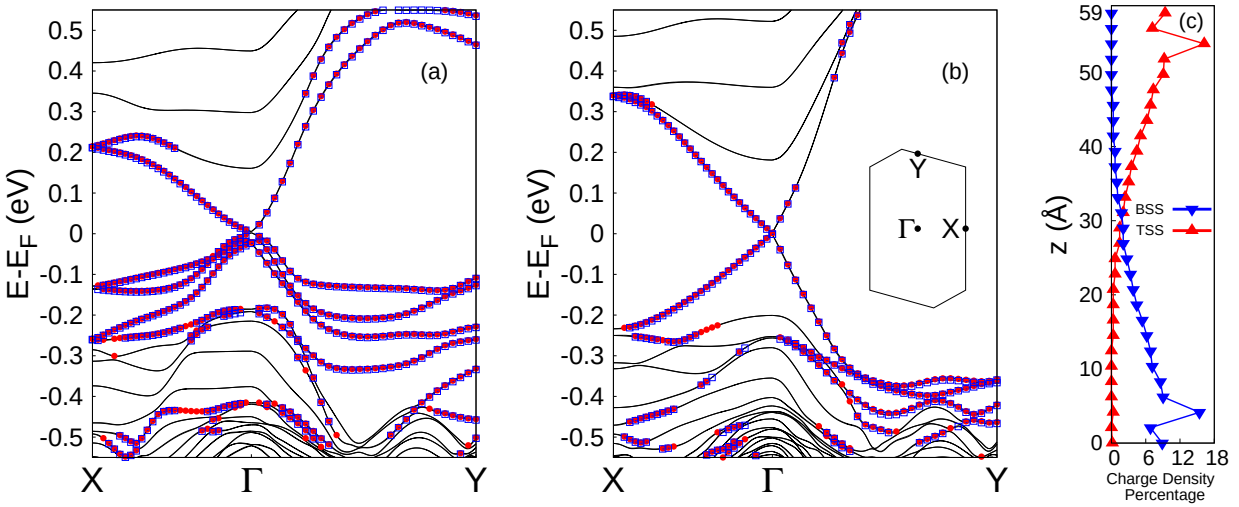

Figure 2.2: Electronic structures of un/optimized $(1\bar{1}0)$ slabs. (a) the un-optimized and (b) the optimized Bi_2Se_3 $(1\bar{1}0)$ slabs, where the top/bottom surface states are identified as circles/squares in red/blue. The Fermi level is zero in (a) and (b). (Inset) The surface-projected first Brillouin zone. (c) Charge density distributions vs vertical coordinate z for the top and bottom surface states in the optimized slab calculated near Γ (at $\vec{k} = (0.003, 0)\ 2\pi/a$ and 4.3 meV below the Dirac point), shown as red and blue, respectively.

would ordinarily be found by fitting the energy eigenvalues of the Dirac surface states in the small k region where only linear terms in k significantly contribute ($0.0015\ 2\pi/a \leq k \leq 0.015\ 2\pi/a$). The constant energy contours show that the ellipses have their principal axes somewhat tilted from the x and y axes even for small k (the clockwise tilting angle of 16°), implying that the linear Rashba-type terms alone would incompletely describe the low-energy physics near Γ for this surface. Including the Dresselhaus-type terms in Eq. (2.1) gives rise to the tilting of the ellipse. These extra linear terms prevent us from extracting the Fermi velocities because the energy eigenvalues E_1 are

$$\begin{aligned} E_1 &= E_0 + \frac{1}{2m_x^\star}k_x^2 + \frac{1}{2m_y^\star}k_y^2 \\ &\quad \pm k\sqrt{u^2\cos^2\phi + q^2\sin^2\phi - 2r^2\sin\phi\cos\phi}, \qquad (2.2) \\ u^2 &= v_x^2 + \alpha_x^2, \quad q^2 = v_y^2 + \alpha_y^2, \quad r^2 = v_y\alpha_x + v_x\alpha_y, \qquad (2.3) \end{aligned}$$

where E_0 is a constant term, $m_{x,y}^\star$ are the effective masses, and ϕ is an azimuthal angle in the $k_x - k_y$ plane measured counter-clockwise from the k_x-axis. Hence any fitting procedure will be unable to extract the set of four parameters, $\{v_x, v_y, \alpha_x, \alpha_y\}$, from just three equations. However, the u, q, and r values can be found from the fitting of the energy eigenvalues at several different values of ϕ. As evidenced by the energy contours, the ellipse for the lower Dirac cone is somewhat elongated in the major axis direction compared to the upper Dirac

cone. This small particle-hole asymmetry leads to the u value being slightly larger for the unoccupied or upper Dirac cone than for the occupied or lower Dirac cone. Upon averaging the values of each parameter found from fitting at different values of ϕ and averaging across the upper and lower Dirac cones, we find that $u = 1.02 \pm 0.07$ eV·Å, $q = 2.35 \pm 0.03$ eV·Å, and $r = 1.20 \pm 0.03$ eV·Å, where the uncertainties are obtained by considering the small difference between the upper and lower Dirac cones. We can estimate the values of the Fermi velocities and Dresselhaus parameters appearing in Eq. (2.1) by making the assumption that the ratio of the Fermi velocities, (v_x/v_y), is the same as the ratio of the Dresselhaus parameters, (α_x/α_y). With this assumption, the values of the four parameters are as follows in units of eV·Å : $v_x = 0.97 \pm 0.10$, $v_y = 2.23 \pm 0.04$, $\alpha_x = 0.33 \pm 0.04$, and $\alpha_y = 0.74 \pm 0.07$.

2.4.2 Spin and Spin-Orbital Textures: $(1\bar{1}0)$ Surface

Let us first discuss the in-plane spin texture of the Dirac surface states. The arrows in Fig. 2.3 show total in-plane spin textures at the constant energy contours for the upper and lower Dirac cones localized at the top surface that are obtained from spin expectation values of the DFT-calculated surface-state bands. To avoid effects of higher-order terms in k, the spin textures are calculated close to the Dirac point. The total in-plane spin polarization is similar for both the upper and lower Dirac cones and reaches up to 0.51 μ_B, which is about a 25% increase compared to that in the (111) surface. The in-plane spin polarization rotates counter-clockwise (clock-wise) around the Γ point for the upper (lower) Dirac cone. Interestingly, the spin directions neither align parallel to the tangent to the constant energy contours nor obey perpendicular momentum-locking along the k_x and k_y axes, despite some similarity to Rashba-like features. Here the perpendicular spin-momentum locking means $\mathbf{s}_k \cdot \mathbf{k} = 0$, where $\mathbf{s}_k$ is an in-plane spin vector at in-plane momentum $\mathbf{k}$. To understand the origin of our calculated spin texture, we examine five representative cases: (i) $v_x \neq v_y$ and $\alpha_x = \alpha_y = 0$, (ii) $v_x = v_y$ and $\alpha_x = \alpha_y$, (iii) $v_x = v_y$ and $\alpha_x \neq \alpha_y$, (iv) $v_x \neq v_y$ and $\alpha_x = \alpha_y$, (v) $v_x \neq v_y$, $\alpha_x \neq \alpha_y$. Our analysis shows that the spin directions do not align tangent to the energy contours *away* from either the k_x and k_y axes or the principal axes when the contours are elliptic such as in all the five cases. However, the perpendicular spin-momentum locking still persists along either the k_x and k_y axes or the principal axes, only when the Fermi velocity is isotropic or there are no Dresselhaus-type terms, i.e., cases (i)-(iii). Therefore, we suggest that our calculated spin texture is attributed to a combined effect of anisotropic Fermi velocity with the Dresselhaus-type terms.

The detailed calculations of the implications of the calculated spin texture on transport properties are beyond the scope of this chapter. There have been multiple studies of observations of spin accumulations of Bi_2Se_3 thin films driven by spin-unpolarized charge currents, especially when layered on a ferromagnetic material. [43, 138] Due to the traditional perpendicular spin-momentum locking associated with the surface states of the (111) slab, the spin accumulation direction was always perpendicular to the direction of the carrier momentum. If similar experiments are performed for this side surface, the observed spin accumulation

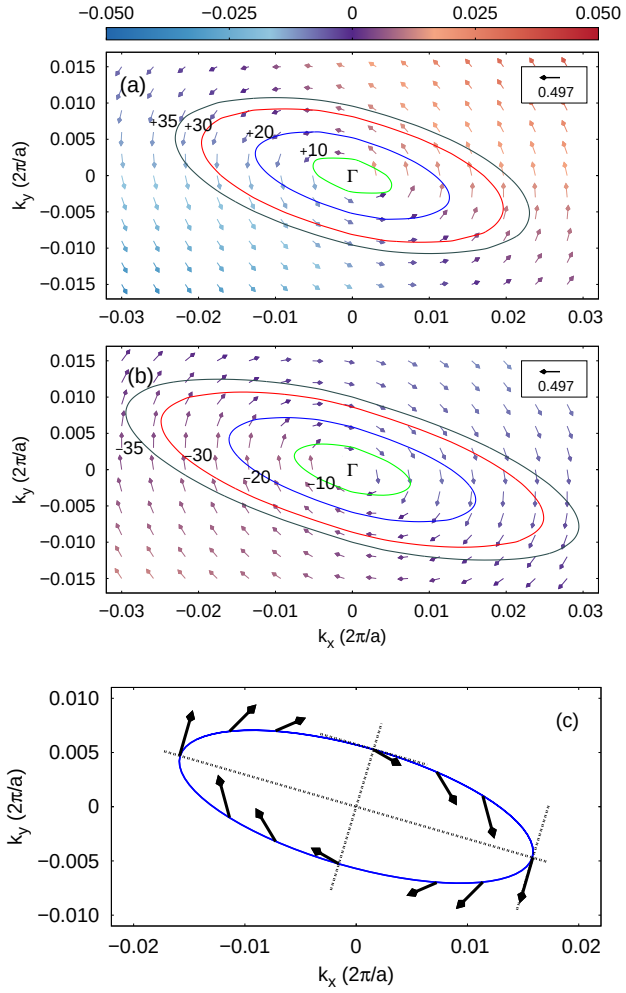

Figure 2.3: Spin-texture of the (1$\bar{1}$0) Dirac cone surface states localized at the top surface for the optimized (1$\bar{1}$0) slab at the constant energy contours. The length of the vectors indicates in-plane spin polarization, and out-of-plane spin polarization is indicated by the color scale. Constant energy contours corresponding to ± 10, 20, 30, and 35 meV with respect to the Dirac point (Fermi level) are overlaid in green, blue, red, and black, respectively. (a) The upper Dirac cone and (b) the lower Dirac cone. (c) A schematic representation of the in-plane spin directions along the -20 meV energy contour of the lower Dirac cone. The spins are calculated using DFT at points very near to the energy contour, and the principal axes are shown, as are the tangents to the energy contour at points along the principal axes.

direction may not be perpendicular to the carrier momentum direction.

Another noticeable effect is found in the in-plane spin-orbital texture. The arrows in Fig. 2.4(a)-(c) show p_x, p_y, and p_z orbital projections of the spin expectation values for the upper Dirac cone shown in Fig.3(a). The spin-orbital texture of the lower Dirac cone is opposite to that of the upper Dirac cone. We find that the p_x and p_z orbitals show the same spin circulation directions, whereas the spin expectation values arising from the p_y orbitals reveal Dresselhaus-like spin texture, i.e., rotates *away* from the Γ point. However, since the contribution of the p_x orbitals is dominant, the total spin texture follows that of the p_x orbitals. The Se and Bi contributions to the spin textures are not the same as each other; aside from Se and Bi contributing to the spin polarization at a ratio of approximately 2.5:1, the spin directions from the Bi and Se sublattices are not parallel to each other for most ϕ values [Fig. 2.4(d)-(e)]. For the Bi sublattice the y components of spin are dominant in the plane, whereas for the Se sublattice there is no such tendency.

The color scale in Fig. 2.3 shows the total out-of-plane spin textures for the upper and lower Dirac cones localized at the top surface. For the out-of-plane spin component, we find that the spin polarization is greater than 0.01 μ_B even at small k values on the order of 0.01 $2\pi/a$, where contributions of higher-order terms are expected to be negligible. The magnitude of out-of-plane spin polarization increases slowly with increasing k. Perfect C_2 symmetry combined with time-reversal symmetry does not allow an out-of-plane spin component from any order of the in-plane momenta in the effective Hamiltonian, Eq. (2.1). Therefore, the z component of spin must originate from slightly broken C_2 symmetry, which we find is attributed to the geometry optimization. For example, for the un-optimized $(1\bar{1}0)$ slab which has perfect C_2 symmetry, the upper Dirac-cone candidate band does not have the z component of spin. Considering this observation, we expect that small linear terms such as $(\gamma_x k_x + \gamma_y k_y)\sigma_z$ are allowed upon the slightly broken C_2 symmetry. These additional linear terms would only affect the energy eigenvalues through modification of u^2 to $(v_x^2 + \alpha_x^2 + \gamma_x^2)$ and q^2 to $(v_y^2 + \alpha_y^2 + \gamma_y^2)$ without any change of r^2 in Eq. (2.3). Thus, the effect of γ_x and γ_y on the energy eigenvalues is evidently much less than that of α_x and α_y. Furthermore, since the values of γ_x and γ_y are expected to be much smaller than the values of α_x and α_y, in order to obtain the values of γ_x and γ_y from the fitting, the higher-order terms in the bulk Hamiltonian need to be included before rotations of the spatial and spin coordinates. This is beyond the scope of our current work. Notice that the spin and spin-orbital textures of the Dirac cones aforementioned in this subsection are opposite to those of the Dirac cones localized at the bottom surface in the sense that both the spin circulation directions and the out-of-plane spin polarization are opposite to each other. Therefore, the existence of the z component of spin does not break time-reversal symmetry in the slab because the z component of spin at a given k value localized at the top surface exactly cancels out with that localized at the bottom surface.

We now compare our calculated spin textures to those predicted by Refs. 129–131, where the $(1\bar{1}0)$ and $(11\bar{2})$ surfaces are supposed to show identical spin textures, as previously stated in 2.2. In the literature, the continuous rotational symmetry in the bulk Hamiltonian, en-

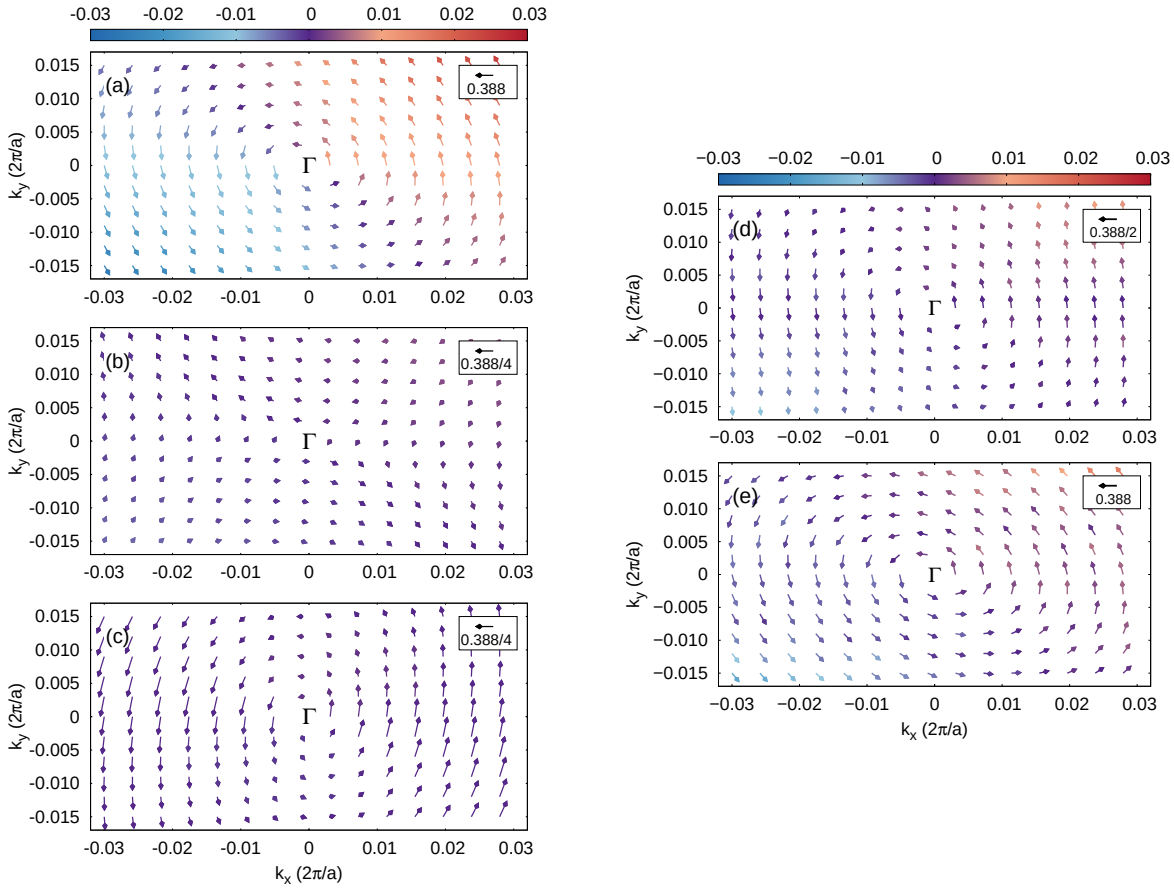

Figure 2.4: Spin-orbital texture of the $(1\bar{1}0)$ Dirac cone surface states localized at the top surface for the $(1\bar{1}0)$ slab, projected onto the (a) p_x, (b) p_y, and (c) p_z orbitals. Note the in-plane scale for (a) differs from those for (b) and (c). Sublattice decomposed spin textures of the upper Dirac cone localized at the top surface: (d) Bi sublattice, and (e) Se sublattice. In (a)-(e) the color scales are for the out-of-plane spin component. Note the in-plane scale for (d) differs from that of (e).

forced by keeping only linear and quadratic terms in k, dictates that the spin polarization be perpendicular to the mirror symmetry plane at un-tilted elliptic constant energy contours for all the surfaces normal to the (111) surface. In addition, the Se and Bi sublattices were assumed to equally contribute to the Dirac surface states. However, as shown in Fig. 2.1(b), the $(1\bar{1}0)$ surface does not have mirror symmetry. Instead it has C_2 symmetry about the z axis. Our DFT-calculated Dirac surface states form elliptic constant energy contours tilted by about 16° from the k_x axis, and our DFT-calculated spin and spin-orbital textures completely differ from those of the literature. The surface reconstruction effect included in the DFT calculation is found to be important for Dirac surface states, although the geometry relaxation maintains the spatial symmetry to a high degree. The qualitative differences between our result and the literature are due to the fact that our DFT calculations capture the correct spatial symmetry and the surface reconstruction effect of the $(1\bar{1}0)$ surface, whereas the model Hamiltonian in the literature does not.

2.5 Results and Discussion for $(11\bar{2})$ Surface

2.5.1 Electronic Structure: $(11\bar{2})$ Surface

Due to inversion symmetry and time-reversal symmetry, the band structure of the slab has at least double degeneracy for all momenta. At the time-reversal invariant momenta (X, Y, and Γ in the inset of Fig. 2.5) the bands have fourfold degeneracy. Similarly to the $(1\bar{1}0)$ slab, we first compare the band structures of the un-optimized and optimized $(11\bar{2})$ slabs, as shown in Fig. 2.5(a) and (b), respectively. The surface Brillouin zone is shown as the inset of Fig. 2.5(b). The un-optimized slab has large residual forces on the atoms close to the top and bottom surfaces and the maximum force is on the order of 1 eV/Å. The band structure of the un-optimized slab does not clearly show Dirac cones near Γ, despite Dirac-like cones at the Y point. The bands crossing the Fermi level at Γ quickly flatten out and group with other bands as k increases. Henceforth, we consider only the optimized slab.

Near the Γ point

The band structure of the optimized $(11\bar{2})$ slab is distinct from those of the $(1\bar{1}0)$ and (111) slabs in many ways, although the $(11\bar{2})$ slab holds topological surface states, as it should in the presence of time-reversal symmetry. The complexity of the band structure of the $(11\bar{2})$ slab in relation to those of the $(1\bar{1}0)$ and (111) slabs is likely influenced by the lower symmetry and the presence of twelve broken covalent bonds, whereas there are only eight broken covalent bonds in the $(1\bar{1}0)$ surface and zero in the (111) surface (due to the van der Waals coupled quintuple layers along the crystal c-axis). Let us first discuss the upper and lower Dirac cones near E_F with the Dirac point at Γ, as shown in Fig. 2.5(b). The Dirac point at Γ, E_Γ^{DP}, is located at 0.12 eV below E_F, due to the surface potential. This indicates

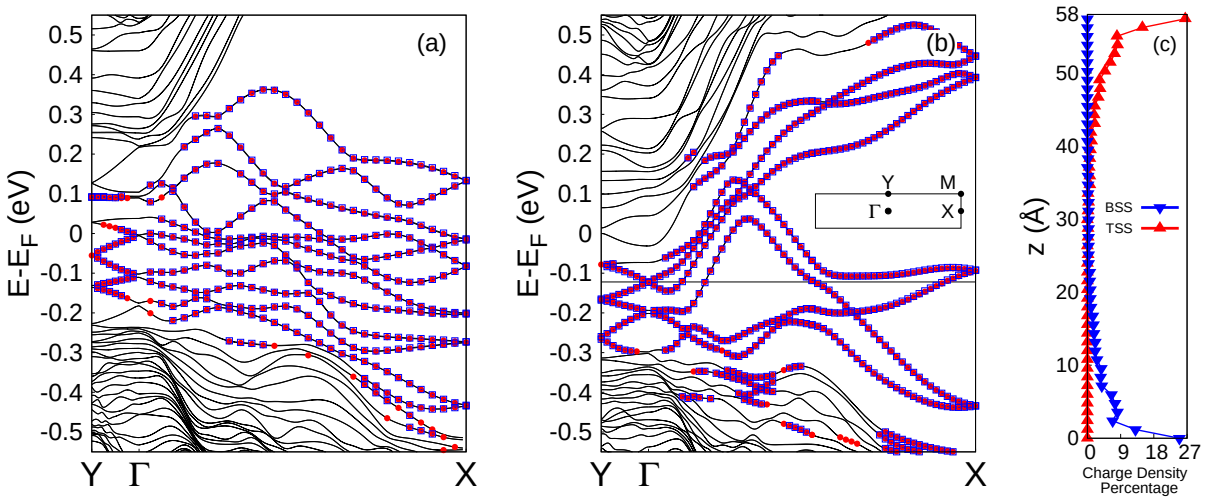

Figure 2.5: Electronic structure of the un/optimized (11$\bar{2}$) slabs. (a) the unoptimized and (b) the optimized Bi_2Se_3 (11$\bar{2}$) slabs, where the top/bottom surface states are identified as circles/squares in red/blue. The horizontal line is to guide the eye at $E_\Gamma^{\rm DP} = -0.12$ eV. (Inset) The surface first Brillouin zone for the (11$\bar{2}$) slab. (c) Charge density distributions vs vertical coordinate z for the top and bottom surface states in the optimized slab calculated near Γ (at $\vec{k} = (0.009, 0)\ 2\pi/a$ and 8.7 meV below the Dirac point), shown as red and blue, respectively.

that the surface reconstruction effect is significant, although the (11$\bar{2}$) surface is non-polar. The energy gap between the upper and lower Dirac cones is 1.4 meV caused by the small surface hybridization. The decay length of the surface states is about 15 Å, which is much shorter than the (1$\bar{1}$0) surface but comparable to that for the (111) surface [Fig. 2.5(c)]. The p_y orbital dominantly contributes to the surface states. Similarly to the (1$\bar{1}$0) slab, Se contributions are dominant over Bi contributions at a ratio of 2.5:1 for both the upper and lower Dirac cones.

Considering the symmetries of the (11$\bar{2}$) surface, the effective Hamiltonian for the p_y-dominated surface states up to quadratic order, in the vicinity of $E_\Gamma^{\rm DP}$, is given by

$$\mathcal{H}_2(k) \;=\; E_0(k)I + [v_x k_x \sigma_y - v_y k_y \sigma_x] + \{\gamma k_x \sigma_z\}, \tag{2.4}$$

where the braced term is an additional linear term allowed by the mirror symmetry of the (11$\bar{2}$) surface about the y axis ($k_x \to -k_x$, $k_y \to k_y$, $\sigma_x \to \sigma_x$, and $\sigma_{y,z} \to -\sigma_{y,z}$).

Figure 2.6 (c) and (d) show our calculated constant energy contours above and below $E_\Gamma^{\rm DP}$, respectively, for the states localized at the top surface. At low energies or energies up to 10 meV above or below the Dirac point, the contours are vertically elongated ellipses for both the upper and lower Dirac cones. However, at high energies or energies sufficiently away from the Dirac point, the size and shape of the contours for the upper Dirac cone differ from

those for the lower Dirac cone. The upper Dirac cone starts to have rectangular-shaped contours from 15 meV above the Dirac point, while the lower Dirac cone retains the same elliptic shape. Therefore, in the case of low energies we fit our DFT-calculated surface-state bands to the energy eigenvalues as a function of k and ϕ for $0.0015\ 2\pi/a \leq |k| \leq 0.015\ 2\pi/a$, with two parameters $s \equiv \sqrt{v_x^2 + \gamma^2}$ and v_y. The energy eigenvalues E_2 of Eq. (2.4) are

$$E_2 \;=\; E_0 + \frac{1}{2m_x^\star}k_x^2 + \frac{1}{2m_y^\star}k_y^2 \pm k\sqrt{s^2\cos^2\phi + v_y^2\sin^2\phi}. \tag{2.5}$$

Upon averaging the values of each parameter found from fitting at different values of ϕ and averaging across the upper and lower Dirac cones, we find that $s = 0.69 \pm 0.07$ eV·Å and $v_y = 0.53 \pm 0.05$ eV·Å. This fitting result is consistent with our DFT-calculated energy contours at low energies. We cannot separately obtain the values of v_x and γ unless the out-of-plane spin polarization is fitted. However, as will be discussed in 2.5.2, we cannot perform a quantitative fitting of the out-of-plane spin polarization based on Eq. (2.4) due to the complex spin texture.

Other than the Γ point

In addition to the Dirac point at Γ, we find a pair of Dirac cones slightly above and below E_Γ^{DP} at the Y point and multiple crossings of the surface states between Γ and X near E_F, as shown in Fig. 2.5(b). All of the identified surface states appearing not near Γ, also have a decay length comparable to those near Γ, as shown in Fig. 2.5(c). The Dirac points at Y with energies of 0.08 eV and 0.17 eV below E_F are referred to as $E_{Y,\mathrm{high}}^{\mathrm{DP}}$ and $E_{Y,\mathrm{low}}^{\mathrm{DP}}$, respectively. The energy gaps at the former and latter Dirac points are 2.6 meV and 1.8 meV, respectively. The crossings of the states at X and $(k_x, k_y) = (0.318, 0)\ 2\pi/a$ (around 0.20 eV below E_F) are not associated with Dirac cones because their dispersion relations are essentially flat rather than linear along the k_y axis (not shown).

Figures 2.6(b), (e), and (f) show constant energy contours of the states localized at the top surface below $E_{Y,\mathrm{high}}^{\mathrm{DP}}$ and above and below $E_{Y,\mathrm{low}}^{\mathrm{DP}}$ at the Y point, respectively. The flat Dirac cone above $E_{Y,\mathrm{high}}^{\mathrm{DP}}$ prevents us from obtaining energy contours. Now at about 10 meV or farther away from $E_{Y,\mathrm{low}}^{\mathrm{DP}}$, the energy contours of the upper Dirac cone noticeably differ from those of the lower Dirac cone. The upper Dirac cone has horizontally elongated elliptic or rectangular contours, whereas the lower Dirac cone has vertically elongated elliptic contours.

2.5.2 Spin and Spin-Orbital Textures: $(11\bar{2})$ Surface

Near the Γ point

We first present our analysis of the spin texture of the upper and lower Dirac cones localized at the top surface near Γ, as shown in Figs. 2.6(c) and (d). This spin texture is opposite to

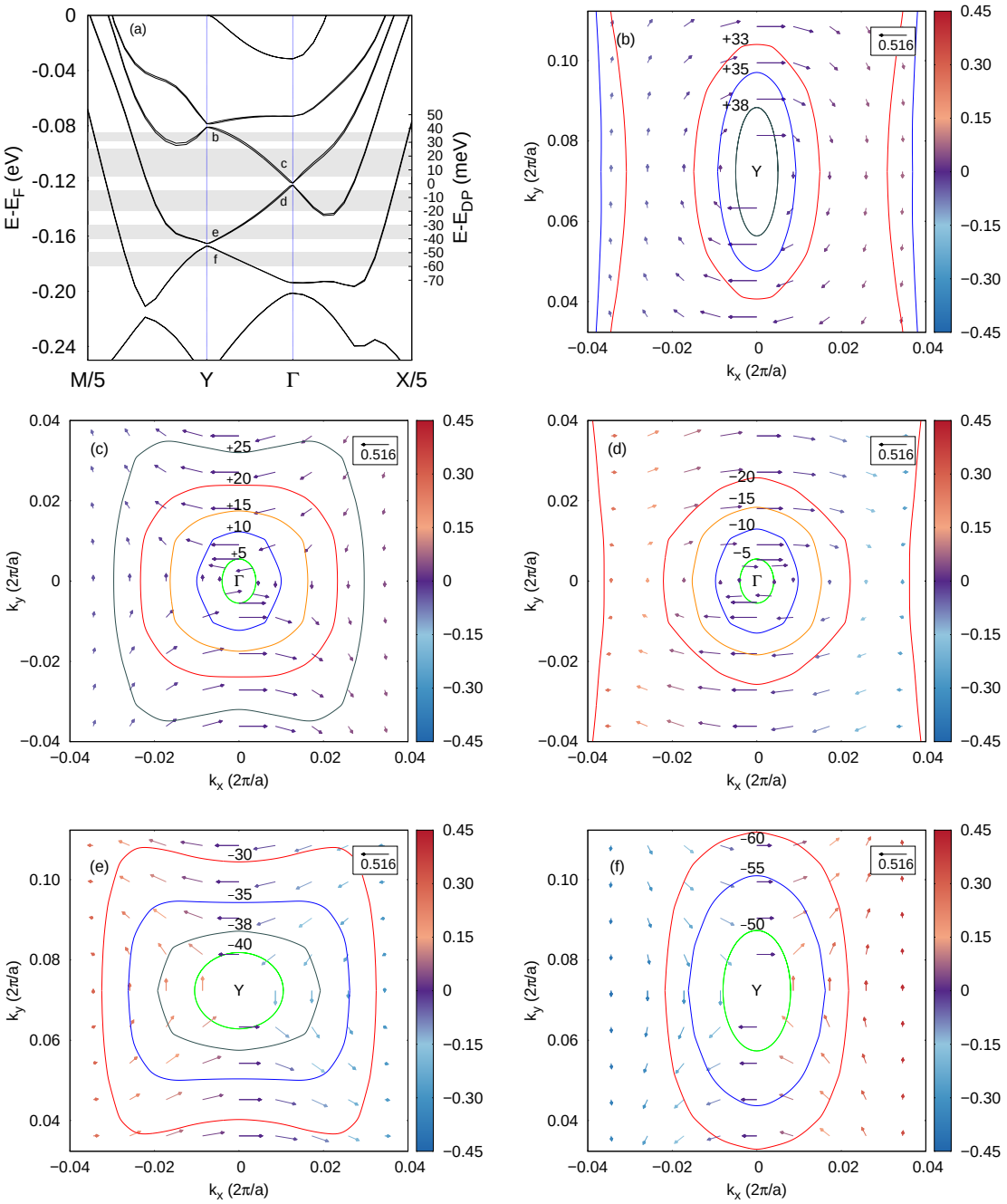

Figure 2.6: Constant energy contours of the (11$\bar{2}$) slab. (a) Band structure centered about the Dirac point at Γ and the two Dirac points at Y. Regions from which constant energy contours are drawn are shown in gray, along with the corresponding figure label. (b-f) Total in-plane and out-of-plane spin textures at constant energy contours for the states localized at the top surface of the optimized (11$\bar{2}$) slab: (b) the lower Dirac cone at $E^{\mathrm{DP}}_{\mathrm{Y,high}}$, (c) the upper Dirac cone at Γ, (d) the lower Dirac cone at Γ, (e) the upper Dirac cone at $E^{\mathrm{DP}}_{\mathrm{Y,low}}$, and (f) the lower Dirac cone at $E^{\mathrm{DP}}_{\mathrm{Y,low}}$. In (b)-(f) the numbers at the contours indicate energies relative to the Dirac point at Γ, and the arrows at the contours and the color scale represent the in-plane and out-of-plane spin components, respectively.

that of the Dirac cones localized at the bottom surface. Overall, the spin textures of both Dirac cones reveal dominant x components of spin for $|k_x| < 0.02\ 2\pi/a$. Along the k_y axis ($k_x = 0$) the spin is polarized along the x axis with the magnitude 0.52 μ_B at $k_y = 0.009\ 2\pi/a$ and it increases to 0.54 μ_B at $k_y = 0.063\ 2\pi/a$. However, there is a fundamental difference in the spin texture between the upper and lower Dirac cones. For the upper Dirac cone the spin polarization circulates clockwise around the Y point (Dresselhaus-like), whereas for the lower Dirac cone the spin rotates again clockwise around the Γ point. This difference has not been observed for the (111) and $(1\bar{1}0)$ surfaces. Compare Fig. 2.6(c) to Fig. 2.3(a). For $|k_x| > 0.02\ 2\pi/a$, along the k_x axis, the in-plane spin polarization of both Dirac cones becomes very small.

For a better understanding of the aforementioned spin texture, we examine the spin polarization projected onto the p_x, p_y, and p_z orbitals for each cone, as shown in Fig. 2.7. For both Dirac cones the p_y orbital contributes most to the spin texture, while the p_x orbital contributes least. The different in-plane spin circulations for the upper and lower Dirac cones are clearly shown in the p_y orbital projection. However, that is not the case for the p_x and p_z orbital projections. Interestingly, the p_z-orbital projection shows the spin circulation around the Y point (Dresselhaus-like) for both the upper and lower Dirac cones, whereas the p_x-orbital projection reveals the circulation around the Γ point (Rashba-like). Along the k_y axis the spin polarizations of the p_y and p_z orbitals are opposite to that of the p_x orbital. Additionally, we separate the spin polarization of the Bi atoms from that of the Se atoms, as shown in Fig. 2.8. The contribution of the Se atoms is greater than that of the Bi atoms. The Se sublattice shows the spin circulating around the Y (Γ) point for the upper (lower) Dirac cone, just like the total spin polarization. But the Bi sublattice reveals the spin winding around the Y point (Dresselhaus-like) for both the upper and lower Dirac cones.

In addition to the in-plane spin polarization, our DFT calculation shows a small out-of-plane spin polarization on the order of 0.01 μ_B even near Γ that is apparent from the color scale of Figs. 2.7 and 2.8. The out-of-plane spin component appears in the whole plane except for the k_y axis. This is consistent with the reasoning that the out-of-plane spin polarization arises from the $\gamma k_x \sigma_z$ term in Eq. (2.4). An estimate of this term from the fitting of our DFT-calculated spin expectation values is not feasible due to the aforementioned complex dependence of the total spin polarization on k and ϕ.

We now briefly mention the comparison of our result to the prediction made by Refs. 129–131. The prediction states that for any normal surface the spin polarization is strictly perpendicular to the [111] direction and it is in the surface plane at un-rotated elliptic constant energy contours. Refs. 130, 131 suggest that the Bi sublattice gives rise to the Rashba spin texture and the Se sublattice the Dresselhaus spin texture, which does not agree with our DFT result for the upper Dirac cone and is opposite to that for the lower Dirac cone. If the Bi and Se sublattices contribute equally, the prediction in Ref. 129 agrees with that in Refs. 130, 131. Hence, the result in Refs. 129–131 captures only the overall feature of the in-plane spin polarization of our DFT-calculated Dirac surface states near Γ

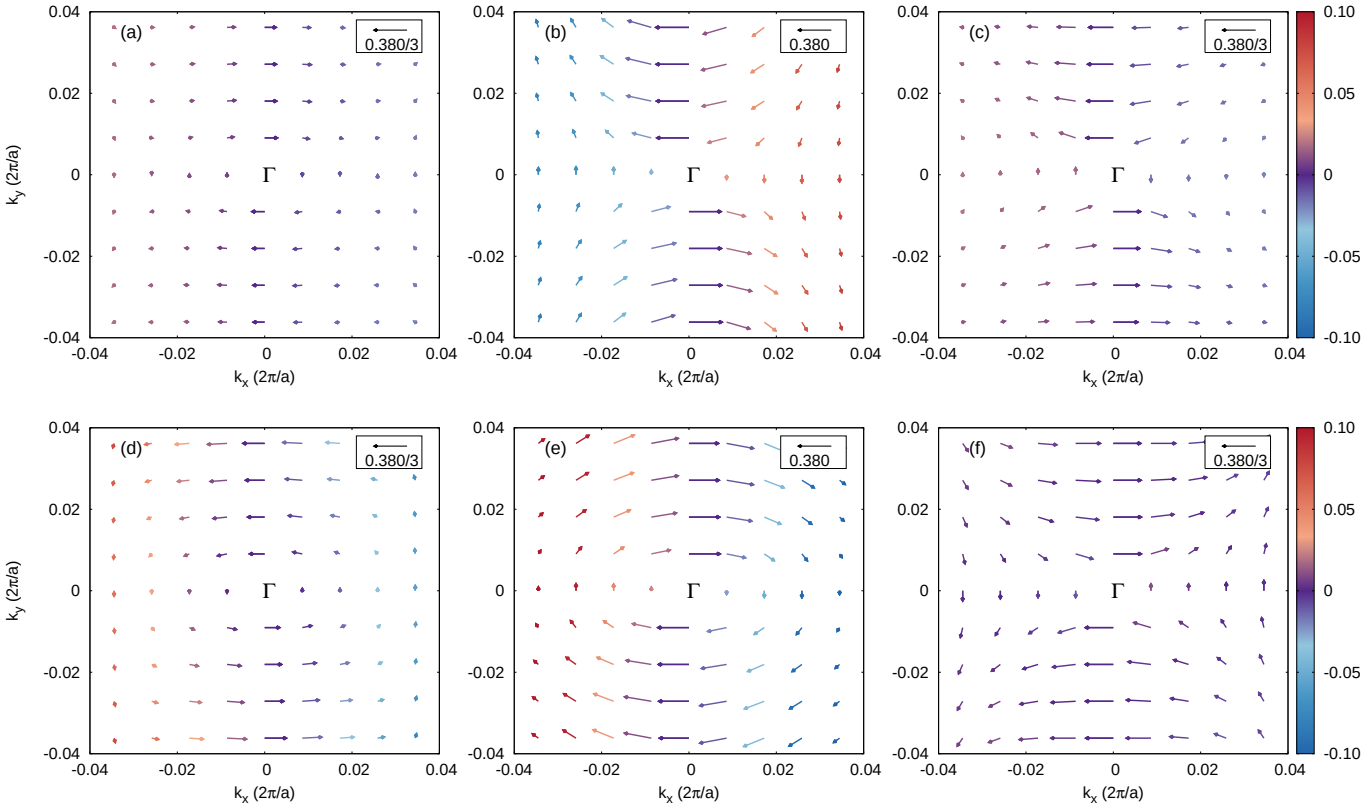

Figure 2.7: Spin-orbital texture near the Γ point. Orbitally decomposed spin textures of (a-c) the upper Dirac cone and (d-f) the lower Dirac cone of the surface states localized at the top surface near Γ for the $(11\bar{2})$ slab shown in Fig. 2.6(c,d); (a) and (d) for the p_x orbital, (b) and (e) for the p_y orbital, and (c) and (f) for the p_z orbital. The in-plane spin polarization is given by the magnitude of the arrows, and the out-of-plane spin polarization is given by the color-scale. Note the different in-plane scale in (b) and (e) for the p_y orbital from the other in-plane scales.

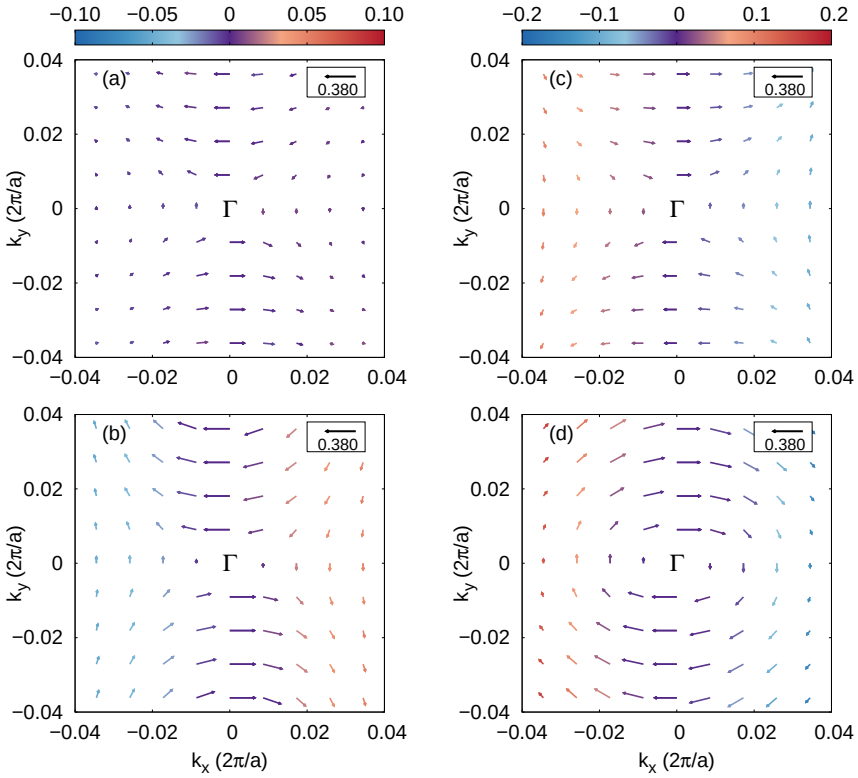

Figure 2.8: Sublattice decomposed spin textures of (a,b) the upper Dirac cone and (c,d) the lower Dirac cone of the surface states shown in Fig. 2.6(c,d): (a,c) Bi sublattice and (b,d) Se sublattice. The meanings of the in-plane and out-of-plane spin polarization scales are the same as those in Fig. 2.7.

for the $(11\bar{2})$ surface. The literature could not predict the additional Dirac points at the Y point. Note that the Hamiltonian used in the literature and Eq. (2.4) have mirror symmetry, while Eq. (2.1) does not. The absence of mirror symmetry in the $(1\bar{1}0)$ surface makes the prediction of the literature inapplicable to the $(1\bar{1}0)$ surface.

Near the Y point

We discuss the spin and spin-orbital textures of the Dirac cones localized at the top surface near the Y point. The arrows in Fig. 2.6(b), (e), and (f) show the spin textures of the lower Dirac cone at $E^{\mathrm{DP}}_{Y,\mathrm{high}}$ and the upper and lower Dirac cones at $E^{\mathrm{DP}}_{Y,\mathrm{low}}$, respectively. The former lower Dirac cone circulates clockwise around the Y point with dominant x components of spin along the k_y axis, similarly to the lower Dirac cone at the Γ point. Immediately away from the k_y axis, the spin polarization of this band is greatly reduced. The spin texture of

the upper Dirac cone at $E^{\mathrm{DP}}_{Y,\mathrm{high}}$ is not obtained since it is difficult to assign constant energy contours due to the flatness of the cone. Now regarding the Dirac cones at $E^{\mathrm{DP}}_{Y,\mathrm{low}}$, the spin at the k_y axis is polarized along the x axis with the magnitude 0.33 μ_B at $k_y = 0.063\ 2\pi/a$ about the Y point. However, right away from the k_y axis, unexpectedly, their spin textures are distinct from those of the Dirac cones at Γ in two ways. Compare Fig. 2.6(c) and (d) to (e) and (f). The first feature is that both the upper and lower Dirac cones now circulate around Γ, similar to the Dresselhaus-type spin texture. The spin polarization of the upper (lower) cone rotates clockwise (counter-clockwise) relative to the Γ point. The second feature is that there is a significant out-of-plane spin polarization except for the k_y axis, at least one order of magnitude greater than that of the Dirac cones near Γ.

To understand these features near $E^{\mathrm{DP}}_{Y,\mathrm{low}}$ at Y, we calculate the spin-orbital texture and Bi and Se sublattice contributions. Figure 2.9(a-c) show the spin polarization projected onto the p_x, p_y, and p_z orbitals of the lower Dirac cone at $E^{\mathrm{DP}}_{\mathrm{Y,low}}$. The p_y orbital contributes most to the spin polarization. The spin polarization arising from the p_y orbitals circulates counter-clockwise around Γ and it has also a significant out-of-plane component. The p_y- and p_z-orbital spin projections are opposite to the p_x-orbital contribution. Both p_y and p_z orbitals show the Dresselhaus-like spin texture. The spin-orbital texture of the upper Dirac cone (not shown) is opposite to that of the lower Dirac cone. Figure 2.9(d-e) shows the Bi and Se sublattice contributions to the spin texture for the lower Dirac cone. In this case, both the Bi and Se sublattices reveal the circulations of the spin around Γ or the Dresselhaus-like SOC feature about Y.

2.6 Conclusion

We have investigated the spin and spin-orbital textures and electronic structures of the topological surface states of two representative normal surfaces to the (111) surface, such as $(1\bar{1}0)$ and $(11\bar{2})$ surfaces, by using relaxed slabs constructed within DFT. In addition to inversion and time-reversal symmetries, the $(1\bar{1}0)$ surface has C_2 symmetry and the $(11\bar{2})$ surface has mirror symmetry. Effects of different surface symmetries and surface reconstruction were included in our DFT calculations of the slabs, in contrast to the effective model Hamiltonian approach based on linear and quadratic terms in momentum. This difference produces qualitative discrepancy between our findings and the results of the model Hamiltonian approach. We found that the spin and spin-orbital textures of the Dirac cones for the two normal surfaces entirely differ from each other and from those for the (111) surface. Interestingly, the $(1\bar{1}0)$ surface shows a combination of Rashba-type and Dresselhaus-type spin texture, and the spin directions do not align tangent to the tilted elliptic constant energy contours. For the $(11\bar{2})$ surface, the upper and lower Dirac cones near Γ shows the Dresselhaus-like and Rashba-like spin textures, respectively, whereas both Dirac cones near the Y point have the Dresselhaus-like spin texture.

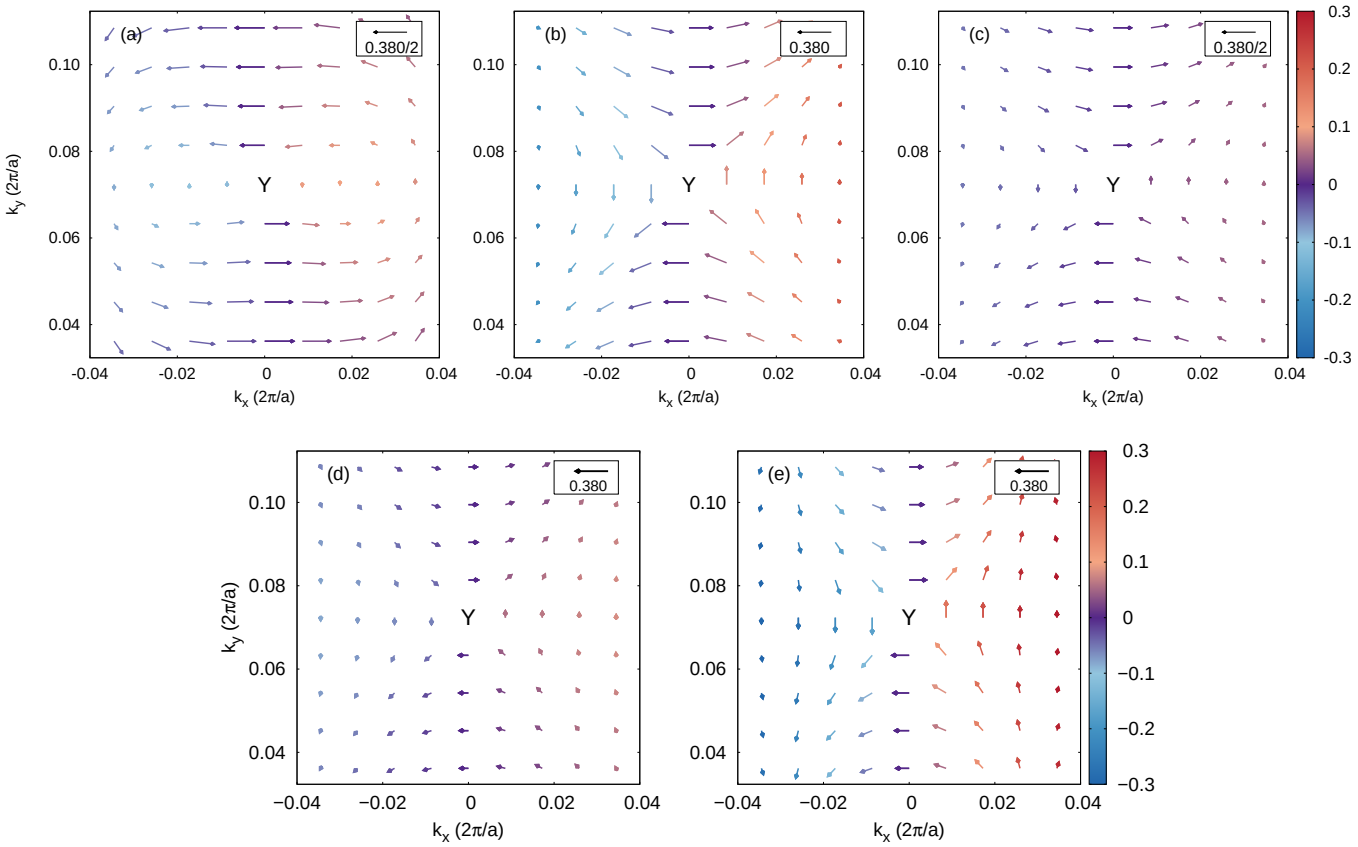

Figure 2.9: Spin-orbital texture near the Y point. Orbitally decomposed spin textures of (a-c) the lower Dirac cone of the surface state localized at the top surface near $E^{\mathrm{DP}}_{Y,\mathrm{low}}$ shown in Fig. 2.6(f): (a) the p_x orbital, (b) the p_y orbital, and (c) the p_z orbital. (d,e) Bi and Se sublattice decomposed spin textures of the lower Dirac cone near the Y point, respectively. The meanings of the in-plane and out-of-plane spin polarization scales are the same as those in Fig. 2.7. The scales of the arrows in (a) and (c) are different from those in (b), (d), and (e).

Chapter 3

Asymmetric charge transfer in Dirac semimetal films

This chapter was previously published. Reprinted with permission from John W. Villanova, Edwin Barnes, and Kyungwha Park, "Engineering and probing topological properties of Dirac semimetal films by asymmetric charge transfer," Nano Letters ***2017***, 17(2), *pp. 963-972 DOI:10.1021/acs.nanolett.6b04299. Copyright 2017 American Chemical Society [139].*

3.1 Introduction

Dirac and Weyl semimetals (DSMs and WSMs) are topological metals where bulk conduction and valence bands touch at an even number of momentum $\mathbf{k}$ points with Dirac dispersion at or near the Fermi level (E_F) [64, 65, 78, 98–103]. The band touching points are referred to as Weyl nodes and they are topologically protected. Depending on the positions of the Weyl nodes in the bulk, on particular surfaces the projections of the Weyl nodes of opposite chirality are connected by Fermi-arc states which can give rise to exotic transport phenomena. Weyl nodes cannot be destroyed unless Weyl nodes with opposite chirality are annihilated with each other at the same $\mathbf{k}$ point. There are two classes of DSMs [140]. The first class has an even number of Dirac nodes, each of which consists of a degenerate pair of Weyl nodes with opposite chirality. These Dirac nodes are induced by band inversion and stabilized by crystal symmetry. Due to the band inversion, DSMs in this class can have two-dimensional (2D) topological invariants. Na_3Bi and Cd_3As_2 are such DSMs, referred to as topological DSMs [99–103]. The second class of DSMs (for example, BiO_2 [98]) has one Dirac node at a time-reversal invariant momentum. The Dirac node in this class is neither associated with degenerate Weyl nodes nor 2D topological invariants. The degeneracy in the Dirac nodes in topological DSMs can be lifted when either inversion or time-reversal symmetry is broken, or both [141]. Recent experiments on Na_3Bi, Cd_3As_2, and the WSM TaAs family showed

interesting chiral magnetic effects as a result of the chiral anomaly [79, 142, 143] as well as unusual quantum oscillations in magneto-transport [76].

Topological materials are also predicted to induce new phenomena when they are in contact with conventional or non-topological materials [29, 30, 51, 144–146]. Such topological heterostructures have been widely explored in the context of topological insulators where novel features such as Majorana modes or topologically enhanced magnetism can arise [29, 30, 145, 146], but little is known about the properties of heterostructures that include DSMs or WSMs [144, 147]. Strong coupling between surface and bulk states in DSMs and WSMs allows interfaces to play a crucial role in hybrid structures, although the topological characteristics of DSMs and WSMs arise from the bulk. The interface may induce proximity effects or charge transfer and can change some orbitals near E_F or break some inherent symmetries. Therefore, it may be used as a tool to probe and control their topological bulk and surface properties. In order to investigate the coupling and interface effects, it is important to simulate hybrid structures including the interface at the atomistic level as well as to utilize low-energy effective models simultaneously. However, a majority of studies of DSMs and WSMs have, so far, focused on bulk properties, i.e. chiral magnetic and anomalous Hall effects [79, 142, 143, 148–150], and properties of the Fermi-arc surface states in the absence of the interface solely from an effective model approach with bulk parameters [68, 99, 103, 151–153]. Even without the interface it is extremely challenging to determine the positions of the Dirac node or Weyl node projections and to investigate properties of the projections and topological Fermi-arc states through direct simulations of finite-sized DSMs and WSMs. This is because the band gap closes very slowly with sample thickness [152] and because there is strong coupling between surface and bulk states. So far, these factors have stymied efforts to identify the positions of the node projections and Fermi arcs from direct simulations of DSM and WSM slabs [154].

Here we show that even for thin DSM films with a sizeable band gap, asymmetric charge transfer at the surface allows one to accurately identify the locations of the 3D Dirac node projections and to examine and modify properties of Fermi-arc states connecting them. While our approach works for any topological DSM, we demonstrate it explicitly by simulating Na_3Bi films with K or Na adsorption within density-functional theory (DFT) in conjunction with an effective model Hamiltonian. Our study functions as a first model to mimic the interface without other complications beyond the charge transfer and ensuing effects in DSM-based hybrid structures. We consider Na_3Bi $(1\bar{2}0)$ films with thicknesses in the range 5.5-21.8 nm with band gaps in the range 26-75 meV. Upon adsorption, charge transfer occurs close to the top surface only, so bulk properties such as the locations of the 3D Dirac nodes remain intact. Therefore the positions of the projections of the Dirac nodes do not change, whereas the topological top-surface states (TSS) are shifted downward in energy relative to the bottom-surface states (BSS) near E_F, due to the charge transfer. The structure of these robust surface states can thus be engineered by controlling the amount of charge transfer. This opens up many intriguing possibilities for controlling novel surface transport phenomena such as the so called "Weyl orbit" [75, 76]. In addition, the shift of the

TSS enables the identification of Dirac node projections despite a band gap. Since the node locations do not change, the downward shift of the TSS leads to easily identifiable gapless crossings of the states at the node projections. We find that the positions of the node projections are not sensitive to the amount of charge transfer, slab thickness, or the symmetry of a non-topological adlayer or substrate surface in the hybrid structure, as long as the slab is thick enough such that the asymmetric charge transfer does not occur throughout the slab. Furthermore, we show that there exist unique spin textures (distinct from a topological insulator) near the Dirac node projections and that the spin textures and the separation between the top- and bottom-surface Fermi arcs can be modified by varying the amount of charge transfer, independently of slab thickness or the symmetry of non-DSM layers in the heterostructure. Our findings can be experimentally observed in any topological DSM film by varying adsorbate type [155], adsorbate concentration, or substrate type, or by varying the voltage of a top or bottom gate without adsorbates or interfaces.

3.2 Structures and Calculation methods

We simulate Na_3Bi bulk and slabs by using the DFT code VASP [156, 157]. We use the generalized gradient approximation (GGA) [158] for the exchange-correlation functional and projector-augmented wave (PAW) pseudopotentials [11, 159]. Spin-orbit coupling (SOC) is included self-consistently within the DFT calculation. We consider bulk Na_3Bi with space group $P6_3/mmc$, as shown in Fig. 3.1a,b, with experimental lattice constants: $a = 5.448$ Åand $c = 9.655$ Å [99]. We use an energy cutoff of 250 eV for the bulk and slabs. For the bulk an $11 \times 11 \times 11$ k-point mesh is used. In addition to inversion symmetry, the bulk has four mirror symmetry planes (xy and yz planes, and two equivalent planes to the yz plane by C_3 symmetry about the c axis). See Fig. 3.1a,b. Note that our coordinates are rotated by $\pi/2$ counter-clockwise from the coordinates used in Refs. 99, 160. We simulate two surfaces, $(1\bar{2}0)$ and (100), whose top-down views are shown in Figs. 3.1c and 3.7a, respectively. Crystal structure figures were made using VESTA [132]. Normal vectors to the $(1\bar{2}0)$ and (100) surfaces correspond to the $[0\bar{1}0]$ and [210] directions in real space, which are shown in the Supporting Information Fig. 3.7b. For the slabs, a thick vacuum layer of 30-40 Å is included in the supercells. For the (100) surface, we consider a 5.50 nm thick slab with Na termination (36 atomic layers) and a 9.44 nm thick slab with Na and Bi termination (60 atomic layers). The surface area of each supercell in this case is $a \times c$, and we use a $9 \times 9 \times 1$ or $11 \times 7 \times 1$ k-point mesh. For the $(1\bar{2}0)$ surface, we consider four different slab thicknesses, such as 5.5, 10.9, 16.3, and 21.8 nm, which correspond to 21, 41, 61, and 81 atomic layers, respectively. The surface area of each supercell for this surface is $\sqrt{3}a \times c$, and we use a $5 \times 5 \times 1$ k-point mesh. We check that our calculated band structures do not change with dipole corrections. We confirm that relaxation of the experimental geometry/structure does not change the main results of our work.

3.3 Results

3.3.1 Electronic Structures of Bulk and Pristine Slabs

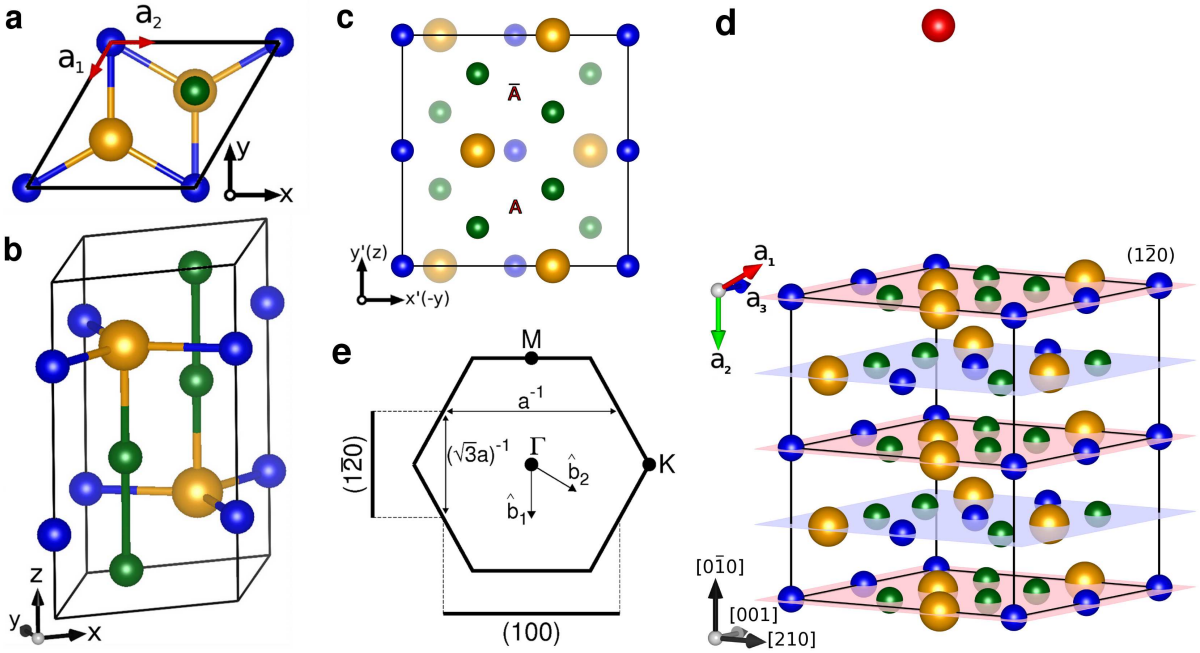

Figure 3.1: Bulk and slab crystal structures of Na_3Bi. (a) Top-down view of the bulk unit cell of Na_3Bi which crystallizes in the $P6_3/mmc$ hexagonal structure. This exhibits the unit cell of the (001) surface. (b) The bulk unit cell at a slight perspective angle. Bi atoms are large and orange. Na atoms are small and blue if in the same c-axis plane as Bi or small and green if not. The in-plane lattice vectors are shown in (a). (c) The unit cell of the $(1\bar{2}0)$ surface. The primed (unprimed) coordinates are the local (crystal) axes. Two inequivalent atomic layers are shown, the lower layer appearing faded. (d) A perspective view of the top five atomic layers of the slab geometry, with a single adatom (red) as in Cases I-III. (e) A top-down view of the bulk crystal first Brillouin zone (BZ) and the projections onto two surface BZs.

Our bulk band structure and 3D Dirac nodes $\mathbf{k}_D$ calculated by applying DFT with SOC are shown in Supporting Information Fig. 3.8b, and they agree well with those in the literature [99–101], where $\pm\mathbf{k}_D = (0, 0, \pm 0.13)\ 2\pi/c$. Although some recent studies suggest that Na_3Bi with space group $P\bar{3}c1$ (very similar to $P6_3/mmc$) may have a slightly lower energy than that with $P6_3/mmc$ [161, 162], we stick to the space group $P6_3/mmc$ in this work. The reasons are that most of the experimental works on Na_3Bi [99–101, 143, 163, 164] take the crystal structure to be $P6_3/mmc$ and that Na_3Bi with $P\bar{3}c1$ has the 3D Dirac nodes at the

same $\mathbf{k}_D$ points with the same Fermi-arc surface states [161]. The Fermi-arc surface states exist at surfaces which do not have the c axis as their normal vector. On a (001) surface the Weyl nodes with opposite chirality are projected onto the same $\mathbf{k}$ point, so Fermi-arcs are not guaranteed. Keeping this in mind, we consider two representative surfaces: $(1\bar{2}0)$ and (100) (Figs. 3.1c, e, and 3.7a). The $(1\bar{2}0)$ surface is neutral in charge since both Na and Bi atoms appear stoichiometrically. However, the (100) surface is polar and so dangling bond states are expected. We simulate (100) slabs with thicknesses of 5.50 and 9.44 nm with different types of surface terminations by using DFT with SOC. Our calculated band structures show several dangling bond states near E_F without surface state Dirac cones at $\overline{\Gamma}$. We show the DFT-calculated band structures of the 5.50-nm (100) slab terminated with two Na and one Bi atoms without and with H passivation in Supporting Information Fig. 3.9. Hence, hereafter, we consider the $(1\bar{2}0)$ surface only.

We simulate four pristine Na_3Bi $(1\bar{2}0)$ slabs with thicknesses of 5.5, 10.9, 16.3, and 21.8 nm by applying DFT with SOC. Figure 3.1d shows a schematic structure of the $(1\bar{2}0)$ slabs. The $(1\bar{2}0)$ surface has C_2 symmetry about the x (z') axis and mirror symmetry across the y (x') axis, as shown in Fig. 3.1c, where the unprimed (primed) coordinates are in terms of crystal (local) axes. The calculated band structure of the 10.9 nm slab is shown in Fig. 3.2a, while those of the three other thickness slabs are shown in Supporting Information Fig. 3.10. Each band has double degeneracy due to inversion and time-reversal symmetry except at time-reversal invariant k points (i.e., $\overline{\Gamma}$, $\overline{Z}$, and $\overline{Y}$) with fourfold degeneracy, where k is two-dimensional momentum. No dangling bond states are found near E_F. Along the $\overline{\Gamma} - \overline{Z}$ direction, there exists a bulk band gap. We show the density of states in Supporting Information Fig. 3.11a. Due to the finite sizes of the slabs or quantum confinement, the conduction and valence bands do not meet. The band gap of the $(1\bar{2}0)$ slab decreases very slowly with increasing slab thickness, which is shown in Supporting Information Fig. 3.11b. This result is in agreement with the literature [152]. Dirac dispersion is found near $\overline{\Gamma}$ in the vicinity of E_F. We identify surface states with a given color scale by computing electron density vs vertical coordinate z', or x, for each band at different k points. On the color scale, absolute values close to unity indicate states which are highly localized at the surface. The detail of the color scale is discussed in Supporting Information Note 1. The electron density vs z' plots for states A-E for the 10.9 nm slab are shown in Fig. 3.2b. State A has some contributions from the surface with a long non-zero tail deeply penetrating into the slab, while the states B and C near k_z^D show flat contributions from the whole slab, where $k_z^D = 0.13 \cdot 2\pi/c$. The horizontal line in Fig. 3.2a crosses the bands at k_z^D. The electron density of state D is clearly localized onto the top or bottom surface, with a decay length of about 2 nm, whereas state E has electron density localized mainly in the middle of the slab. We assign the states B and C as bulk states and state D as a surface state. State E is a quantum-well state. This identification is consistent with the fact that the bulk conduction and valence bands meet at the 3D Dirac nodes and that topological surface states are expected near $\overline{\Gamma}$ due to the large bulk band gap with band inversion at Γ [52, 99, 104, 160]. The finite band gap at Γ allows one to determine the Z_2 invariant despite the metallic nature of Na_3Bi. As shown later, existence of the surface Dirac cones near $\overline{\Gamma}$ for the adsorbed Na_3Bi

slabs reinforces the topological robustness of these 2D Dirac cones. Along the $\overline{\Gamma}-\overline{Z}$ direction, the surface states *gradually* become bulk states as k_z^D is approached from $\overline{\Gamma}$, but that is not the case along the $\overline{\Gamma}-\overline{Y}$ direction.

3.3.2 Electronic Structures of Slabs with Asymmetric Charge Transfer

To introduce the asymmetric charge transfer and to vary the transfer amount, we vary the vertical distance between the adatom and the Na_3Bi surface in a supercell of $1 \times 1 \times N$, where N is the slab thickness, without geometry relaxation. Here a 1×1 surface area in the supercell corresponds to the whole area shown in Fig. 3.1c. This method is computationally more effective in examining the effect of charge transfer amount or adsorbate concentration than a conventional method of increasing a supercell size such as $2\times2\times N$, $3\times3\times N$, or larger with a fixed number of adatoms whose positions are relaxed. Considering the thicknesses of the $(1\bar{2}0)$ slabs, it is computationally extremely challenging to use the conventional method for our study. It has been shown that our method gives rise to similar electronic structures to the conventional method for topological insulator films with adatoms or Bi bilayers [165–167]. Moreover, we check that the former method provides the similar band structures and features to the latter method for the adsorbed 5.5 nm $(1\bar{2}0)$ slab. More discussion is provided later.

We simulate four cases of the asymmetric charge transfer: Na atom at 15 Å, Na atom at 10 Å, K atom at 10 Å, and two K atoms at 6 Å above the 10.9 nm thick slab. These are henceforth referred to as Case I, II, III, and IV, respectively. The schematic structures of the four cases are shown in Figs. 3.1d and 3.12a. The cases of thinner and thicker adsorbed slabs will be addressed later. Even though a Na or K atom is adsorbed on site "A" indicated in Fig. 3.1c, we confirm that the calculated electronic structure does not depend on the adsorption site because of the large distance between the adatom and the surface. (For Case IV, one K atom is on the site "A" and the other on site "$\bar{\text{A}}$.") Thus, the adatom-enriched surface maintains the same symmetry as the pristine surface. Figures 3.2d-f and 3.12b shows our DFT-calculated band structures with top and bottom surface states identified as $+1$ and -1 for Cases I, II, III, and IV, respectively. The surface states are determined by using the same scheme as for the pristine slabs (see Supporting Information Note 1).

For Cases I-IV, the lifting of the double degeneracy is most apparent for the surface states (except at the time-reversal invariant k points, where the quadruple degeneracy is lifted to double degeneracy) because the charge transfer occurs mainly at the top surface rather than throughout the slab. The top surface states are shifted downward in energy relative to the bottom surface states near E_F, whereas the bottom surface states have approximately the same energy as those for the pristine slab relative to E_F (see E_Γ^{BSS} in Table 3.1). For Cases I-IV, at $\overline{\Gamma}$, the top-surface Dirac point is separated from the bottom-surface Dirac point by 23.6, 71.1, 156.3, and 196.6 meV, respectively (Figs. 3.2 d-f and 3.12b). This energy

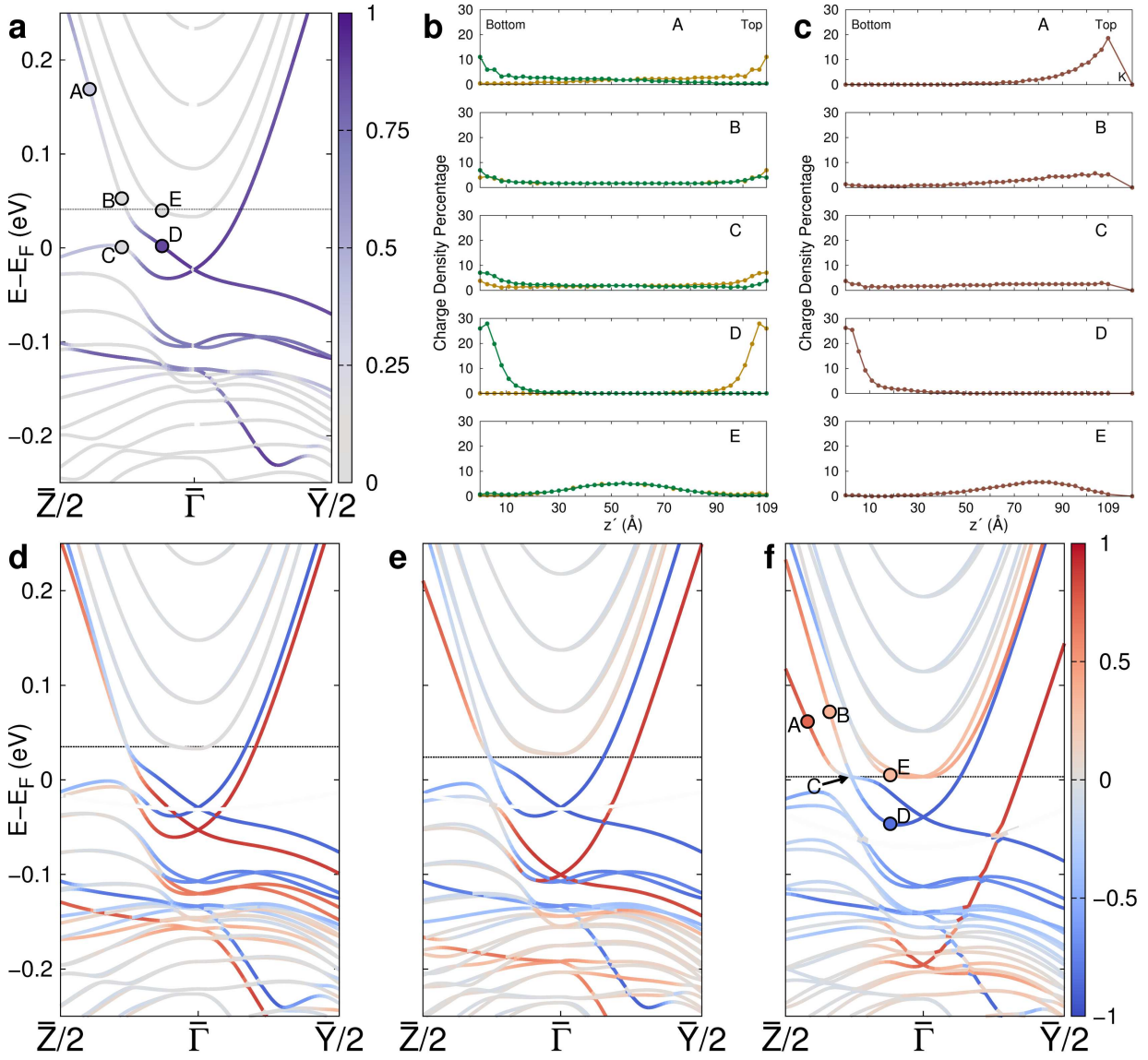

Figure 3.2: DFT-calculated electronic structures of Na_3Bi $(1\bar{2}0)$ slabs. (a) The surface band structure of the pristine slab. (b) Charge density vs coordinate z' profiles for states identified in (a). (c) Charge density vs coordinate z' profiles for states identified in (f). (d)-(f) The surface band structure for Case I, Case II, and Case III, respectively (Na- or K-impurity bands not shown). E_c is marked by a horizontal line in each case. On the color scales, absolute values close to unity indicate high surface localization of the states and are further discussed in the Supporting Information.

difference measures a potential difference between the top and bottom surfaces. A similar shift of the two surface Dirac cones was shown for topological insulators with adatoms [165]. We find that 0.027, 0.044, 0.073, and 0.116 e per unit cell area is transferred from the adatom to the slab for Cases I-IV, respectively. We discuss the calculation method in Supporting Information Note 2. The separation between the top- and bottom-surface Dirac points and the charge transfer amount for Case IV are comparable to those for the case of a $2 \times 2 \times 5.5$-nm adsorbed slab with a low K concentration. In the $2 \times 2 \times 5.5$ nm slab, only one K adatom is adsorbed and its position is optimized. For details, see Supporting Information Note 3. Once charge moves off the adatoms, the top surface states have lower energy because of the positive voltage created by the positively charged adatoms. The transferred charge fills the top-surface Dirac cone only, which explains the shift of the two surface Dirac cones near $\overline{\Gamma}$. The same effect can be reproduced by applying a gate voltage to the top surface without either adatoms or surface doping. In all four cases, the transferred charge penetrates into the slab up to about 3-4 nm, as shown in Supporting Information Fig. 3.13b. Interestingly, along the $\overline{\Gamma} - \overline{Z}$ direction, two outermost conduction bands meet at k_z^D with energy E_c as indicated by the dashed horizontal line. In all four cases the crossing of the bands at $\pm k_z^D$ is gapless, and the conduction and valence bands near $\pm k_z^D$ still have bulk characteristics . The electron density vs z' plots for Case III show surface character for state D and bulk characters for states B and C in Fig. 3.2c. The electron density of state E in Fig. 3.2c compared to that of state E in Fig. 3.2b clearly reveals small downward band bending at the top surface due to the charge transfer, similarly to the case of a topological insulator with adsorbates [165].

3.3.3 Constant Energy Contours and Spin Texture

For a better understanding of the band crossing points and the effect of the charge transfer, we examine constant energy contours (CECs) of the two outermost conduction bands near E_c and their spin textures at E_c for the pristine 10.9 nm slab. For the pristine slab we select the E_c value to be the energy of the lowest conduction band at k_z^D, indicated with a horizontal line in Fig. 3.2a. Figure 3.3a-c shows DFT-calculated CECs at $E_c - 10$ meV, E_c, and $E_c + 10$ meV, where colored bands are surface states. The doubly degenerate contours are symmetric about the local $k_{x'}$ (crystal k_y) and $k_{y'}$ (k_z) axes. The contours at E_c belonging to a single surface intersect the $k_{y'}$ axis at 90° degrees (without singularity) rather than obliquely (with singularity) due to the quantum confinement (Fig. 3.3b). Near the $k_{y'}$ axis the bands have bulk characteristics. Figure 3.4a illustrates DFT-calculated spin textures of the bands at E_c. The spin polarization of the bands is tangential to the CEC. Along the $k_{y'}$ ($k_{x'}$) axis, the spin polarization is constrained to be normal to the $k_{y'}$ ($k_{x'}$) axis because of the glide mirror (horizontal mirror) plane $k_{y'}$-$k_{z'}$ ($k_{x'}$-$k_{z'}$). The top-surface (bottom-surface) states show clockwise (counter-clockwise) rotation of the spin, which will be re-interpreted in comparison to the spin textures for the adsorbed slabs later.

Next we investigate CECs of the two conduction bands for Cases I-IV near E_c. Figure 3.3d-l

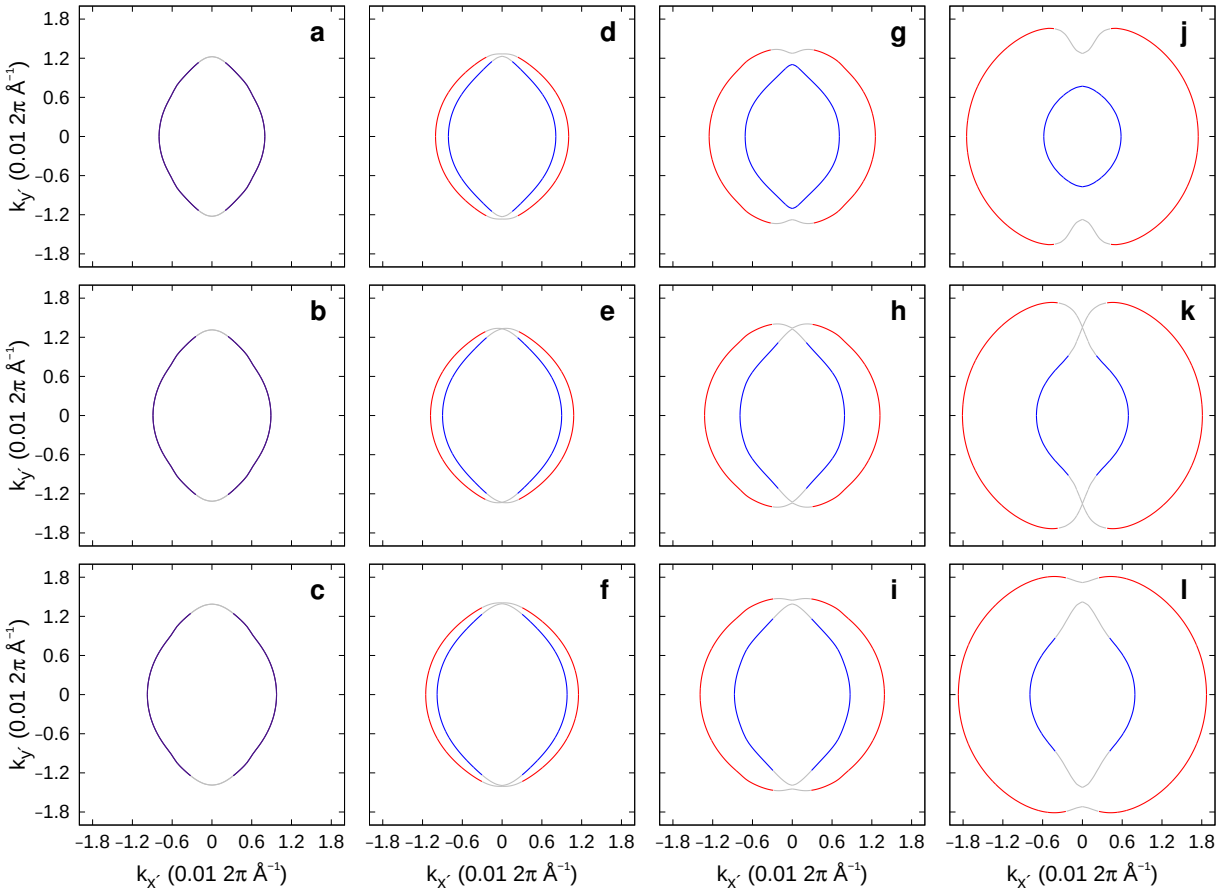

Figure 3.3: Constant energy contours (CECs) of four systems at three different energies. Top (bottom) surface states are identified in red (blue). The doubly degenerate surface states in the pristine case are shown in purple. The top row is at $E = E_c - 10$ meV. The middle row is at $E = E_c$. The bottom row is at $E = E_c + 10$ meV. The first column (a)-(c) is for the pristine 10.9 nm slab. The second column (d)-(f) is for Case I. The third column (g)-(i) is for Case II. The fourth column (j)-(l) is for Case III. In all of the adsorbate cases, the CECs only touch each other at $E = E_c$.

shows the CECs for Cases I-III at $E_c - 10$ meV, E_c, and $E_c + 10$ meV with band characteristics (i.e., surface or bulk states). The CECs for Case IV are not shown since they have qualitatively similar features to those for Case III. In all four cases, the contours are still symmetric about the $k_{x'}$ and $k_{y'}$ axes, and they cross at $(k_{x'}, k_{y'})=(0, \pm k_z^D)$ with *singularity* only for energy E_c (see Table 3.1). The contours for E_c connecting the $(0, \pm k_z^D)$ points have bulk character near the crossing points and gradually change to top or bottom surface-state character away from the points (Fig. 3.3e,h,k). These features of the E_c contours coincide with those of the Fermi arcs appearing on a surface of a topological DSM when the $(0, \pm k_z^D)$ points are projections of the Dirac nodes. Our analysis (based on an effective model) that will be discussed later ensures that these contours are indeed Fermi arcs. Away from E_c the closed contours do not cross each other. Although near the crossing points, $\pm k_z^D$, the surface state character disappears for both contours at a given energy, the contours are referred to as top- and bottom-surface contours for convenience in explaining their features and spin textures. In Cases I-IV, the bottom-surface contour always appears inside the top-surface contour. For the small charge transfer (Case I), the overall contour shapes do not change much with energy except for the region very close to the crossing points (Fig. 3.3d-f). As the amount of charge transfer increases, the top-surface contour at E_c expands along both the $k_{x'}$ and $k_{y'}$ directions with a slightly pinched circular shape, whereas the bottom-surface contour shrinks mostly along the $k_{x'}$ axis while keeping its oval or almond shape. Compare Fig. 3.3e with Fig. 3.3h,k. For large charge transfer (Cases III and IV), the overall shapes of the CECs now significantly change at energies away from E_c. Compare Fig. 3.3k with Fig. 3.3j,l. Below E_c the bottom-surface closed contour has pure surface-state character without singularity for all k values (Cases II-IV).

We also examine spin textures at the E_c contours for Cases I-IV. Figure 3.4b,c,e shows DFT-calculated spin textures of the states at the E_c contours for Cases I-III, respectively. For all four cases the spin polarization along the $k_{y'}$ axis is constrained to be normal to the mirror $k_{y'}$-$k_{z'}$ plane, but at the crossing points, $\pm k_z^D$, the spin is ill-defined. For small charge transfer (Case I), the spin polarization along the bottom-surface contour rotates counterclockwise and is tangential to the contour except for very close to the $k_{y'}$ axis. The spin orientations along the top-surface contour are opposite to those along the bottom-surface contour. Overall features of the spin textures in this case are similar to those for the pristine slab. In Case II, interestingly, the spin texture along the top-surface contour is found to qualitatively differ from that for Case I and the pristine slab, as highlighted in the yellow shaded areas in Fig. 3.4c, although the spin texture along the bottom-surface contour is similar to that for Case I. Near the crossing points, the spin polarization along the top-surface contour is substantially reduced and its orientation deviates considerably from the tangent to the contour. Approaching k_z^D, the spin polarization in the $k_{x'} > 0$ plane ($k_y < 0$ plane) becomes almost perpendicular to the contour and then it turns toward the other direction such that it smoothly interpolates into the spin polarization of the bottom-surface contour in the $k_{x'} < 0$ plane. The same trend is found in Case III with more pronounced features and it appears at larger $|k_{x'}|$ and $|k_{y'}|$ values due to the larger charge transfer. The same trend as Case III is also observed for the spin textures for Case IV (not shown). The

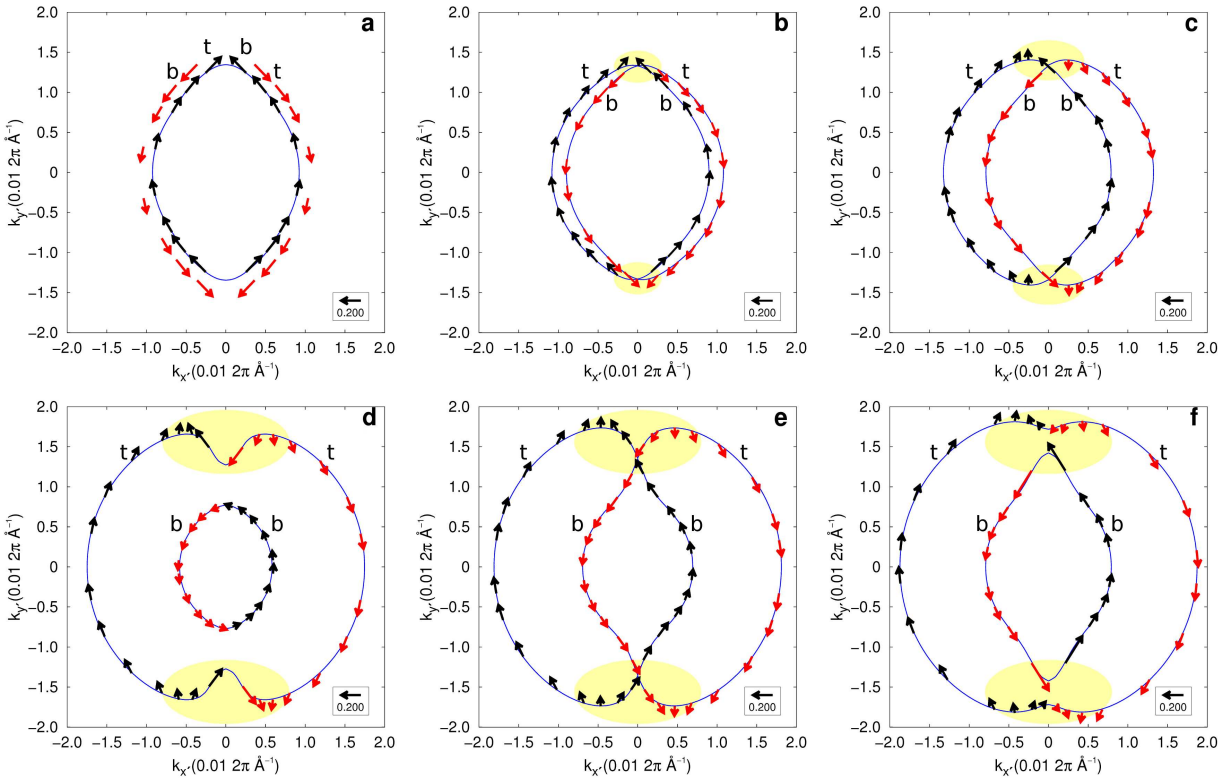

Figure 3.4: Spin textures along constant energy contours. (a) For the pristine slab at $E = E_c$. The degenerate bands have exactly opposite spin, and the spin texture for the down-sector is shown offset from the CEC for clarity. (b) For Case I at $E = E_c$. (c) For Case II at $E = E_c$. (d) For Case III at $E = E_c - 10$ meV. (e) For Case III at $E = E_c$. (f) For Case III at $E = E_c + 10$ meV. In every panel, the spin is colored according to which spin-sector it belongs to, up (down) -sector spin is shown in black (red). The top (t) or bottom (b) surface character is also marked. In the adsorbate cases, the region including k_z^D and $(\pm k_{x'}^0, \pm k_{y'}^0)$ is highlighted in yellow.

$(\pm k^0_{x'},\pm k^0_{y'})$ points at which the spin polarization of the states at the top-surface contour is almost normal to the contour for Cases II-IV are listed in Table 3.1. This unique spin texture of the top-surface contour is distinct from that associated with the surface states of a topological insulator. The interesting spin texture still appears at slightly below and above E_c, as shown in Fig. 3.4d,f. Figure 3.5 schematically combines the spin texture and surface character of the CECs seen in Figs. 3.3k and 3.4e with emphasis on those segments of the CECs belonging to different spin sectors, as we describe next.

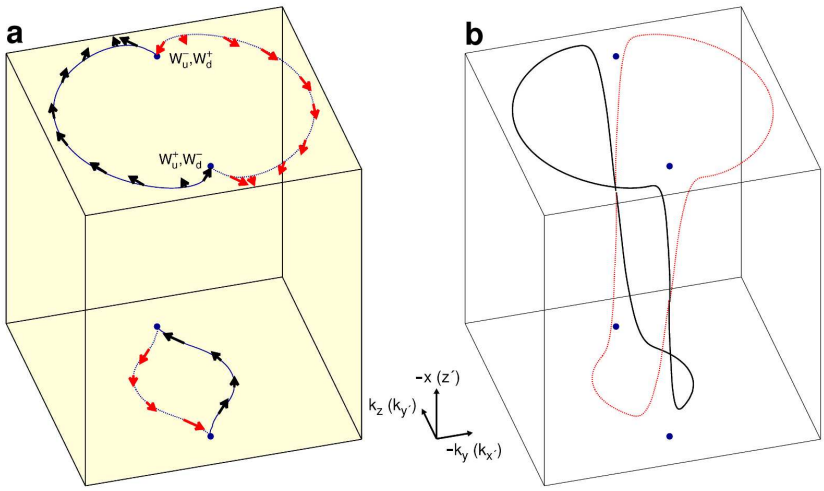

Figure 3.5: Schematic diagrams of the Fermi arcs in DSM thin films with asymmetric charge transfer. (a) Fermi arcs connect the projections of the Dirac nodes on the surface, and the up and down spin sectors are colored in black and red, respectively. The crystal (local) coordinates are shown. (b) A representation of how the surface character of the Fermi arcs changes on approach to the Dirac nodes, developing significant bulk character near the Dirac nodes. At the Dirac node, schematically at the center of the slab, the charge density is smeared through the entire slab as shown in panel C of Fig. 3.2c.

3.3.4 Analysis Based on DFT Calculations and Model

Now we analyze our DFT-calculated results by using an effective model. With inversion symmetry, the electronic structure of bulk Na_3Bi near Γ can be described by an effective low-energy 4×4 model Hamiltonian [99] (see the Supporting Information Discussion 1). The same Hamiltonian with different parameter values can be used for the electronic structure of bulk Cd_3As_2 [103]. The effective model up to second order in $\mathbf{k}$ indicates that Weyl fermions associated with one pair of Weyl nodes, $W_u^{\pm}$, are related to Weyl fermions at another pair of Weyl nodes, $W_d^{\mp}$, by interchanging k_y with $-k_y$ [160]. Thus, the Fermi-arc surface states connecting projections of $W_u^{\pm}$ are also related to those connecting projections of $W_d^{\mp}$ by

$k_y \leftrightarrow -k_y$ or $k_{x'} \leftrightarrow -k_{x'}$ (Fig. 3.6a). The two pairs of Weyl nodes ($W_u^{\pm}$, $W_d^{\mp}$) are referred to as *up*- and *down*-sector following the (crystal) z component of the spin polarization of the Fermi-arc states [160]. The calculation based on the model reveals that for the up-sector WSM, the Fermi-arc state from the top surface appears in the $k_{x'} < 0$ ($k_y > 0$) plane, while that from the bottom surface appears in the $k_{x'} > 0$ ($k_y < 0$) plane. For the down-sector WSM, the Fermi-arc states from the top and bottom surfaces are formed on half-planes opposite to those for the up-sector (Fig. 3.6a). These spin textures qualitatively agree with our DFT-calculated results for the pristine slab (Fig. 3.4a vs 3.6a). The model-calculated CECs at E_c are compared to the DFT-calculated CECs in Fig. 3.6c. The $|k_z^D|$ value from the model, $\sqrt{M_0/M_1}$ ($= 0.01438 \cdot 2\pi$ Å$^{-1} = 0.14 \cdot 2\pi/c$), is slightly greater than that from our DFT band structure and the literature [99]. See Supporting Information Discussion 1 for details. The Fermi-arc states from the model meet the x' axis at a much greater $k_{x'}$ value than that from the DFT result (Fig. 3.6c). This discrepancy is not due to the small slab thickness but arises from differences in the bulk band structure obtained from the model and DFT calculations (of ours and the literature [99]), as shown in Fig. 3.6e. The parameters used in the effective model give rise to dispersion in agreement with the DFT-calculated bands along the z axis with a slightly larger value of $|k_z^D|$ than $0.13 \cdot 2\pi/c$, whereas the dispersion along the y axis is greatly off from the DFT-calculated bands except for in the vicinity of Γ.

Now with the asymmetric charge transfer at the *surface*, the symmetry in the bulk does not change and so the locations of the 3D Dirac-node projections are not affected, i.e. $\pm k_D$=(0, $\pm 0.13 \cdot 2\pi/c$). Thus, the Fermi-arc states from the top and bottom surfaces must connect the projections of the Dirac nodes. This is because of the coexistence of the degenerate Weyl nodes of opposite chirality at the Dirac nodes; owing to the up/down sector symmetry, the degenerate Weyl nodes (W_u^- and W_d^+ in Fig. 3.6a) are not annihilated at each Dirac node but instead are superimposed on each other. The Weyl node with which a given Weyl node would annihilate is actually situated across the Brillouin zone at the opposite Dirac node. Our DFT calculations show such connections between the Dirac node projections. Compare Fig. 3.3e,h,k and Fig. 3.4b,c,e with Fig. 3.6b. These connections explain the existence of the gapless band crossings at $\pm k_z^D$ and why the bands shown in Fig. 3.3e,h,k carry bulk characteristics near the Dirac node projections (see Fig. 3.5). The shapes of the top- and bottom-surface contours can be explained by introducing a surface potential V to the top-surface states in the model since the charge transfer occurs mainly at the top surface. See Supporting Information Discussion 1 for details. In the semi-infinite slab limit, with $V =$ 0.12 eV, we calculate the top- and bottom-surface states at E_F for the up- and down-sector within the model, as shown in Fig. 3.6d. The value of V qualitatively corresponds to Case III. The model-calculated CECs of the surface states show that the down-sector surface states are shifted toward the positive $k_{x'}$ direction, while the up-sector surface states shift toward the opposite direction, with their crossing points near $\pm k_z^D$. This trend agrees with our DFT-calculated CECs of the Fermi-arc states. With $V = 0.12$ eV, the k values of the crossing points and the amount of the shift of the Fermi surface states obtained from the model [represented by $(k_{x'}^0, k_{y'}^0)$] are in reasonable agreement with those of our DFT

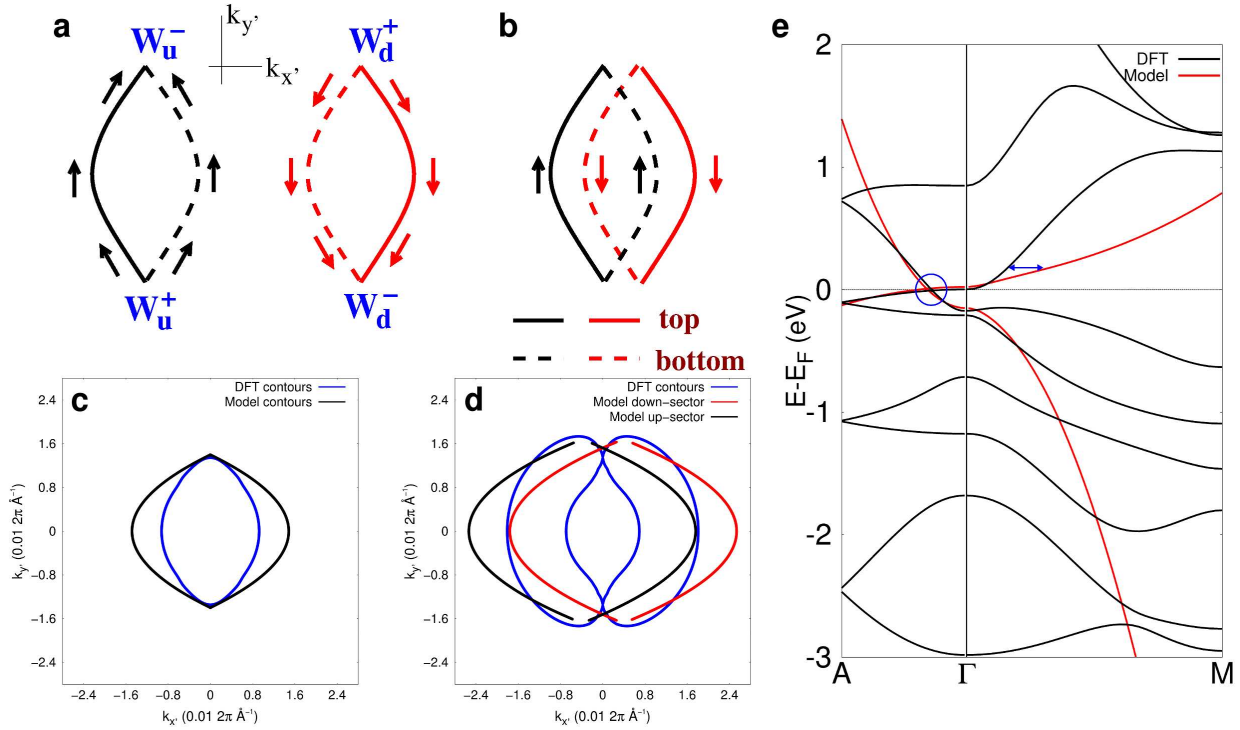

Figure 3.6: Comparison of the DFT result with the effective model. (a) Schematic diagram of the Fermi-arc surface states connecting Weyl node projections from each spin-sector for the up-sector (black) and down-sector (red). The top (bottom) surface character is shown by the solid (dashed) curves. In the pristine slab case, these contours lie on top of each other, and so the schematic in this panel is not meant to indicate absolute locations of the Weyl node projections in the surface BZ. (b) Schematic diagram of the surface states in the adsorbate cases, with spin and surface character denoted as in (a). (c) CECs from the model for the pristine semi-infinite slab and from the DFT calculation for the pristine 10.9 nm slab. (d) CECs from the model with $V = 0.12$ eV and from the DFT calculation for Case III. (e) DFT- and model-calculated bulk band structure. The model locates the bulk Dirac node slightly farther from Γ than our DFT calculation does, circled in blue. The blue arrow draws attention to the significant deviation of the bands of the model from our DFT calculation along the $\Gamma - \mathrm{M}$ direction, which is responsible for the substantial difference between the DFT and model CECs along the local x' axis, as seen in (c) and (d).

calculations (Fig. 3.6d). The spin textures along the top- and bottom-surface contours from our DFT calculations also qualitatively agree with those from the model. The gapless band crossings at $\pm k_z^D$ can be also justified by the crossings of different spin sectors, i.e. up- and down-sector. Interestingly, although the spin textures near $(\pm k_{x'}^0, \pm k_{y'}^0)$ points (the yellow shaded areas in Fig. 3.4c,e) follow as if they are the Weyl node projections (Fig. 3.6b), these k points are not the true projections of the 3D Weyl nodes. Several reasons to corroborate this are provided. In Supporting Information Discussion 2 and Note 3, we discuss the case where asymmetric charge transfer occurs throughout the entire slab such that it breaks C_3 and inversion symmetries at the bulk level, based on the effective model as well as DFT-calculated band structures. The main features in this case of broken bulk symmetry do not agree with those of Cases I-IV. For example, we find an increase of $|k_{y'}^0|$ as charge transfer increases (Table 3.1), whereas the case in the Supporting Information predicts a decrease of $|k_{y'}^0|$. Moreover, when the asymmetric charge transfer influences the entire slab, the gapless band crossings occur far away from the original 3D Dirac-node projections $\mathbf{k}^D$ (Supporting Information Note 3). As clearly shown in Figs. 3.3e, h, k, and 3.14, the electron density near and at $(\pm k_{x'}^0, \pm k_{y'}^0)$ is mostly localized at the surface rather than bulk. If the $(\pm k_{x'}^0, \pm k_{y'}^0)$ points were separated (non-degenerate) Weyl node projections, the electron density profile must reveal bulk characteristics near those k points rather than near the gapless band crossing points. Therefore, our result suggests that the spin textures alone are not sufficient to identify the locations of the Dirac-node projections, in contrast to Ref. 154, and that apparent projections of the 3D Weyl nodes such as $(\pm k_{x'}^0, \pm k_{y'}^0)$ at the surface are *not* necessarily related to the 3D Dirac or Weyl nodes in the bulk.

3.4 Discussion

Regarding the DFT-calculated features, six caveats need to be addressed. First, simple charge transfer to the slab is not enough to observe the main outcomes of this work. The charge transfer must be asymmetric and only at the surface. We consider the case that one Na atom is adsorbed on both the top and bottom surfaces of the 10.9 nm thick slab while keeping the distance between the adatom and the surface at 10 Å. The charge transfer amount, 0.089 e per unit cell area, is comparable to that for Case III. We provide the DFT-calculated band structure of this slab in Supporting Information Fig. 3.15. The calculated band structure shows that the bulk band gap is 27.3 meV and that there are no band crossings at $\pm k_z^D$ or any other k points near the Fermi level. Second, we find that the gapless band crossings at the 3D Dirac node projections appear independently of the amount of charge transfer and slab thickness, as long as the slab is thick enough such that the asymmetric charge transfer occurs only at the surface rather than throughout the entire slab. We investigate the electronic structures of adsorbed slabs thinner and thicker than the 10.9 nm slab studied earlier in the text: slabs with thicknesses of 2.7, 5.5, and 16.3 nm. Their band structures are provided in Supporting Information Fig. 3.16. The band structure of the K-adsorbed 2.7-nm slab

(where the K atom is 10 Å above the surface) shows gapless band crossings at $\pm 0.12 \cdot 2\pi/c$, which does not coincide with the Dirac node projections. However, for the 5.5 nm and 16.3 nm thick slabs with adatoms, the gapless band crossings occur at $\pm k_z^D$. Third, the aforementioned CECs and spin textures depend only on the amount of charge transfer, independent of slab thickness and adatom type, as long as the slab is somewhat thicker than the penetration depth of the charge transfer. We show the CECs and the spin textures at E_c for the adsorbed 5.5 nm slab in Supporting Information Fig. 3.17. These figures can be compared with Figs. 3.3k and 3.4e. Considering the symmetry of Cd_3As_2 (with space group $I4_1acd$ [168]), similar spin textures to our work are expected for a (112) surface of Cd_3As_2 [169]. Fourth, due to robustness of the Dirac or Weyl nodes against *surface* perturbations, the symmetry of a non-topological material (substrate or overlayer) at the interface with a DSM or WSM is not important in hybrid structures in order to experimentally observe our DFT-calculated properties of the Fermi-arc states and bulk states. What is important is the amount of asymmetric charge transfer. Fifth, the gapless band crossings would not occur in thin films for the surface where the Weyl nodes with opposite chirality for a given sector are projected onto the same **k** points, such as the (001) surface, even with the asymmetric charge transfer. Sixth, the features we found in this work cannot be observed in the second class of DSMs such as BiO_2 [98, 140]. It is crucial to have topological surface states which are ensured by the band inversion in topological DSMs, in order to observe the gapless band crossings. However, topological surface states do not exist in the second class of DSMs.

3.5 Conclusion

In summary, we investigated probing and engineering topological bulk and surface properties of DSM thin films with a band gap by the asymmetric charge transfer which may occur at the interfaces of heterostructures involving DSMs or WSMs. We simulated K- or Na-adsorbed Na_3Bi $(1\bar{2}0)$ films where a small amount of charge is transferred at the top surface only and the charge transfer amount is varied, by using DFT including SOC rather than using an effective model or tight-binding model with bulk parameter values. We found that the asymmetric charge transfer induces the gapless band crossings exactly at the 3D Dirac node projections for thin slabs despite the band gap because the topological top- and bottom-surface states separated by the charge transfer are pinned by the projections of the topologically robust 3D Dirac nodes. We also showed that the CECs and spin textures at the band crossing energy can be modified by varying the amount of charge transfer. The main features we discussed are independent of slab thickness when the asymmetric charge transfer occurs only in close proximity to the surface. Although we considered a specific example of Na_3Bi slabs, our findings can be applied to other topological DSMs.

Table 3.1: DFT-calculated parameter values for the pristine and adsorbed $(1\bar{2}0)$ slabs: the energy of the 3D Dirac node E_c, the amount of charge transfer per unit cell area (u.c.a), $\Delta\rho$, the energy of the TSS and BSS at Γ (E_Γ^{TSS} and E_Γ^{BSS}), μ=$|E_\Gamma^{TSS}-E_\Gamma^{BSS}|$, the position of the projections of the 3D Dirac node along the k_z axis (k_z^D), the intersections of the surface states with the $k_{x'}$ axis ($k_{x',TSS}$ and $k_{x',BSS}$), and the coordinates ($k^0_{x'}$, $k^0_{y'}$) of the shift of the TSS. All energies are relative to E_F and all momenta appear in units of 2π Å^{-1}.

	Pristine	Case I	Case II	Case III	Case IV
E_c (meV)	41	35	24	3.3	2.0
$\Delta\rho$ (e/u.c.a.)	0	0.027	0.044	0.073	0.116
E_Γ^{TSS} (eV)	-0.0232	-0.0529	-0.1004	-0.1957	-0.2242
E_Γ^{BSS} (eV)	-0.0232	-0.0293	-0.0293	-0.0394	-0.0277
μ (eV)	0	0.0236	0.0711	0.1563	0.1965
k_z^D	0.01346	0.01334	0.01337	0.01353	0.01377
$k_{x',TSS}$	0.00889	0.01080	0.01323	0.01810	0.02020
$k_{x',BSS}$	0.00889	0.00898	0.00799	0.00709	0.00541
$k^0_{y'}$	N/A	0.01337	0.01405	0.01735	0.01916
$k^0_{x'}$	N/A	0.00057	0.00218	0.00458	0.00483

3.6 Supporting Information

This Supporting Information contains (1) a top-down view of (100) surface and real-space (100) and $(1\bar{2}0)$ surface terminations, (2) DFT-calculated bulk band structure, (3) DFT-calculated band structures of a (100) slab, (4) dependence on slab thickness of the band structure, (5) calculated density of states of the slabs, (6) a perspective view of Case IV and the band structure, (7) quantification of charge transfer to a slab in the adsorbate cases, (8) electron density vs z' plot at $(\pm k^0_{x'}, \pm k^0_{y'})$ points, (9) band structure in the case of symmetric charge transfer, (10) slab thickness dependence in the adsorbate case, (11) constant energy contours for the adsorbed 5.50-nm slab, (12) a note on identifying surface states, (13) a note on the quantification of charge transfer, (14) a note on the cases of optimized adsorbates, (15) a discussion of the calculations with the model Hamiltonian, and (16) a short discussion in the case of broken bulk symmetry.

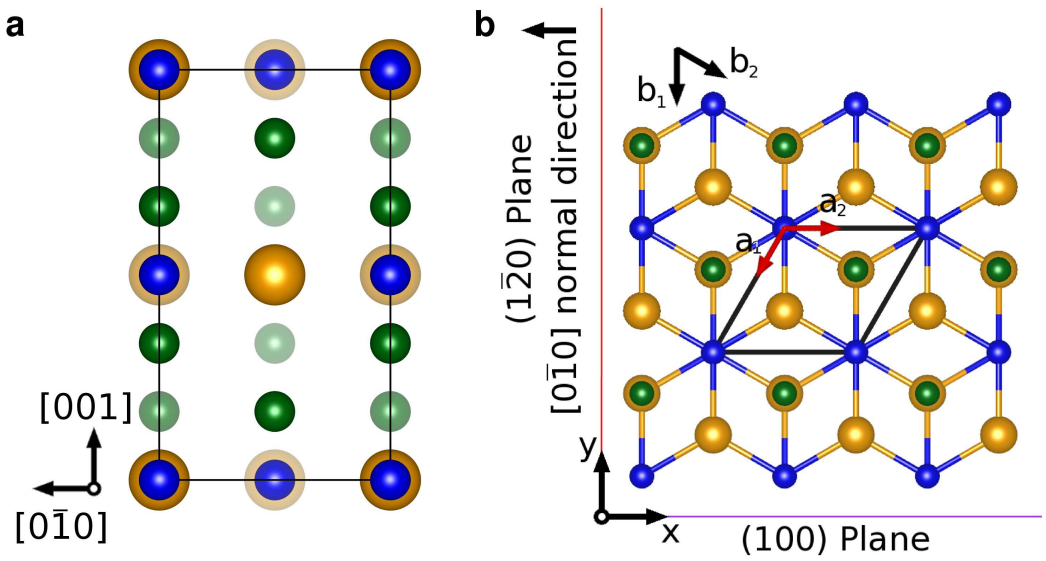

Figure 3.7: Side-views of the slab unit cell. (a) The side-view of the slab unit cell exhibiting the (100) surface. (b) Two representative Na_3Bi surfaces possessing the Fermi-arc surface states: (1$\bar{2}$0) and (100) planes.

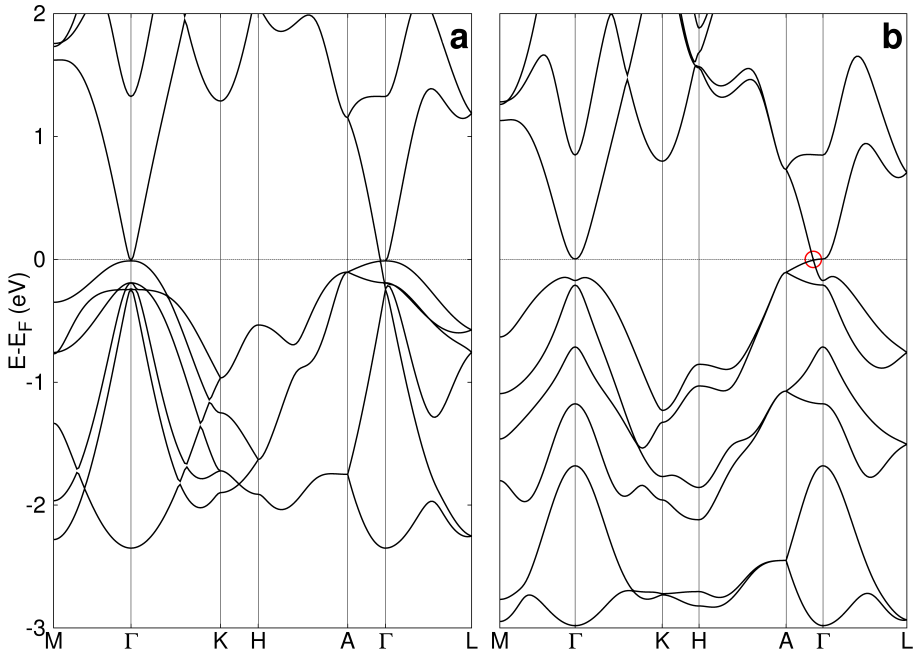

Figure 3.8: Electronic structure of bulk Na_3Bi with space group $P6_3/mmc$ (a) without and (b) with spin-orbit coupling. In (b) the Dirac node is emphasized.

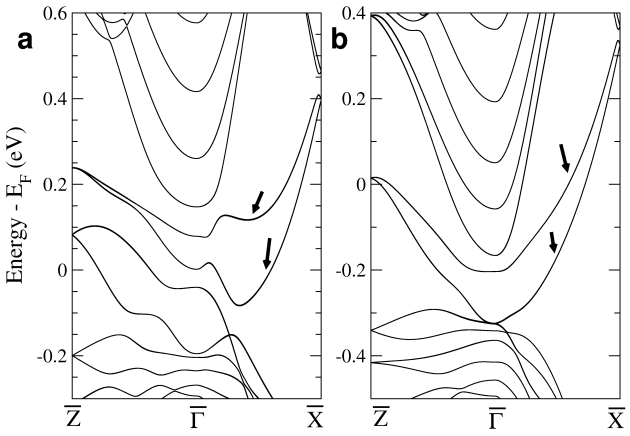

Figure 3.9: Electronic structure of the (100) slab. A 5.5 nm thick Na_3Bi (100) slab terminated with two Na and one Bi atoms (a) without and (b) with H passivation. Arrows indicate dangling bond states. The horizontal axis is in units of $2\pi/c$ for the $\overline{\Gamma} - \overline{Z}$ direction, while it is in units of $2\pi/a$ for the $\overline{\Gamma} - \overline{X}$ direction. All bands have double degeneracy due to time-reversal and inversion symmetries. Note that any (100) surface termination type is not stoichiometric. Our calculations differ from the literature [99, 152] in that we simulate finite-sized slabs by using DFT rather than obtaining the surface states in the semi-infinite slab limit with Wannier functions from bulk DFT calculations. In the latter approach, any realistic effects of surface termination types and dangling bond states are neglected.

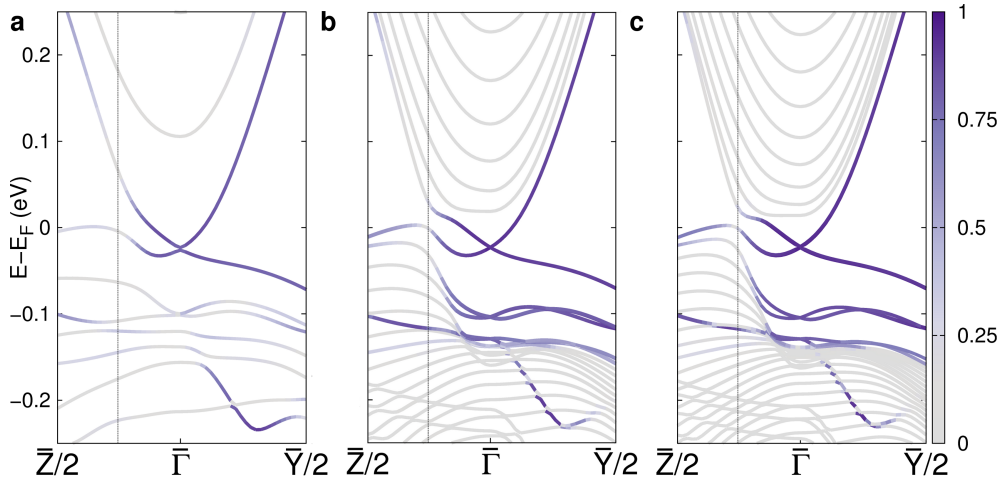

Figure 3.10: Electronic structure of pristine $(1\bar{2}0)$ slabs of various thickness. (a)-(c) with thicknesses 5.5, 16.3, and 21.8 nm, respectively. On the color scale, absolute values close to unity indicate high surface localization of the states, according to Supporting Note 1. There are no dangling bond states and topological surface-state Dirac cones are clearly visible near $\overline{\Gamma}$.

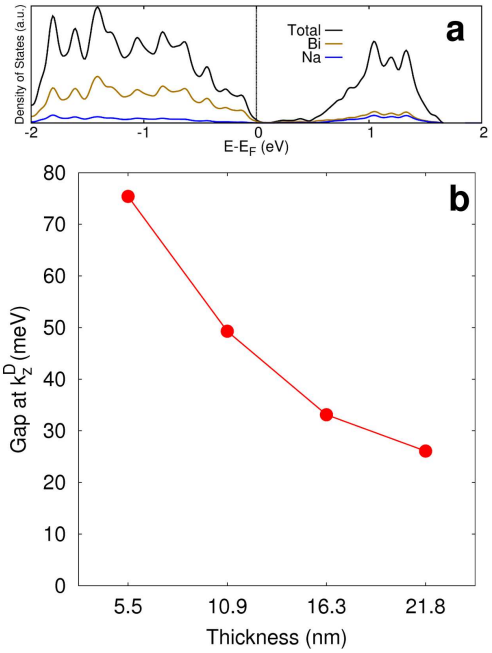

Figure 3.11: (a) Density of states for the 10.9 nm thick $(1\bar{2}0)$ slab. (b) DFT-calculated bulk band gap computed at k_z^D vs slab thickness for the $(1\bar{2}0)$ surface.

3.6.1 Supporting Note 1: Identification of Surface and Bulk States

The surface states are identified by calculating electron density as a function of the vertical coordinate (local z' coordinate). We calculate the following quantity:

$$D = \frac{\sum_j^N \rho_j z'_j}{\sum_j^N \rho_j} \frac{1}{\frac{L_{z'}}{2}},$$

where ρ_j is the electron density at the atomic layer j with its vertical component z'_j, N is the total number of atomic layers per supercell, and $L_{z'}$ is slab thickness. We set $z'_j = 0$ at the center of the slab. Here $D \in [-1, 1]$ and $D = +1$ $(D = -1)$ indicates a surface state which is perfectly localized at the top (bottom) surface. For the adsorbed slabs (Case I-IV in the main text and Fig. 3.16), the definition of D is slightly modified in order to exclude the adatom layer. The color scales in Fig. 3.2d-f in the main text and Figs. 3.10 and 3.16 indicate the values of D. For the purpose of identifying surface states in the DFT-calculated CECs, the electron density is considered to be localized at the top (bottom) surface when $D \geq 0.5$ $(D \leq 0.5)$.

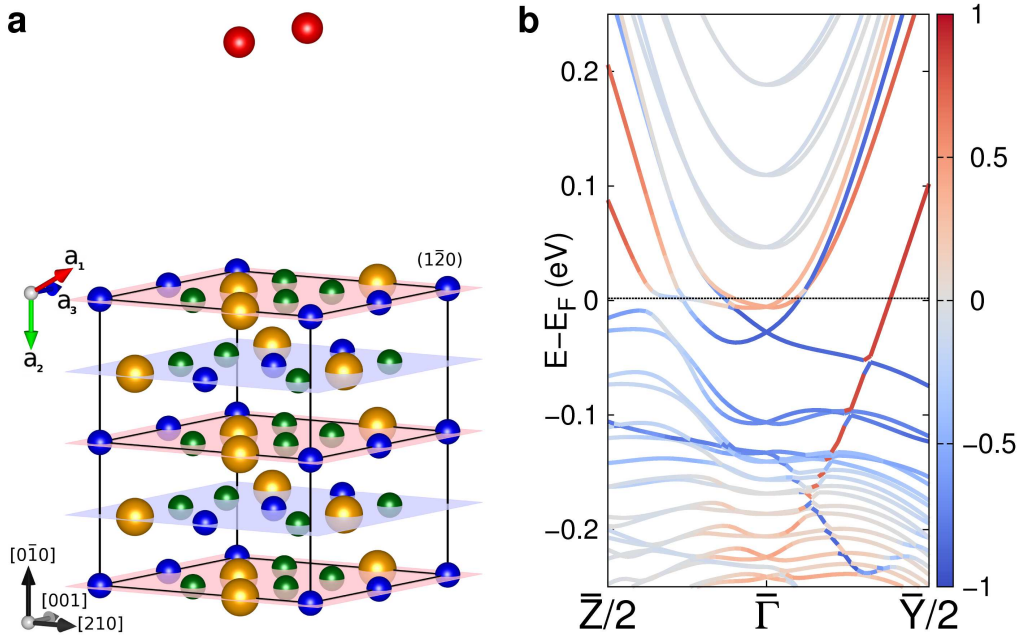

Figure 3.12: The slab geometry with two adatoms. (a) A perspective view from the top, with two adatoms (red) as in Case IV. (b) Band structure corresponding to Case IV in the text.

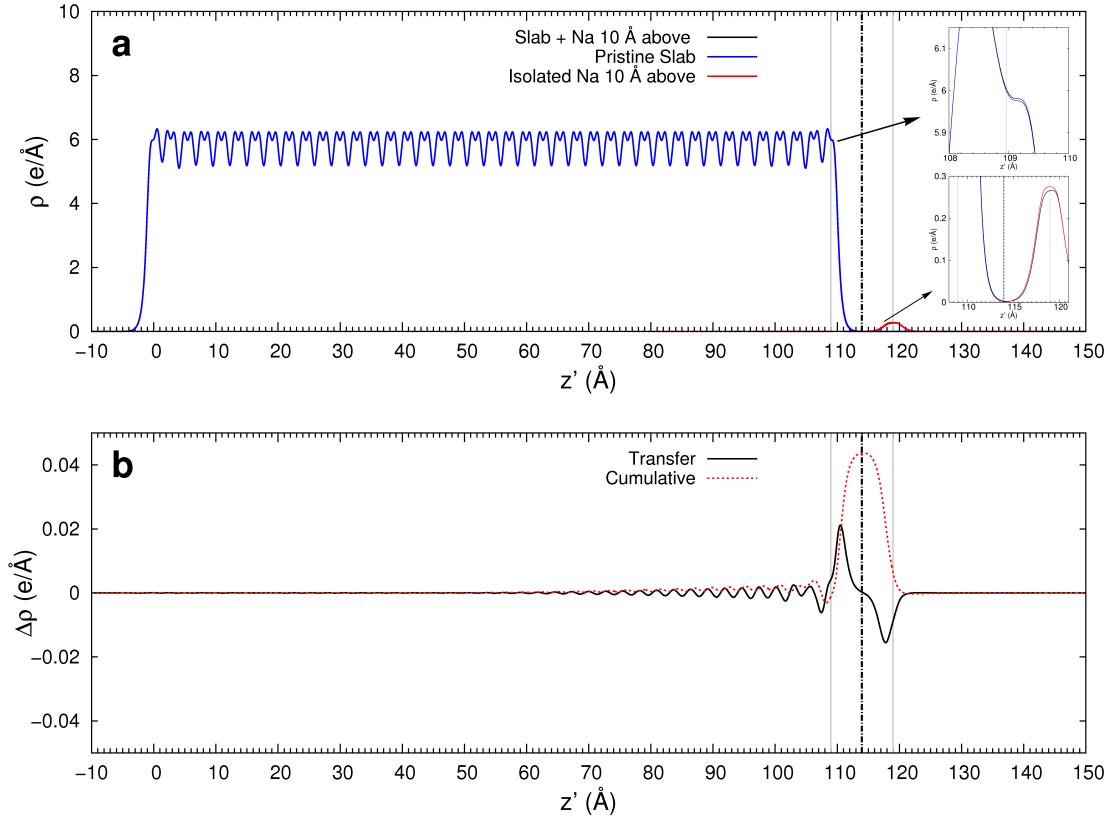

Figure 3.13: (a) Layer-projected electron densities of the 10.9 nm thick Na_3Bi $(1\bar{2}0)$ slab with one Na atom 10 Å above, the isolated Na_3Bi slab, and the isolated Na atom, as a function of the vertical distance z' from the bottom surface. Two insets are zoom-in figures near the surface to clarify the small differences. (b) Electron-density difference $\Delta\rho(z')$ vs z'. The vertical dashed lines denote the midpoint between the top surface and the Na adatom. The red cumulative curve is an integral of the black transfer curve, and it shares the vertical axis, though in units of e.

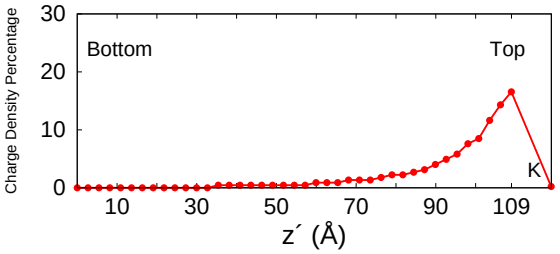

Figure 3.14: Charge density profile of a surface state vs coordinate z' profiles of the state located at $(k^0_{x'},k^0_{y'})$ in Case III. This state, at the "apparent projection," is still a top surface state.

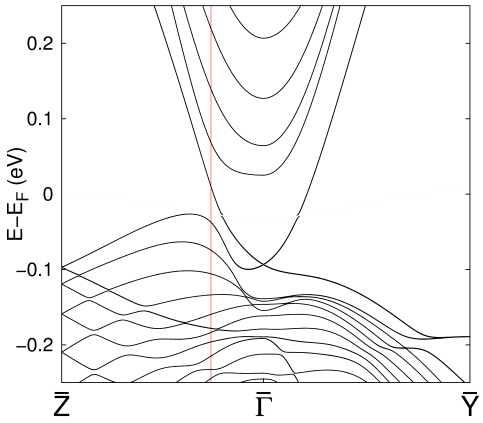

Figure 3.15: Electronic structure a slab with symmetric charge transfer. The Na_3Bi slab has one Na atom 10 Å above the top surface and 10 Å below the bottom surface. Each band has double degeneracy and there is a bulk band gap of 27.3 meV. No band crossings are found at k_z^D. The position of k_z^D is marked by a vertical line.

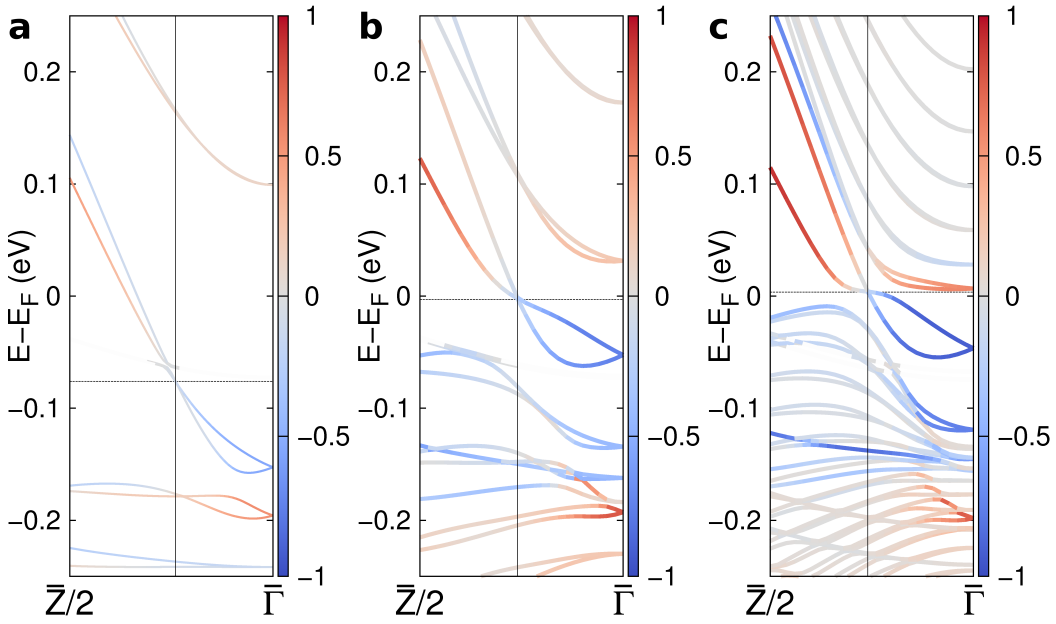

Figure 3.16: Electronic structures of adsorbed $(1\bar{2}0)$ slabs of various thickness. (a) 2.7 nm, (b) 5.5 nm, and (c) 16.3 nm thick $(1\bar{2}0)$ slabs with one K adatom 10 Å above. See Supporting Note 1 for the color scales. K-impurity bands are not shown (whited out). The 2.7 nm slab is too thin so that the charge transfer goes through the entire slab. The band crossing point does not occur at $\pm k_z^D$ $(= 0.13 \cdot 2\pi/c)$ but at $0.12 \cdot 2\pi/c$.

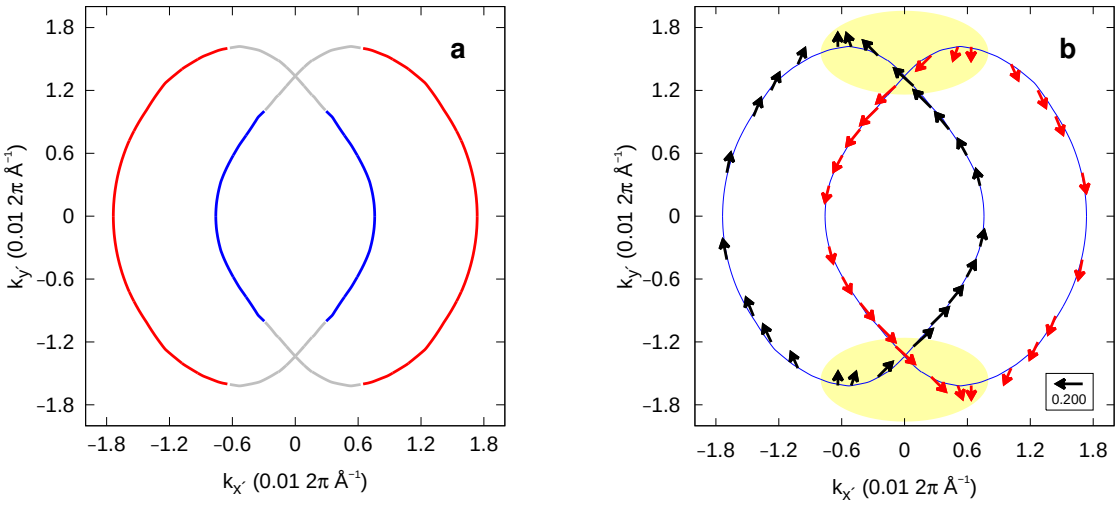

Figure 3.17: Constant energy contours for a thinner slab. (a) DFT-calculated constant energy contours of the adsorbed 5.5 nm slab at E_c and (b) spin textures at the E_c contours. Here a K adatom is adsorbed 10 Å above the surface per unit cell. The charge transfer in this case is the same as that for Case III for the thicker 10.9 nm slab. Top (bottom) surface states are identified in red (blue). In this case $k_z^D = 0.013376$ and $(k_{x'}^0, k_{y'}^0) = (0.005314,\ 0.016192)$ in units of 2π Å^{-1}.

3.6.2 Supporting Note 2: Charge Transfer

We calculate the amount of charge transfer for Cases I-IV by calculating the difference between the layer-projected electron density of the adsorbed slab and the sum of the layer-projected electron densities of the isolated Na_3Bi slab and the isolated Na atom, such as $\Delta\rho(z') = \rho(\text{adsorbed slab}) - \rho(\text{pristine slab}) - \rho(\text{isolated adsorbate})$. Here the dipole corrections are included. Figure 3.13 shows the electron densities and the difference vs the vertical distance z' from the bottom surface for the Na adatom adsorbed slab (Case II). The transferred charge penetrates into the surface up to about 3-4 nm.

3.6.3 Supporting Note 3: Cases of Optimized Adsorbates

In order to show the justification of our unconventional method of varying the amount of charge transfer or adsorbate concentration, we performed DFT calculations of a $1 \times 1 \times N$ supercell with one K adatom (at site "A" in Fig. 1c in the main text) and a $2 \times 2 \times N$ supercell with one K adatom (at one of the four possible "A" sites, Fig. 3.18), where N is the slab thickness, 5.5 nm. The former and latter structures are referred to as supercell α and β, respectively. Here we optimized the structure until the residual forces are less than 0.01 eV/Å with the K adatom and four (two) top atomic layers relaxed for supercell α (β). We use a k-point mesh of $5 \times 5 \times 1$ ($3 \times 3 \times 1$) for the former supercell α (β) for the geometry optimization and the electronic structure calculations. Their calculated band structures are shown in Fig. 3.19. In supercell α, the charge transfer occurs throughout the entire slab and so we expect that the main features of electronic structure in this case qualitatively differ from those in Cases I-IV discussed in the main text, i.e. charge transfer at the surface only. We find that in supercell α the charge transfer amount is 0.216 e per unit cell area, which is twice as large as that in Case IV, and there is a clear gap around the original Dirac node projection $\pm\mathbf{k}_D$ (as shown in the inset of Fig. 3.19a). The gapless band crossings occur far away from the original 3D Dirac node projections. In supercell β, the main features such as the charge transfer amount, the band structure, and the locations of the gapless band crossings are comparable to those in Case IV (Fig.S6b) discussed in the main text.

3.6.4 Supporting Discussion 1: Model Hamiltonian

To describe the bulk Na_3Bi we use the effective model Hamiltonian $\mathcal{H} = \epsilon_0(\mathbf{k})I_{4\times4} + \tilde{\mathcal{H}}$ constructed by using a basis set $\{|S^+_{1/2}, 1/2\rangle, |P^-_{3/2}, 3/2\rangle, |S^+_{1/2}, -1/2\rangle,$ and $|P^-_{3/2}, -3/2\rangle\}$, where the subscripts $1/2$ and $3/2$ are total angular momenta $\mathbf{J}$ of s and p orbitals, $\pm1/2$ and $\pm3/2$ are projections of $\mathbf{J}$ onto the c or z axis, and the superscripts $\pm$ correspond to the parity values. Here $\epsilon_0(\mathbf{k}) = C_0 + C_1k_z^2 + C_2(k_x^2 + k_y^2)$ and $I_{4\times4}$ is a 4×4 identity matrix. The

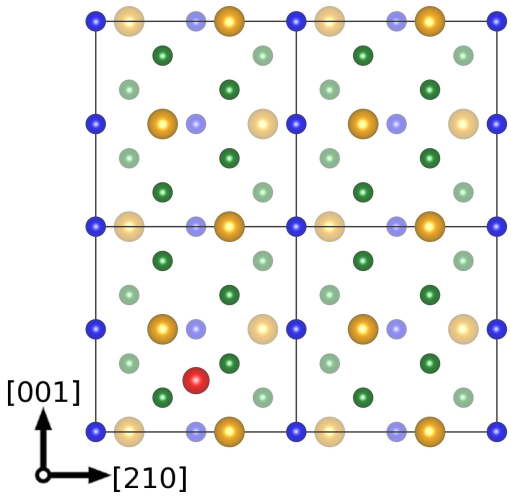

Figure 3.18: The $2 \times 2\times$ supercell for a 5.5 nm slab before geometry relaxation. The single adatom is located at only one of the four equivalent sites.

Hamiltonian was first suggested in Ref. 99. The Hamiltonian $\tilde{\mathcal{H}}$ reads

$$\begin{pmatrix} M(k) & iAk_+ & 0 & B(k)^\star \\ -iAk_- & -M(k) & B(k)^\star & 0 \\ 0 & B(k) & M(k) & iAk_- \\ B(k) & 0 & -iAk_+ & -M(k) \end{pmatrix},$$

where $M(\mathbf{k}) = M_0 - M_1 k_z^2 - M_2(k_x^2 + k_y^2)$, $k_\pm = k_x \pm ik_y$, $B(\mathbf{k}) = \alpha k_z k_+^2$, and $B(\mathbf{k})^\star$ is its complex conjugate. Here $C_0 = -0.06382$ eV, $C_1 = 8.7536$ eV Å^2, $C_2 = -8.4008$ eV Å^2, $M_0 = -0.08686$ eV, $M_1 = -10.6424$ eV Å^2, $M_2 = -10.3610$ eV Å^2, and $A = 2.4598$ eV Å, from fitting [99] of the bulk band structure near Γ, but the parameter α is unknown. Note that our Hamiltonian $\tilde{\mathcal{H}}$ is slightly modified from the literature, considering that our coordinates differ from those in Refs. 99, 160. For $\alpha = 0$, the lower 2×2 matrix of $\mathcal{H}$ can be obtained from the upper 2×2 matrix by replacing k_y by $-k_y$, and the upper (lower) 2×2 matrix represents the up-sector (down-sector) Weyl fermions [160]. For simplicity, henceforth we consider $\alpha = 0$ or $B(\mathbf{k}) = 0$. After applying a canonical transformation [160] to the *down*-sector 2×2 matrix $\mathcal{H}'$ with a unitary matrix $\mathcal{U} = (I_2 + i\sigma_y)/\sqrt{2}$, we obtain the transformed Hamiltonian $\mathcal{H}^d_{2\times2} = \mathcal{U}^{-1}\mathcal{H}'\mathcal{U}$ as

$$\begin{pmatrix} \epsilon_0(\mathbf{k}) - Ak_y & M(\mathbf{k}) + iAk_x \\ M(\mathbf{k}) - iAk_x & \epsilon_0(\mathbf{k}) + Ak_y \end{pmatrix}.$$

The up-sector 2×2 Hamiltonian matrix $\mathcal{H}^u_{2\times2}$ can be obtained from $\mathcal{H}^d_{2\times2}$ by interchanging k_y with $-k_y$. From $\mathcal{H}^u_{2\times2}$ and $\mathcal{H}^d_{2\times2}$, we obtain energy eigenvalues of

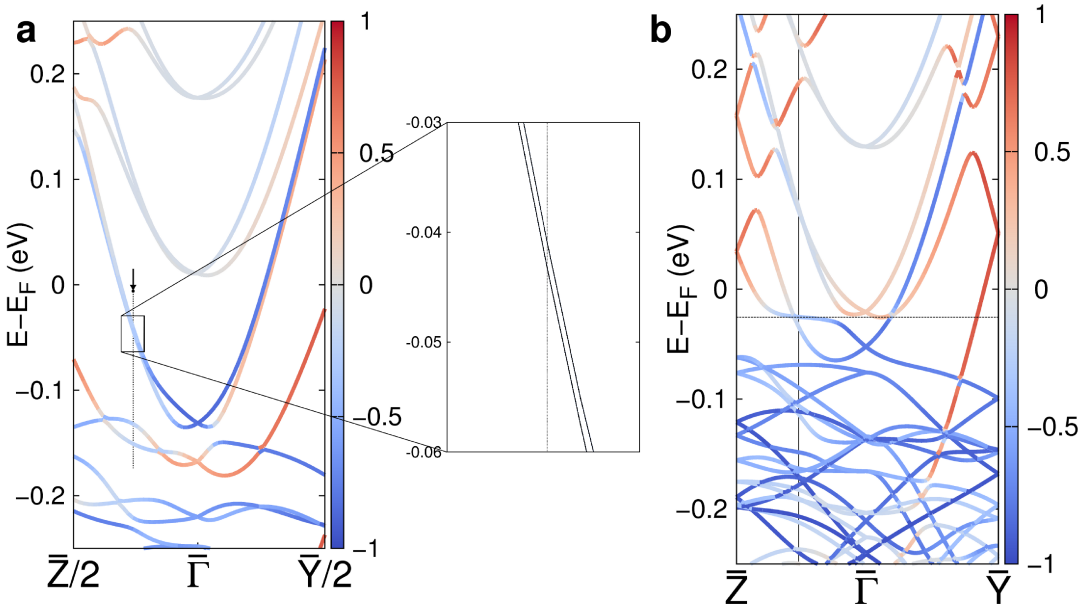

Figure 3.19: Electronic structure of slabs with smaller and larger unit cells. (a) Band structure of the $1 \times 1\times$ 5.5 nm $(1\bar{2}0)$ slab with one K adatom at the optimized distance (2.69 Å). (Inset) The two bands emphasized remain gapped at the original Dirac node projection. The surface state colorization is removed for clarity. (b) Band structure of the $2 \times 2\times$ 5.5 nm $(1\bar{2}0)$ slab with one K adatom at the optimized distance (2.74 Å). Top (bottom) surface states are identified in red (blue). Unfolding of the bands was not carried out in (b).

$\epsilon_0(\mathbf{k}) \pm \sqrt{M^2(\mathbf{k}) + A^2(k_x^2 + k_y^2)}$. Here the square root vanishes at $(0, 0, \pm\sqrt{M_0/M_1})$, which are the 3D Dirac nodes.

We first examine the Fermi-arc surface states in the absence of the asymmetric charge transfer. We focus on the down-sector Hamiltonian, considering a semi-infinite slab occupying $x > 0$. The top surface is located at $x = 0$, while the vacuum is on the $x < 0$ side. After replacing k_x by $-i\partial_x$, $\mathcal{H}^d_{2\times 2}$ becomes surface Hamiltonian $\mathcal{H}^d_s$:

$$\begin{pmatrix} C_0 + C_1 k_z^2 + C_2(-\partial_x^2 + k_y^2) - Ak_y & -M_1(k_z^2 - m) - M_2(-\partial_x^2 + k_y^2) + A\partial_x \\ -M_1(k_z^2 - m) - M_2(-\partial_x^2 + k_y^2) - A\partial_x & C_0 + C_1 k_z^2 + C_2(-\partial_x^2 + k_y^2) + Ak_y \end{pmatrix},$$

where $\sqrt{m} = \sqrt{M_0/M_1}$. The top surface states at $x = 0$ must have a form of e^{-px} with $p > 0$. Eigenvectors of $\mathcal{H}^d_s$ can be written as a linear combination of $e^{-p_1 x}(1, Q_1)$ and $e^{-p_2 x}(1, Q_2)$, where p_1 and p_2 are positive. Thus, applying the boundary conditions at $x = 0$ [160, 170], we find that the Fermi-arc surface states at a given energy E can be obtained by solving the following equations numerically.

$$\begin{aligned} Q_1 &= Q_2, \qquad Q_i \equiv \frac{C_0 + C_1 k_z^2 + C_2(-p_i^2 + k_y^2) - Ak_y - E}{M_1(k_z^2 - m) + M_2(-p_i^2 + k_y^2) + Ap_i}, \\ p_{1,2}^2 &\equiv \frac{1}{2(C_2^2 - M_2^2)}[2(C_2 K + M_2 J) - A^2 \\ &\quad \pm\sqrt{(2(C_2 K + M_2 J) - A^2)^2 + 4(M_2^2 - C_2^2)(K^2 - J^2 - A^2 k_y^2)}], \\ K &\equiv C_0 + C_1 k_z^2 + C_2 k_y^2 - E, \quad J \equiv -M_1(k_z^2 - m) - M_2 k_y^2. \end{aligned} \tag{3.1}$$

The above equation is equivalent to equation (25) in Ref. 160 when k_x and k_y are interchanged. The solution of equation (3.1) indicates that the top surface states exist only on the $k_y < 0$ side ($k_{x'} > 0$ side). Similarly, the bottom surface states can be obtained by considering that p_1 and $p_2 < 0$ in equation (3.1). Then we find that the bottom surface states appear only on the $k_y > 0$ side ($k_{x'} < 0$ side). For the up-sector, the bottom and top surface states exist on the opposite sides of the k_z axis ($k_{y'}$ axis). The calculated CECs of the Fermi-arc surface states at $E = 0$ from this model are shown as black curves in Fig. 3.6c in the main text.

Now in the presence of the asymmetric charge transfer at the top surface, a new surface Hamiltonian $\bar{\mathcal{H}}^d_s$ can be written as $\mathcal{H}^d_s + \mathrm{diag}(-V, 0)$:

$$\begin{pmatrix} C_0 + C_1 k_z^2 + C_2(-\partial_x^2 + k_y^2) - Ak_y - V & -M_1(k_z^2 - m) - M_2(-\partial_x^2 + k_y^2) + A\partial_x \\ -M_1(k_z^2 - m) - M_2(-\partial_x^2 + k_y^2) - A\partial_x & C_0 + C_1 k_z^2 + C_2(-\partial_x^2 + k_y^2) + Ak_y \end{pmatrix}.$$

Here the new term $V > 0$ accounts for the charge transfer to the top surface. The small change in the surface Hamiltonian results in solving equation (3.1) with different definitions

of Q_i and $p_{1,2}$:

$$\begin{aligned} Q_i &\equiv \frac{C_0 + C_1 k_z^2 + C_2(-p_i^2 + k_y^2) - A k_y - V - E}{M_1(k_z^2 - m) + M_2(-p_i^2 + k_y^2) + A p_i}, \\ p_{1,2}^2 &\equiv \frac{1}{2(C_2^2 - M_2^2)}[2(C_2 K + M_2 J) - A^2 - C_2 V \\ &\pm\sqrt{(2(C_2 K + M_2 J) - A^2 - C_2 V)^2 + 4(M_2^2 - C_2^2)(K^2 - J^2 - A^2 k_y^2 - A k_y V - K V)}]. \end{aligned} \tag{3.2}$$

The calculated CECs of the surface states at $E = 0$ from this model are shown as black and red curves in Fig. 3.6d in the main text.

3.6.5 Supporting Discussion 2: Fermi-arc States with Broken Bulk Symmetry

We discuss the case that the charge transfer goes throughout an entire $(1\bar{2}0)$ slab. Now the model Hamiltonian for the bulk has to be modified. First we focus on an effect of broken inversion symmetry at the bulk level. The simplest bulk Hamiltonian (modified from Ref. 99) is now

$$\begin{pmatrix} M(k) & iAk_+ + V & 0 & B(k)^\star \\ -iAk_- + V & -M(k) & B(k)^\star & 0 \\ 0 & B(k) & M(k) & iAk_- + V \\ B(k) & 0 & -iAk_+ + V & -M(k) \end{pmatrix}, \tag{3.3}$$

where $V > 0$. Let us assume that $B(k) = 0$. Then after the unitary transformation [160] (discussed in Supporting Discussion 1), the down-sector Hamiltonian becomes

$$\begin{pmatrix} \epsilon_0(\mathbf{k}) - Ak_y - V & M(\mathbf{k}) + iAk_x \\ M(\mathbf{k}) - iAk_x & \epsilon_0(\mathbf{k}) + Ak_y + V \end{pmatrix}.$$

The eigenvalues of the above Hamiltonian are given as

$$E_{\mathrm{d}} = \epsilon_0(\mathbf{k}) \pm \sqrt{(Ak_y + V)^2 + M^2(\mathbf{k}) + (Ak_x)^2}, \tag{3.4}$$

where the square root goes to zero at $\mathbf{k}^{\mathrm{d}} = (0, -V/A, \pm\sqrt{\{M_0 - M_2(V/A)^2\}/M_1})$. For the up-sector Hamiltonian, the eigenvalues are $E_{\mathrm{u}} = \epsilon_0(\mathrm{k}) \pm \sqrt{(-Ak_y + V)^2 + M^2(\mathrm{k}) + (Ak_x)^2}$, where the square root vanishes when $\mathbf{k}^{\mathrm{u}} = (0, +V/A, \pm\sqrt{\{M_0 - M_2(V/A)^2\}/M_1})$. Therefore, we now find that the Dirac nodes previously at $\mathbf{k} = (0, 0, \pm\sqrt{M_0/M_1})$ for $V = 0$ are separated into two pairs of Weyl nodes at $\mathbf{k}^{\mathrm{u},d} = (0, \pm V/A, \pm\sqrt{\{M_0 - M_2(V/A)^2\}/M_1})$. Here the k_z components of $\mathbf{k}^{\mathrm{d}}$ and $\mathbf{k}^{\mathrm{u}}$ are always *less* than the k_z^D values, $\pm\sqrt{M_0/M_1}$, in magnitude since M_0, M_1, and $M_2 < 0$. The shift of the Weyl nodes along the k_y axis is proportional to

V. When following a similar step to that discussed in Supporting Information Discussion 1, we find that the projections of the 3D Dirac nodes at the $(1\bar{2}0)$ surface are also shifted accordingly. However, the trend of the shift in this case does *not* agree with that from our DFT calculations. In the latter the *apparent* projections (not true projections) of the Weyl nodes, $(k^0_{x'}, k^0_{y'})$, are shifted along the positive k_z axis ($k_{y'}$ axis) in the upper half plane, while they are shifted along the negative k_z axis ($k_{y'}$ axis) in the lower half plane. See Figs. 3.4c,e in the main text. However, they are moved in the opposite directions for this modified model Hamiltonian.

Although the above result seems to be convincing, there is one caveat: the separated Weyl nodes have C_2 symmetry about the x axis. With the broken inversion symmetry at the bulk level, the C_3 symmetry is also broken. This leads to a nonzero $B(k)$ term such as $B_1 k_z$ in the modified model Hamiltonian for the bulk, which is crucial. This term opens up an energy gap at the Dirac or Weyl nodes [99] and so the system is not a DSM or WSM anymore. We include $B(k) = B_1 k_z$ in equation (1) and diagonalize the Hamiltonian. By varying parameter values of B_1 and V with all other parameter values fixed as those in Ref. 99, we find that an increase of the V term lowers the gap at the Weyl nodes.

Chapter 4

Magnetic-field-induced Weyl semimetal

This chapter is based in substantial part on a manuscript in progress. There are sections which appear more didactic than the previous chapters and which may not feature in a final published version. Nevertheless, these are included as they extend the reader's understanding of the utilized methods.

4.1 Introduction

Weyl semimetals (WSMs) are materials in which the bulk conduction and valence bands touch at a discrete number of points (Weyl nodes) in the Brillouin zone (BZ) in the absence of either inversion symmetry (IS) or time reversal symmetry (TRS) or both. The Weyl nodes are topologically protected by nonzero Chern numbers associated with the nodes, and the surface manifestation of this bulk topological nature is the existence of open-contour Fermi arc surface states which connect the projections of the Weyl nodes of opposite chirality. The topological properties persist under small perturbations, as the Weyl nodes can only be removed if an oppositely charged pair of Weyl nodes annihilates at the same point in the BZ. First theoretically proposed in TRS-broken pyrochlore iridates [64], IS-broken TaAs was predicted to be a WSM [78] and experimentally measured shortly thereafter [65, 66]. Other exotic types of WSMs have since been predicted, including Type-II WSMs (which result from the touching of electron- and hole-pockets) [68] and multiple-topological-charge WSMs (so-called "double" or "triple" WSMs) [92, 171]. WSMs have shown novel properties deriving from nonzero Berry curvature, such as the chiral magnetic effect, anomalous thermoelectric properties [172], and unique quantum oscillations [75, 173].

IS-broken WSMs have been more studied than the TRS-broken WSMs. The former has a large number of Weyl nodes near the Fermi level, e.g. 24 nodes in TaAs and its family of

WSMs [66, 78, 174]. However, one can also achieve the WSM state by breaking TRS in topological Dirac semimetals (DSMs) via an applied external magnetic field, **B**. Topological Dirac semimetals have TRS and IS, and they have an even number of fourfold band crossings in the BZ which occur along a rotational axis [140]. The fourfold band crossings, Dirac nodes, can be thought of as two copies of Weyl nodes superimposed on each other and stabilized by the crystalline symmetry; application of an external magnetic field splits the Dirac nodes into Weyl nodes of opposite chirality. Unlike in TaAs which has twenty-four Weyl nodes, the magnetically-induced DSM-to-WSM has much fewer Weyl nodes (here, eight). This is a particularly attractive avenue because the initial Dirac nodes are symmetry-protected and occur along a high-symmetry direction, rather than existing at an arbitrary point in the BZ. Two topological DSMs have been experimentally discovered to date, Na_3Bi [100, 101] and Cd_3As_2 [102, 103]. TRS-breaking induced by a magnetic field would split the Dirac nodes into multiple Weyl nodes with nonzero Chern numbers [175]. So far, magnetic-field-induced WSMs have been mostly studied within 4×4 effective models where the parameter values were fitted to density functional theory (DFT) calculated band structures [175, 176].

We develop from first principles a Wannier-function-based tight-binding (WF-TB) model for the topological DSM Na_3Bi in order to examine the magnetically-induced WSM state and the resultant Fermi arc surface states. We first obtain atom-centered Wannier functions (WFs) from a DFT-calculated electronic structure in the absence of a **B**-field and spin-orbit coupling (SOC). Then we create a tight-binding model based on the WFs by adding atomic-like SOC and a Zeeman term. We check that the mirror symmetry and threefold rotational symmetry are preserved in the presence of the magnetic field. One caveat to this procedure is that we are not interested in maximally localized WFs: the existence of maximally localized WFs relies on the fact that the band characteristics are not abruptly modified in momentum **k**-space [24, 26]. However, the crucial band inversion in topological DSMs, even in the absence of SOC, is such an abrupt change. Thus the WFs we obtain and somewhat more delocalized than what one typically hopes for in a WF-TB model.

We find that upon application of the **B**-field along the crystal c-axis, each Dirac node splits into two single Weyl nodes with Chern number ± 1 and two double Weyl nodes with Chern number ± 2. In the 4×4 effective models, higher-order cubic terms (which respect the crystal symmetry) are ignored, and so it is commonly known that the Dirac nodes would each split into two single Weyl nodes with opposite chirality [176]. Ignoring the higher-order cubic terms was also reasonable since the DFT-calculated band structure near the Γ point can be well-fitted without them. Only Cano *et al.* explicitly discussed the possibility of having double Weyl nodes when the higher-order terms are included in such effective models for magnetic-field-induced WSMs [175].

Our calculations of the Chern numbers of the Weyl nodes unambiguously reveal the necessity of the higher-order terms, which are directly associated with the existence of double Weyl nodes. With a magnetic field strength of 25 meV oriented along the c-axis, the four Weyl nodes appear approximately 35 meV above the Fermi level and 60 meV below the Fermi level. The single and double Weyl nodes with the same sign Chern numbers are close to each

other, whereas the Weyl nodes with negative Chern numbers are well separated from those with positive Chern numbers, as detailed in Table 4.3. By using a surface Green's function method [178] based on our tight-binding model with a magnetic field, we identify Fermi arc states on the $(1\bar{2}0)$ surface. We also reveal an interesting interplay between the Fermi arc surface states and other topological surface states as a function of chemical potential by carefully considering the associated Chern numbers of Fermi surface (FS) sheets, in the same vein as Gosálbez-Martínez *et al.* [179]. The number of calculated Fermi arc surface states as a function of chemical potential corroborates our calculated Chern numbers. Our tight-binding model can be used to compute various physical properties induced by the nonzero Berry curvature, including anomalous transverse Hall and thermal conductivities. Our findings can also be applied to topological DSM Cd_3As_2 in the presence of an external magnetic field.

4.2 Crystal Structure of Na_3Bi

We consider bulk Na_3Bi in space group $P6_3/mmc$ (No. 194) with experimental lattice constants of $a = 5.448$ Å and $c = 9.655$ Å [99] and no geometry relaxation is performed. There are two inequivalent Na sites, 2b and 4f, with z=0.5827 for the latter in the Wyckoff convention, and these are shown in Figure 4.1 in blue and green, respectively. There is one inequivalent Bi site, 2c in the Wyckoff convention shown in gold in Fig. 4.1. The site symmetries of 2b, 4f, and 2c sites are D_{3h}, C_{3v}, and D_{3h}, respectively. The primitive unit cell in real space consists of six Na atoms and two Bi atoms, and an associated first Brillouin zone (BZ) is shown in Fig. 4.1(d). The bulk crystal has inversion symmetry, a 6_3 screw axis along the c-axis (or z-axis), and four mirror planes (xy and yz planes, and a further two planes equivalent to the latter by rotational symmetry). For convenience, we will use the $z' \perp (1\bar{2}0)$ non-primitive unit cell for all that follows, unless specified otherwise. The global primitive cell coordinates are unprimed and the local $(1\bar{2}0)$ cell coordinates are primed. The unit cell has a rectangular shape and its dimension is $9.436 \times 9.655 \times 5.448$ Å^3. The reason we use the non-primitive unit cell will be discussed later.

4.3 Construction of the Wannier-function-based Tight-binding Model

We first perform DFT calculations for bulk Na_3Bi without SOC and generate the Wannier functions based on the DFT-calculated Bloch states. We then construct a WF-TB model by adding atomic-like SOC and a Zeeman term.

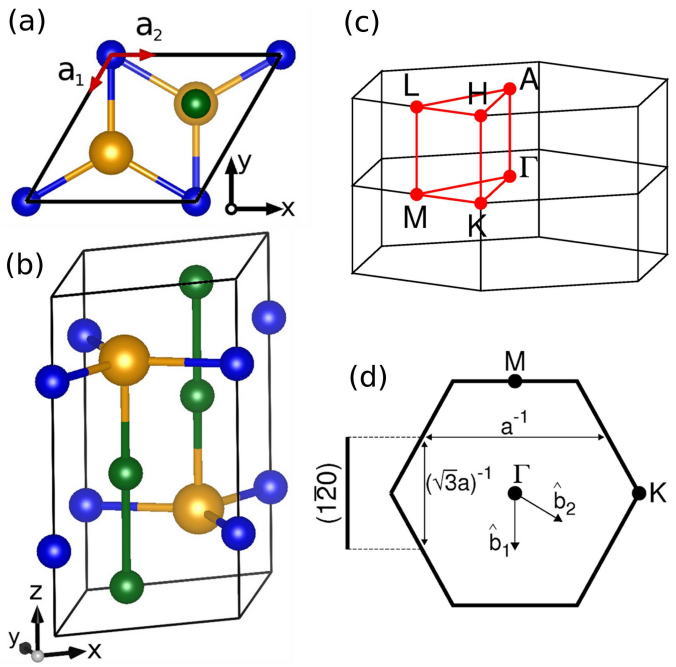

Figure 4.1: Crystal structure and primitive cell Brillouin zone of Na_3Bi. (a) Top-down view of the primitive hexagonal unit cell of Na_3Bi which crystallizes in the $P6_3/mmc$ hexagonal structure. (b) The primitive unit cell at a slight perspective angle. The in-plane lattice vectors are shown in (a). (c) The primitive cell first Brillouin zone (BZ) with high-symmetry points marked. (d) A top-down view of the primitive cell first BZ and the projection onto the $(1\bar{2}0)$ surface BZ. (Panels (a), (b), and (d) are used with permission [139].)

4.3.1 Initial DFT Calculations

We perform the *ab initio* calculations using the DFT code Quantum Espresso (QE) [183] within the Perdew-Burke-Ernzerhof (PBE) generalized-gradient approximation (GGA) [7] without SOC. We used the Na.pbe-spn-kjpaw_psl.0.2.UPF and Bi.pbe-dn-kjpaw_psl.0.2.2.UPF projector augmented wave (PAW) pseudopotentials [184] with an energy cutoff of 50 Ry and smearing of 0.001 Ry. We use the $c \perp (001)$ primitive hexagonal unit cell to calculate the band structure and the $z' \perp (1\bar{2}0)$ non-primitive unit cell for all that follows. We use an $11 \times 11 \times 7$ Monkhorst-Pack k-point mesh in the former case and a $7 \times 7 \times 15$ mesh in the latter case. We also carry out the electronic structure calculation using the DFT code VASP [134] with the PBE GGA and PAW pseudopotentials in the absence of SOC and with an $11 \times 11 \times 5$ mesh. We find excellent agreement between the QE-calculated and VASP-calculated electronic structures, as a consistency check.

4.4 Generation of the Wannier functions

A Wannier function, $|\mathbf{R}+\tau_\alpha, n\rangle$ centered at a position τ_α relative to the origin of the real space unit cell denoted by $\mathbf{R}$, is a Fourier transform of Bloch states, $\psi_{n\mathbf{k}}(\mathbf{r}) = u_{n\mathbf{k}}e^{i\mathbf{k}\cdot\mathbf{r}}$, over the reciprocal space. n is a band index and $u_{n\mathbf{k}}$ is a lattice-periodic function.

$$|\mathbf{R}+\tau_\alpha, n\rangle = \frac{V}{(2\pi)^3}\int_{BZ} d\mathbf{k}\; e^{-i\mathbf{k}\cdot(\mathbf{R}+\tau_\alpha)}|\psi_{nk}(\mathbf{r})\rangle. \tag{4.1}$$

The home cell, $\mathbf{R}=\mathbf{0}$, contains N_w WFs and there are $N_b > N_w$ bands within the outer window of WANNIER90 [19]. Without the spin index, the tight-binding Hamiltonian is given by,

$$\mathcal{H}_{\alpha\beta} = \sum_{\mathbf{R}} e^{i\mathbf{k}\cdot\mathbf{R}}\; t_{\alpha\beta}(\mathbf{0}-\mathbf{R}), \tag{4.2}$$

$$t_{\alpha\beta}(\mathbf{0}-\mathbf{R}) = \langle \mathbf{0}+\tau_\alpha|\mathcal{H}|\mathbf{R}+\tau_\beta\rangle, \tag{4.3}$$

with α and β= $1, 2, ..., N_w$.

There are some criteria by which to judge the acceptability of the generated WFs: (i) they must reproduce the DFT-calculated band structure as closely as possible near the Fermi level with and without SOC, (ii) they should maintain the crystal symmetry with and without an external magnetic field, (iii) the Wannier centers must be at the atomic sites, (iv) the WFs should be either a pure atomic orbital or a linear combination of them, (v) the spread of each WF should be as small as possible (reasonably within the home unit cell), and (vi) a smaller number of WFs is desirable to reduce the size of the Hamiltonian matrix. Criteria (iii) and (iv) stem from including atomic-like SOC and the Zeeman term.

4.4.1 Wannier Functions From the Primitive Hexagonal Cell

We used the bulk primitive hexagonal cell initially to construct the WFs. We removed the inner (frozen) window since Na_3Bi is already semimetallic with a band inversion. We did disentangle the bands but did not minimize the localization functional, so that the WFs would be as atomically centered as possible. Aside from the parameters we varied in WANNIER90, we encountered the following results in the pursuit of WFs which satisify our criteria:

1. 14 WFs: Consisting of Bi-s and Bi-3p orbitals on each of the two bismuth sites and an Na-s orbital on each of the six sodium sites, excellent agreement was found without SOC along high-symmetry directions. However, the addition of SOC resulted in breaking of band degeneracies of up to 0.5 meV. The pattern of this discrepancy revealed

the C_2 symmetry of the Wannier functions. The C_3 symmetry-lacking energy contours are plotted in Figure 4.2(a).

2. Slater-Koster [177]: There needed to be some way to achieve the rotational symmetry in the energy contours. We attempted to manually symmetrize the hopping parameters and examine if a suitable cutoff distance could be imposed to make the model capture only the most important hoppings. Instead we found that the hopping parameters remained significant far into neighboring unit cells even along the rotational axis: the Dirac node was not reproduced without a cutoff distance larger than 11 Å. Upon abandoning any cutoff, it became clear that the WFs themselves did not have the requisite symmetry, so there was no hope of merely averaging and symmetrizing the hopping parameters into a large set of Slater-Koster parameters.

3. 8 WFs: Consisting of Bi-s and Bi-3p orbitals on each of the two bismuth sites, excellent agreement was found without SOC along high-symmetry directions again (see Fig. 4.3(a)]. The degeneracy in the presence of SOC is maintained, but the energy contours in the global xy-plane revealed a more pronounced C_2 symmetry [see Fig. 4.2(b)]. Indeed, application of the magnetic field resulted in a C_2-symmetric line-node in the $k_z = 0$ plane. The resulting WFs were atomically centered (Wannier centers deviating no more than a 0.005 Å from the atomic site, see Table 4.1).

We also looked at a few other choices of trial orbitals, each of which contained these four orbitals per bismuth site plus: (1) s-orbitals on in-plane (blue, 2b) sodium atoms, which would create a TB model of layered planes related by the 6_3-screw symmetry and (2) s-orbitals on out-of-plane (green, 4f) sodium atoms, since the hopping parameters remained significant even between vertical copies of the unit cell and the Bi-s orbitals had some weight on the sodium atoms. Each of these resulted in a substantially worse band structure with SOC and more greatly spread WFs; they were only effective at reproducing the band structure if restricted to the valence bands, which is useless as the Dirac node will not be present. Thus item 3 gave the procedure and parameters for the best WFs we could achieve in the primitive hexagonal cell. The positions of the Wannier centers and WF spreads are listed in Table 4.1.

4.4.2 Wannier Functions from the $(1\bar{2}0)$ cell

The energy contours from item 3 clearly lack C_3 symmetry despite other criteria being met. We use the $(1\bar{2}0)$ cell to generate a set of WFs using the same parameters as in item 3, but the non-primitive cell has twice the volume as the primitive hexagonal cell, and so we use a basis set of projection orbitals which is twice the size. One intuition of the sensibility of this choice is that this adds two bismuth sites which are related to the bismuth sites in the primitive cell by the 6_3 screw symmetry [or C_3 symmetry if one considers just those bismuth atoms in the same (001) atomic plane]. This choice of unit cell is also a matter of

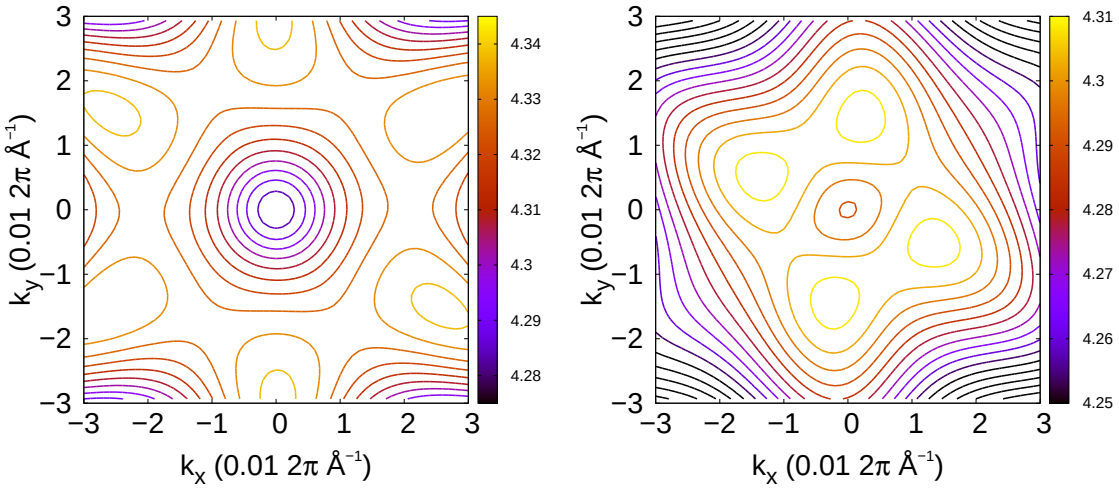

Figure 4.2: Constant energy countours exhibiting broken C_3 symmetry. (a) Constant energy contours of the top valence band in the k_z=0 plane as calculated from the WF-TB model of item 1. There is not quite C_3 symmetry, as seen in the vertices of the hexagonal feature at the edge of the figure. (b) Constant energy contours of the top valence band in the k_z=0 plane as calculated from the WF-TB model of item 3. The C_2 symmetry is clear. In both panels, SOC is included and the colorscale is for the energy (eV).

Table 4.1: Cartesian positions (Å) of the Wannier functions for the primitive hexagonal cell with their spreads. The atomic positions are listed at the top of the table for ease of comparison. All coordinates are *global*.

Atom	Orbital	x	y	z	Spread (Å^2)
Bi 1		2.72400	-1.57270	2.41375	
Bi 2		0.00000	-3.14540	7.24125	
1	s	2.72400	-1.57270	2.41375	15.77
2	s	0.00000	-3.14540	7.24125	15.77
1	p_z	2.72400	-1.57270	2.41375	4.49
1	p_x	2.72400	-1.57720	2.41375	4.42
1	p_y	2.72400	-1.56802	2.41375	4.42
2	p_z	0.00000	-3.14540	7.24125	4.49
2	p_x	0.00000	-3.14091	7.24125	4.42
2	p_y	0.00000	-3.15009	7.24125	4.42

convenience: to investigate the side-surface (on which we could expect to find Fermi arcs), we desire a unit cell which has the surface specified as a plane; that is, at least there needs

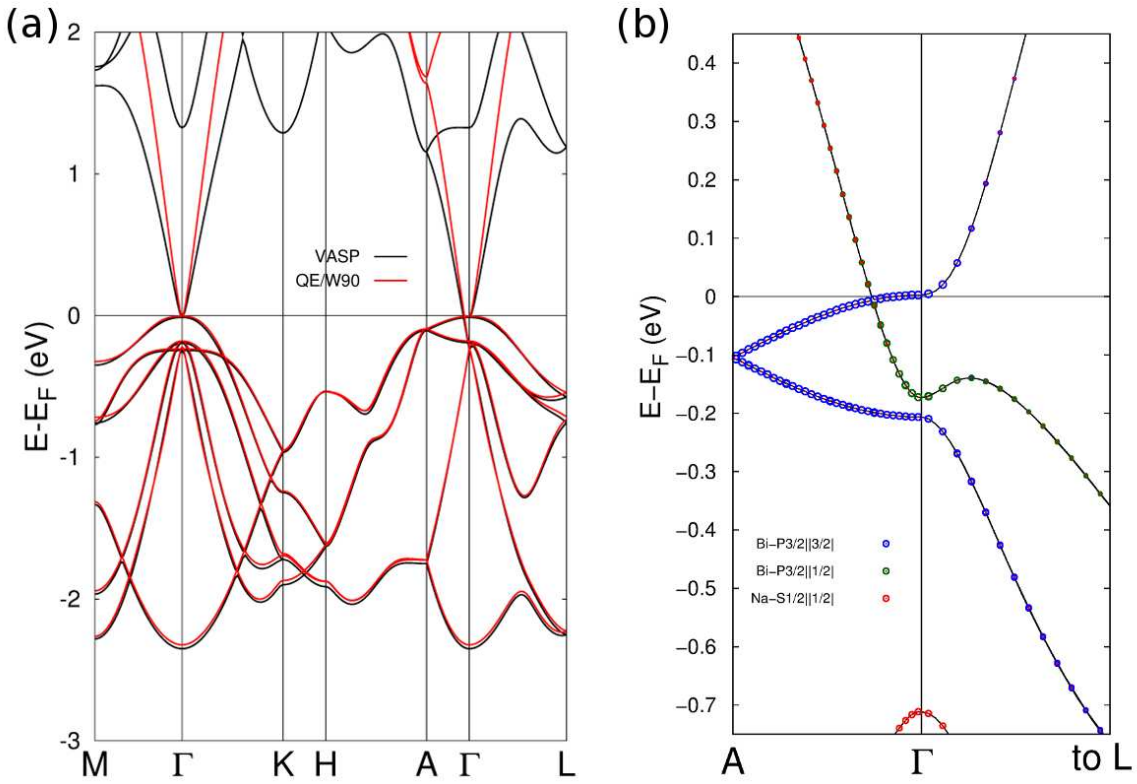

Figure 4.3: Band structure of bulk Na_3Bi using the primitive hexagonal cell. (a) Comparison of the bulk band structure without SOC of Na_3Bi using the primitive hexagonal cell calculated with VASP versus with the WF-TB Hamiltonian (using Quantum Espresso as the source electronic structure calculation). (b) Band structure near the Dirac node and Γ point with SOC. The size of the circles indicates the relative weight onto $|j, |m_j|\rangle$ states; the Dirac node is a band crossing between states with different rotational eigenvalues, $|m_j| = \frac{3}{2}$ and $|m_j| = \frac{1}{2}$, and the majority of the band character comes from bismuth orbitals.

to be two surface lattice vectors which define the surface plane, or, stronger, the third lattice vector should be normal to the surface plane. Since the $(1\bar{2}0)$ cell is a rectangular prism, both of these possibilities are satisified. This allows one to use the iterative Green's function method [178] and to efficiently construct a finite slab model within Wannier Tools [180]. The main differences between this doubled basis set and the smaller basis set of the primitive hexagonal cell are: a greater offset of the s-orbitals (by approximately 0.04 Å) and improved spread for all the WFs (by approximately 2.5 Å^2 for the s-orbitals and 0.2 Å^2 for the p-orbitals). One can observe the band-folding from using the non-primitive cell in the bulk band structure and also the good agreement with the DFT-calculated bands in Fig 4.5.

We use Wannier90 [19] to develop a tight-binding Hamiltonian from s-, $p_{x'}$-, $p_{y'}$-, and $p_{z'}$-orbitals centered on the four bismuth atoms in the $(1\bar{2}0)$ unit cell. We do not use an inner

(frozen) window and we use a disentanglement window of $[-3.86, 5.44]$ eV with respect to the Fermi level. We plot the Wannier functions for one of the s- and $p_{z'}$-orbitals in Figure 4.4. We see the nearly pure atomically-centered orbitals, though the s-orbital WFs are expanded to include pockets on the nearby Na-atoms, and the p-orbital WFs have small pockets at nearby Na-atoms. The positions of the Wannier centers and WF spreads are listed in Table 4.2. Figure 4.6(a) shows that C_3 symmetry is preserved in the constant energy contours of the top of the valence band with our set of WFs for the $(1\bar{2}0)$ cell. Thus we achieve the atom-centered and substantially-localized features of the primitive hexagonal cell WFs, but crucially recover C_3 symmetry at the cost of a larger set of WFs.

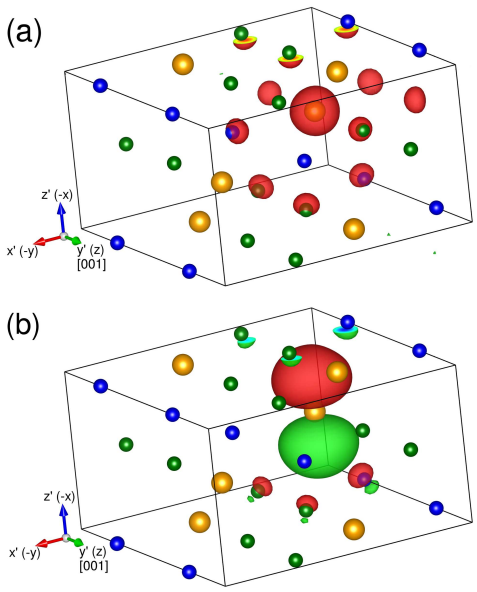

Figure 4.4: s- and p-orbital Wannier functions in the $(1\bar{2}0)$ cell. (a) Wannier function corresponding to an s-orbital. (b) Wannier function corresponding to a $p_{z'}$-orbital. An isolevel of 3 is chosen in both panels. Bi atoms are orange and Na atoms are blue (Wyckoff site 2b) and green (4f). Green Na atoms are vertically oriented relative to the Bi atoms in the primitive hexagonal cell.

4.4.3 Addition of SOC and the Zeeman term

Assuming the atomically-centered Wannier functions are pure states of the orbitals we projected onto, spin-orbit coupling is added to the home unit cell terms directly. The matrix

Table 4.2: Cartesian positions (Å) of the Wannier functions for the $(1\bar{2}0)$ cell with their spreads. The atomic positions are listed at the top of the table for ease of comparison. All coordinates are *local*.

Atom	Orbital	x'	y'	z'	Spread (Å^2)
Bi 1		1.57270	2.41375	2.72400	
Bi 2		3.14540	7.24125	0.00000	
Bi 3		6.29081	2.41375	0.00000	
Bi 4		7.86351	7.24125	2.72400	
1	s	1.53021	2.41377	2.72400	13.30
2	s	3.18791	7.24123	0.00000	13.30
1	$p_{z'}$	1.56990	2.41375	2.72400	4.36
1	$p_{x'}$	1.57225	2.41375	2.72400	4.36
1	$p_{y'}$	1.56931	2.41375	2.72400	3.99
2	$p_{z'}$	3.14821	7.24125	0.00000	4.36
2	$p_{x'}$	3.14587	7.24125	0.00000	4.36
2	$p_{y'}$	3.14880	7.24125	0.00000	3.99
3	s	6.24840	2.41377	0.00000	13.30
4	s	7.90603	7.24123	2.72400	13.30
3	$p_{z'}$	6.28801	2.41375	0.00000	4.36
3	$p_{x'}$	6.29034	2.41375	0.00000	4.36
3	$p_{y'}$	6.28742	2.41375	0.00000	3.99
4	$p_{z'}$	7.86632	7.24125	2.72400	4.36
4	$p_{x'}$	7.86398	7.24125	2.72400	4.36
4	$p_{y'}$	7.86691	7.24125	2.72400	3.99

form of SOC in the $\{|p_{z'},\uparrow\rangle, |p_{x'},\uparrow\rangle, |p_{y'},\uparrow\rangle, |p_{z'},\downarrow\rangle, |p_{x'},\downarrow\rangle, |p_{y'},\downarrow\rangle\}$ basis is

$$H_{SOC} = \lambda \vec{\boldsymbol{L}} \cdot \vec{\boldsymbol{\sigma}} = \frac{\lambda}{2} \begin{pmatrix} 0 & 0 & 0 & 0 & -1 & i \\ 0 & 0 & -i & 1 & 0 & 0 \\ 0 & i & 0 & -i & 0 & 0 \\ 0 & 1 & i & 0 & 0 & 0 \\ -1 & 0 & 0 & 0 & 0 & i \\ -i & 0 & 0 & 0 & -i & 0 \end{pmatrix}, \tag{4.4}$$

with λ the SOC parameter. We found that $\lambda = 1.165$ eV reproduces the DFT band structure around the Fermi level the best, which is to be favorably compared to $\lambda_{Bi} = 1.25$ eV from Ref. [181]. We present the band structure from first principles with the Wannier bands overlain with and without SOC in Figure 4.5.

We add the magnetic field as a Zeeman term $H_Z = g\mu_B(\vec{L} + 2\vec{S}) \cdot \vec{B}$. The magnetic field strength used in the rest of this work is 25 meV, which results in a splitting of the $m_j = \frac{1}{2}$ conduction band by ≈ 33 meV. The corresponding magnetic field strength (T) in topological

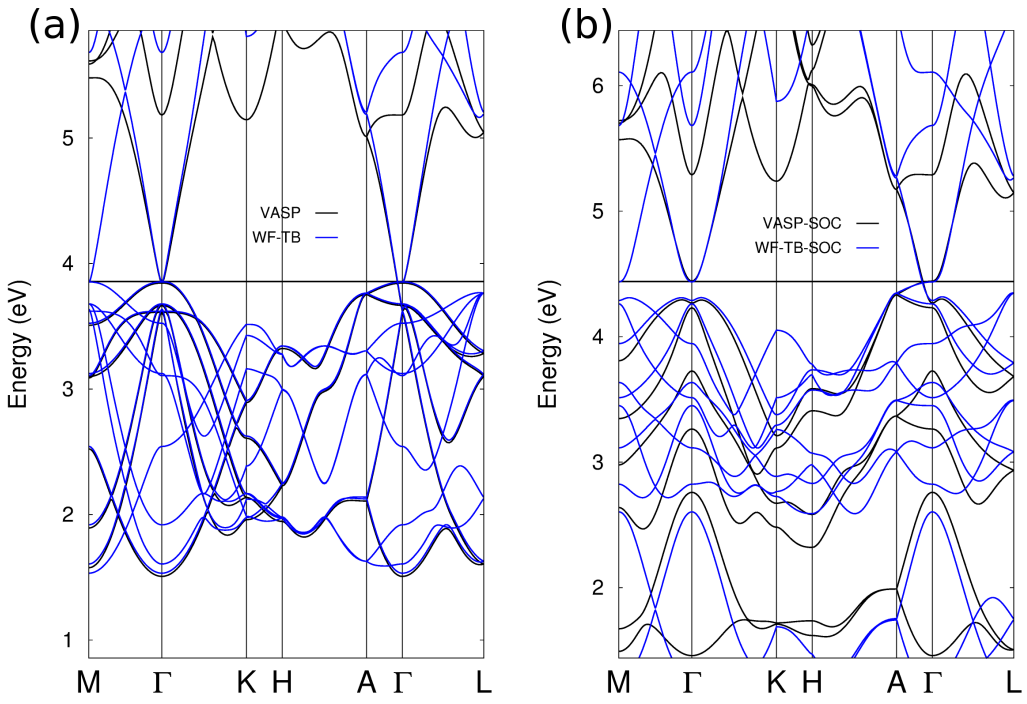

Figure 4.5: Band structure of bulk Na_3Bi using the $(1\bar{2}0)$ cell. (a) Comparison of the bulk band structure without SOC of Na_3Bi using the $(1\bar{2}0)$ cell calculated with VASP versus with the WF-TB Hamiltonian. (b) Likewise with SOC. In both cases the band-folding is apparent, especially where the $(1\bar{2}0)$-BZ ends halfway along MΓ.

Dirac semimetals depends on the effective g-factor in these materials. For Na_3Bi, $g \approx 20$ [143] and in Cd_3As_2 $g \approx 40$ [182]. However, there are not experimental estimates for g_p for the p-orbitals.

4.5 Discussion

4.5.1 Finite-size Slab

As an extra check of our tight-binding Hamiltonian, we create a finite-size slab as well as a slab with an applied band bending potential at one surface to mimic asymmetric charge transfer, as investigated in Chapter 3. In this subsection, there is no applied magnetic field.

Figure 4.7 compares our tight-binding result for a 10.9 nm thick slab and the DFT result for the same. Notice that the Dirac point at Γ appears lower in energy for WF-TB, nearly at the top of the bulk valence band, compared to DFT. This is in agreement with Ref. [152]. There

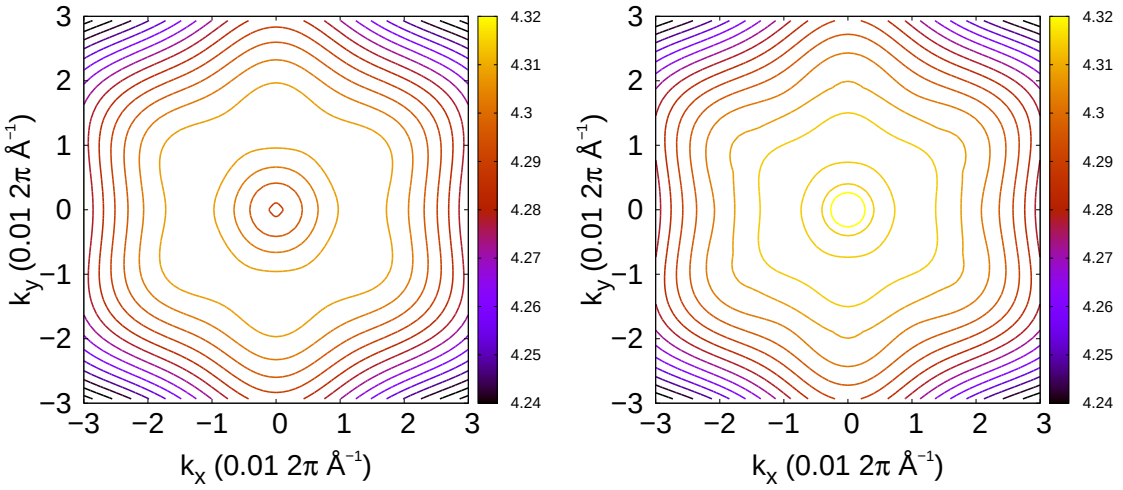

Figure 4.6: Constant energy contours with and without an applied magnetic field. (a) Constant energy contours of the top valence band in the k_z=0 plane as calculated from the WF-TB model for the $(1\bar{2}0)$ cell in the absence of the magnetic field. (b) Constant energy contours of the top valence band in the k_z=0 plane as calculated from the WF-TB model of the $(1\bar{2}0)$ cell with an applied magnetic field of 25 meV, exhibiting the hexagonal symmetry. In both panels, SOC is included and the colorscale is for the energy (eV).

is also substantially reduced surface character along $\bar{Z}\Gamma$ except for a couple of momenta; this feature disappears for thicker slabs, recovering the surface state character of those bands in the region between Γ and the projection of the bulk Dirac node.

We then apply an exponentially decaying band bending potential to the top surface, given by

$$V = V_0 e^{-z/\eta}, \tag{4.5}$$

with z measured positively into the slab from the top surface, and V_0 = -30 meV and η = 1 nm to match the order of magnitude of our parameters in [139]. See also μ in Table 3.1 and the decay length in Fig. 3.13(b).

We compare our tight-binding result and the DFT result in the case of asymmetric charge transfer amounting to 0.073 electrons per unit cell area (0.0008 e/$\mathring{A}^2$). The band structures are presented in Fig. 4.8. As in the pristine case, the WF-TB Dirac point at Γ occurs just above the bulk valence band, but now the top-surface Dirac cone is driven deep into the bulk valence band. A crossing between the two lowest conduction bands develops at the projection of the Dirac node along the rotational axis, and we see at this level of charge transfer that the lowest quantum well states develop a slight top-surface character and also start to shift

down in energy. All of these qualitative features are present in the DFT-calculated result.

Likewise, we compare the constant energy contours (CECs) of our tight-binding result with the DFT result at the energy of the Dirac node in Fig. 4.9. The top-surface Fermi arcs expand into the BZ and connect to the projection of the Dirac node on the surface. The bottom-surface Fermi arcs are unchanged since the charge transfer occurs at the opposite surface. The Fermi arcs have weaker surface character, blending into the bulk, at the Dirac node projection. The qualitative features of the DFT result are strongly reproduced by our TB model and add further credence to the validity of the TB model, even without MLWFs and in a non-primitive unit cell.

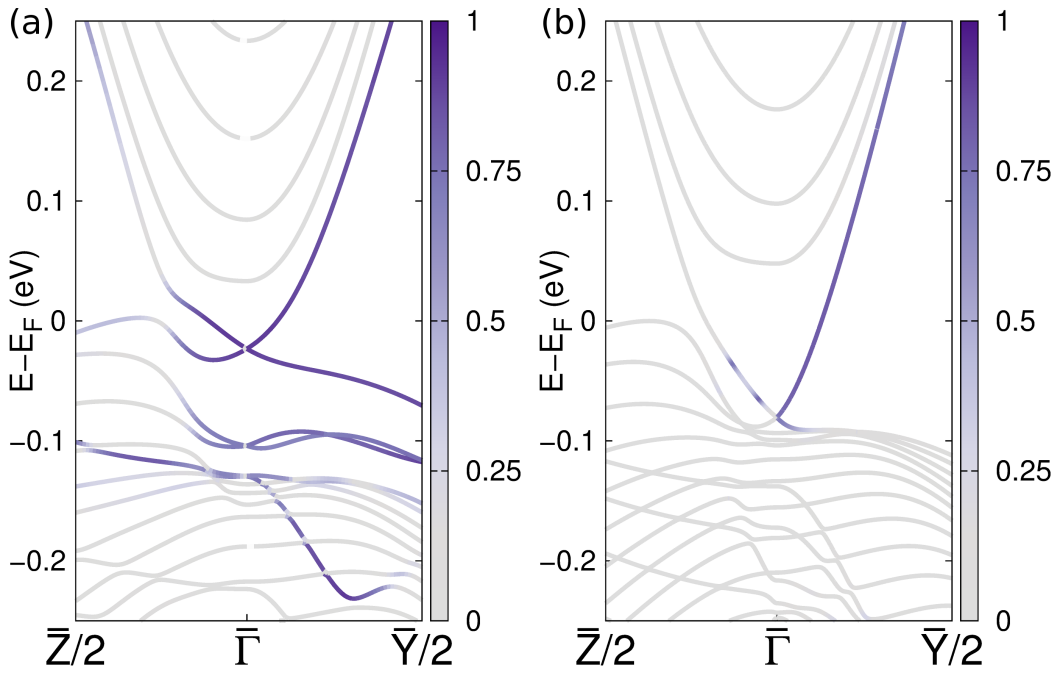

Figure 4.7: Slab band structures. (a) Band structure of the pristine, inversion-symmetric 10.9 nm thick $(1\bar{2}0)$ slab from DFT [139]. (b) Band structure of the same slab from the WF tight-binding Hamiltonian. The color scale represents the surface state character with values closer to unity indicating localization on the top or bottom surface.

4.5.2 Splitting Dirac Nodes via Magnetic Field

We apply a magnetic field along the rotational axis (c-axis) of Na_3Bi. We find that each Dirac node splits into two single Weyl nodes and two double Weyl nodes along the rotational axis. Their positions and energies are listed in Table 4.3. The bands forming the single Weyl nodes disperse linearly in all directions around the Weyl node, and for the double Weyl node

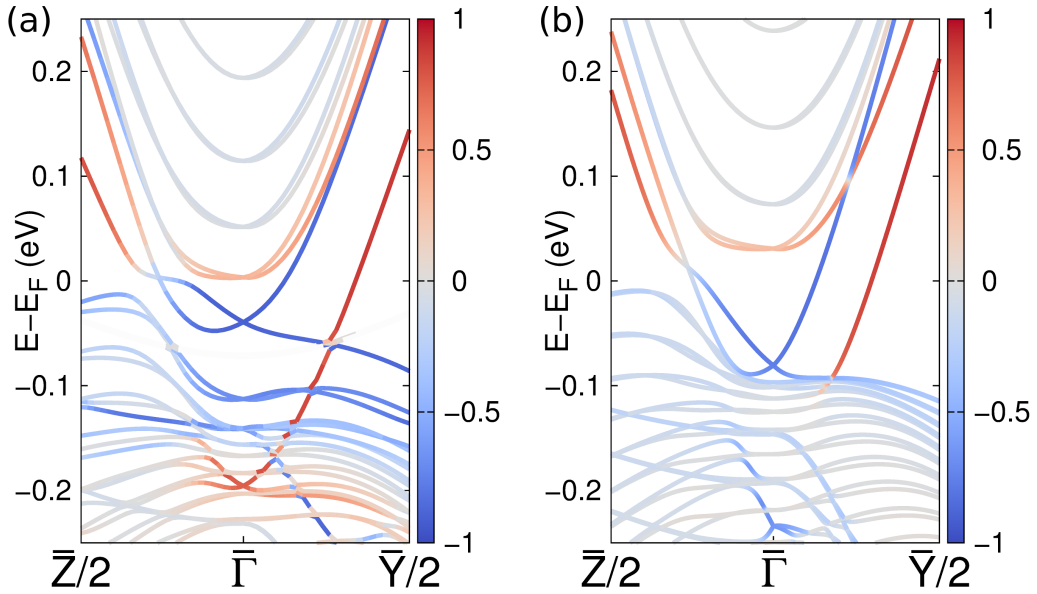

Figure 4.8: Slab band structures with band bending potential. (a) Band structure of the 10.9 nm thick $(1\bar{2}0)$ slab with asymmetric charge transfer to the top surface from DFT [139]. (b) Band structure of the same slab from the WF tight-binding Hamiltonian. The red (blue) color scale represents the surface state character with values closer to +1 (-1) indicating localization on the top (bottom) surface.

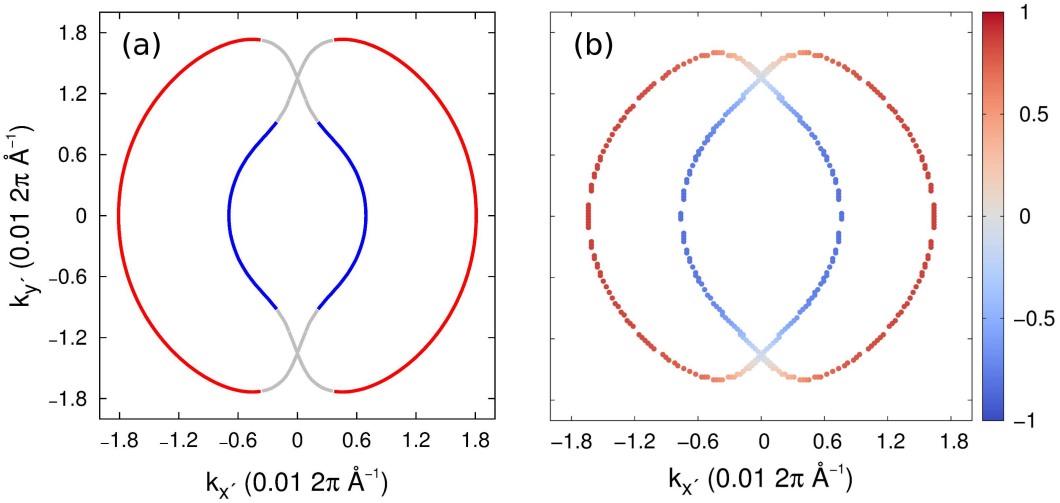

Figure 4.9: Constant energy contours in the slab model with band bending potential. (a) Constant energy contours at the energy of the band crossing point at the projection of the Dirac node from [139]. (b) Constant energy contours from the WF-TB model for the 10.9 nm thick slab with band bending potential; the surface state character is denoted by the colorscale as in Figure 4.8.

they disperse linearly along the z-axis and quadratically in the xy-plane. We determine the chiral charge of the Weyl nodes by enclosing each in spheres of successively smaller radius and calculating their Chern numbers (Berry curvature flux),

$$\chi_n = \frac{1}{2\pi} \oint_S dS \; \hat{\boldsymbol{n}} \cdot \boldsymbol{\Omega}_n(\boldsymbol{k}). \tag{4.6}$$

S is the two-dimensional surface of the sphere, or, as relevant later, S_n is the FS sheet of band n. The Berry curvature vector fields for the single and double WNs are shown in Figure 4.11. Discussion of how this surface integral is performed, plus sample code, is available in Appendix A.2.

There are four Weyl nodes in the $z > 0$ half-BZ which we can consider as two pairs (each pair consisting of a single and a double Weyl node): one pair has negative chirality and is higher in energy, and the other pair has positive chirality and is lower in energy. Fig 4.10 shows the band structure along the rotation axis in the half-BZ, and the development of the four Weyl nodes as discussed in Ref. [175]. Each Weyl node is the result of a crossing of bands with different rotational eigenvalues, as was the Dirac node in the absence of the magnetic field. Each pair shares a $|j_z| = \frac{3}{2}$ band and is separated by only ≈ 2 meV. Whereas Refs. [160, 176] considered what Fermi arcs arise in an exchange field in Na_3Bi, they considered only the pairs of single Weyl nodes. Here we examine the Fermi arcs and other surface states which arise from the magnetically-induced single *and* double Weyl nodes.

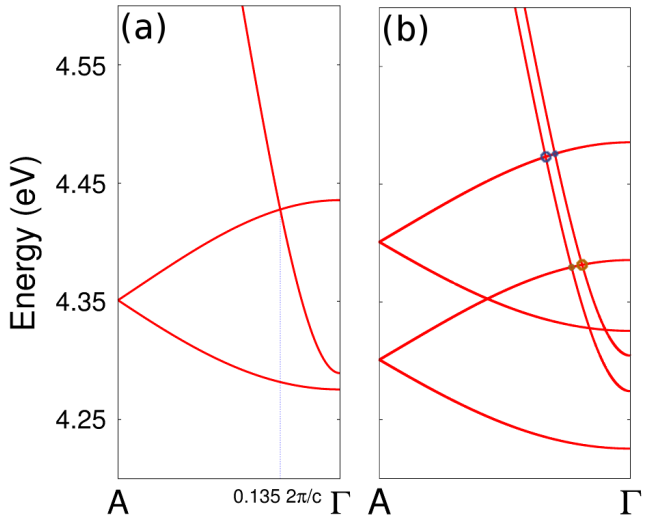

Figure 4.10: (a) Band structure of Na_3Bi along the rotation axis. The position of the Dirac node is emphasized. (b) Band structure of Na_3Bi along the rotation axis in the presence of a magnetic field of 25 meV. The positive (negative) chirality Weyl nodes are noted in orange (blue) circles, with the small (large) circles meaning Chern numbers of ± 1 (± 2).

Table 4.3: Chern numbers, momenta, and energies with respect to the Fermi level of the four Weyl nodes in the $z > 0$ half-Brillouin zone. The band index is listed for use in Equation 4.7.

$W_{n,\alpha}$	χ_n	k_z ($\mathring{A}^{-1}$)	Energy (meV)
$W_{24,a}$	-2	0.10973	33.3
W_{25}	-1	0.09779	35.8
W_{23}	+1	0.07618	-60.4
$W_{24,b}$	+2	0.06237	-58.5

4.5.3 Fermi Surface Chern Numbers and Fermi Arcs

Following Gosálbez-Martínez *et al.* [179], we examine the Chern numbers of disjoint FS sheets at different chemical potentials around the magnetically-induced Weyl nodes. Figure 4.12 shows the band structure in the presence of the magnetic field and the projection of the bulk FS at different chemical potentials. The Chern number, C_n, of each FS sheet (S_n, the boundary of the volume $\mathcal{V}$) arising from band n is given by

$$C_n = \sum_{W_{n,\alpha} \in \mathcal{V}} \chi_{n,\alpha} - \sum_{W_{n-1,\alpha} \in \mathcal{V}} \chi_{n-1,\alpha} \tag{4.7}$$

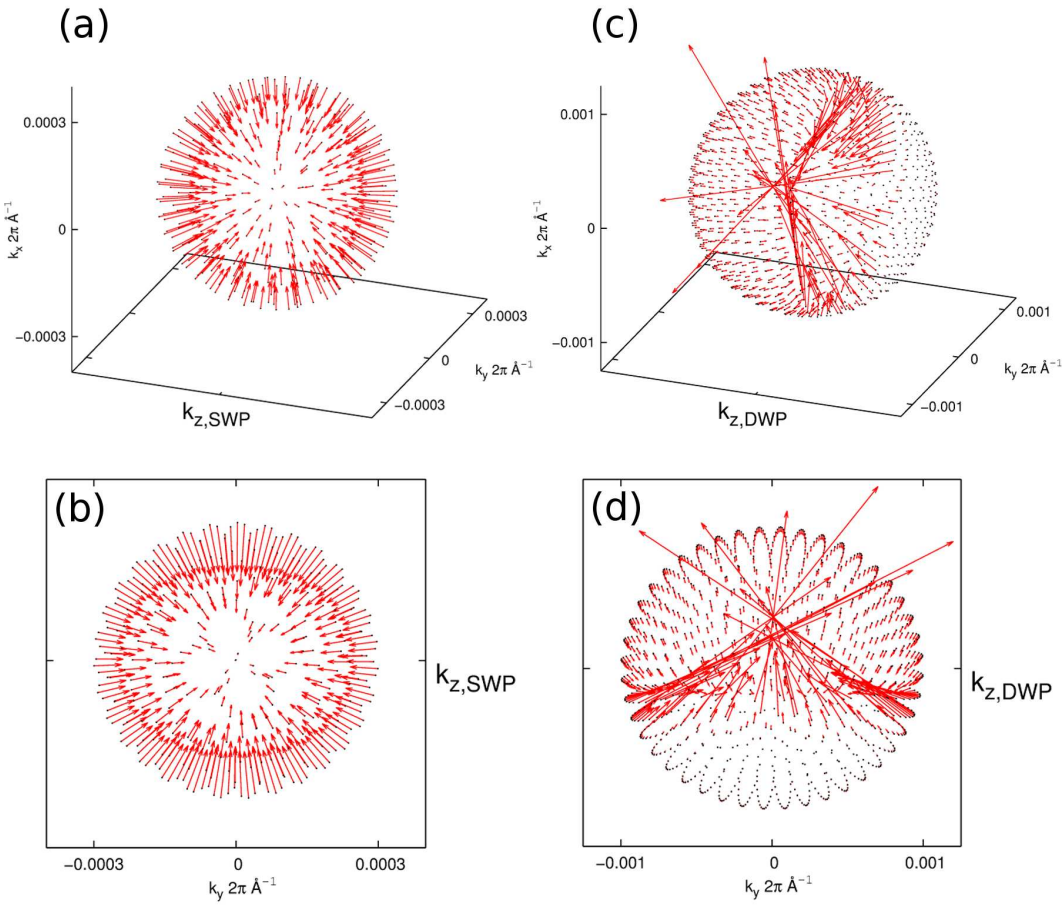

Figure 4.11: (a) Berry curvature in the vicinity of a single Weyl node (SWP) with chiral charge of -1. The "anti-hedgehog" monopole shape is apparent. (b) Projection of the SWP Berry curvature into the k_x=0 plane. (c) Berry curvature in the vicinity of a double Weyl node (DWP) with chiral charge of -2. The "anti-hedgehog" shape is quite different, with almost all of the Berry curvature arising on a chord of the sphere. (d) Projection of the Berry curvature into the k_x=0 plane, showing the chord which is almost along the equator of the sphere.

where $\chi_{n,\alpha}$ is the chirality of the α^{th} Weyl node connecting bands n and $n+1$, $W_{n,\alpha}$. The sum is over all Weyl nodes interior to the FS sheet; the outward pointing normal vector points toward the exterior of the FS for electron-pockets and the reverse for hole-pockets. It is a source of Berry flux in the lower band (n) and a sink of Berry flux in the upper band ($n+1$).

Figure 4.12(a) locates all of the magnetically-induced Weyl nodes along the rotational axis and colors bands 22 through 26 as they will be referenced in the foregoing section. Table 4.4 lists the Fermi surface Chern numbers of each Fermi sheet belonging to each band. At each choice of chemical potential we identify the Fermi surface Chern numbers and describe the resulting Fermi arcs and surface states.

Table 4.4: C_n for each Fermi surface sheet, S_n as a function of chemical potential (meV). Only Fermi surface sheets appearing in the $z > 0$ half-BZ are listed.

S_n	E_1=+40	E_2=+10	E_3=-20	E_4=-50	E_5=-65
26	+1	-	-	-	-
25	0	0	0	0	-
24	-	+2	+2	0	0
23	-	-	-	0	-1

At $E = E_1$ [Fig. 4.12(b)], we see a small electron-pocket ellipsoid (brown, deriving from band 26) which encloses negative and positive chirality single Weyl nodes from bands 25 and 23, respectively. Only the negative Weyl node (W_{25}) enters into Equation 4.7 and the FS inherits a Chern number of +1. For the other electron-pocket ellipsoid (green, deriving from band 25), every Weyl node *and its partner in the other half of the BZ* is enclosed and its FS Chern number is zero [see Fig. 4.14(b)]. This is alternatively understood from the fact that S_{25} encloses the parity-invariant Γ point, so its Chern number must be zero. We might expect one Fermi arc per surface terminating on S_{26} and zero terminating on S_{25}. However, Haldane [187] points out that Fermi arcs arising from Weyl nodes lower in energy may still be observed away from the energy of the Weyl node, so long as they terminate tangentially and respect the Chern number of the Fermi surface; i.e. for $C_{25} = 0$, such a state would have to originate from and terminate on the same surface. We show the surface Green's function for the same energy in Figure 4.13(b). Indeed, there is a single Fermi arc terminating on S_{26}, and there is a single Fermi arc which originates from and terminates on S_{25} [as seen in the wider view of Fig. 4.14].

At $E = E_2$ [Fig. 4.12(c)], the analysis for S_{25} does not change, and the hole-pocket S_{24} (magenta, deriving from band 24) encloses the double Weyl node $W_{24,a}$ (yielding $C_{24} = +2$). Accordingly we expect two Fermi arcs to connect S_{24} and its mirror partner. The data show instead two Fermi arcs connecting to S_{25} [see Fig. 4.13(c)]. This is acceptable because while the Fermi arcs terminate on S_{24} and originate from S_{25}, in the other half of the BZ there is a pair related by mirror symmetry which originates on S'_{24} (the mirror partner) and terminates on S_{25}.

At $E = E_3$ [Fig. 4.12(d)], the analysis is much the same as at the preceding energy except that the hole-pocket encloses an extra Weyl node (W_{25}). The extra Weyl node connects bands with indices which are irrelevant for the calculation of the hole-pocket Chern number (C_{24}), so the same result obtains. Fig. 4.14(a) provides a zoom-in view of the two Fermi arcs, which is qualitatively the same for $E = E_2$ and $E = E_4$, discussed next. The Fermi arcs connect the Fermi surface sheets tangentially.

At $E = E_4$ [Fig. 4.12(e)], S_{25} extends all the way across the BZ as it has at the previous energies [see also Fig. 4.14(e)], so it has a zero Chern number. As has been the case previously, but only necessary to discuss now, S_{24} (magneta) is roughly ellipsoidal except for a "crumpled-nosecone" shape near where it avoids S_{25}. The Weyl node W_{23} is actually *exterior to* S_{24}, and so the Fermi surface Chern numbers might have been the same as at the previous energy. However, S_{24} also has elongated to cross the BZ boundary, enclosing the A point, and thus it has a zero Chern number. Again we see the two Fermi arcs which connect these two Fermi surface sheets, but now we note that the other surface states have connected through S_{25}, forming a closed loop in the BZ which is similar to the surface states of topological insulators in applied in-plane magnetic fields [185, 186]. Also there appears a short whisker of a surface state which forms off of the "crumpled-nosecone" of S_{24} and is lost into the projected bulk states.

At $E = E_5$ [Fig. 4.12(f)], we are below the energies of the Weyl nodes. In dark blue, the hole-pocket S_{23} encloses only W_{23}, so $C_{23} = -1$. In magenta, S_{24} is a hole-pocket which reaches all the way across the the BZ again, enclosing the parity-invariant point A (not shown) and also all of the Weyl nodes and their partners, so $C_{24} = 0$. The whisker surface state is identified as the Fermi arc. The TI-like closed surface state can be seen in Fig. 4.14(f) and does not connect any bulk Fermi surface sheets.

4.6 Conclusion

In summary, we have developed a Wannier-function-based tight-binding model for the topological Dirac semimetal, Na_3Bi, which reproduces the DFT-calculated band structure well while preserving the symmetries of the crystal. The Wannier functions are atom-centered with larger spread than maximally localized WFs. Atomic-like SOC was included, and we investigated the splitting of the Dirac nodes into multiple Weyl nodes in an applied magnetic field. We found that each Dirac node splits into pairs of Weyl nodes with charges ± 1 and ± 2. By carefully considering the Chern number of associated Fermi surface sheets, we detailed the interesting development of Fermi arc and other topological surface states as a function of chemical potential consistent with the topological charges of the Weyl nodes. Our tight-binding model can be used to calculate novel properties induced by the nonzero Berry curvature, and its qualitative features can be applied in another experimentally observed topological DSM, Cd_3As_2.

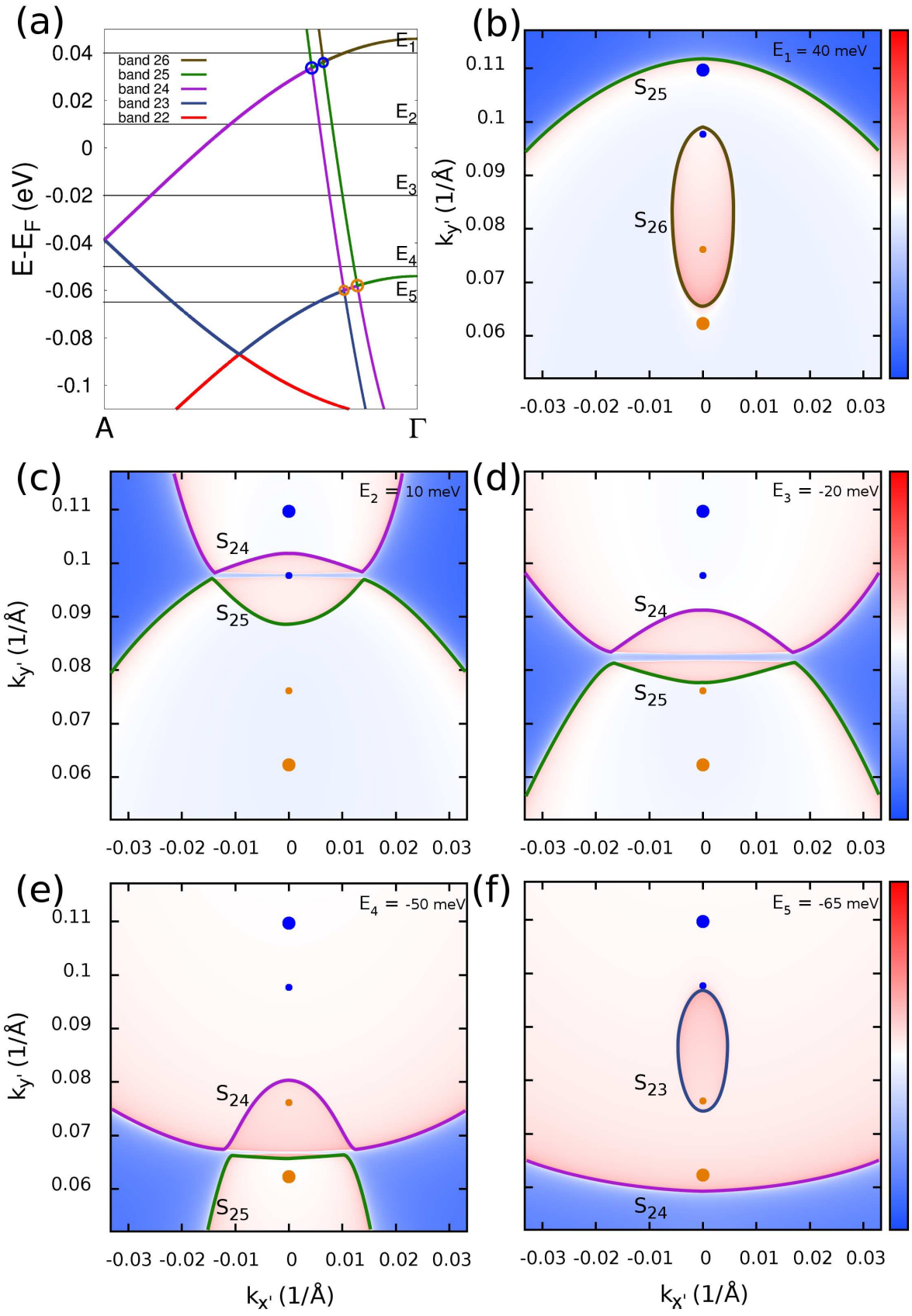

Figure 4.12: (Caption on page 94.)

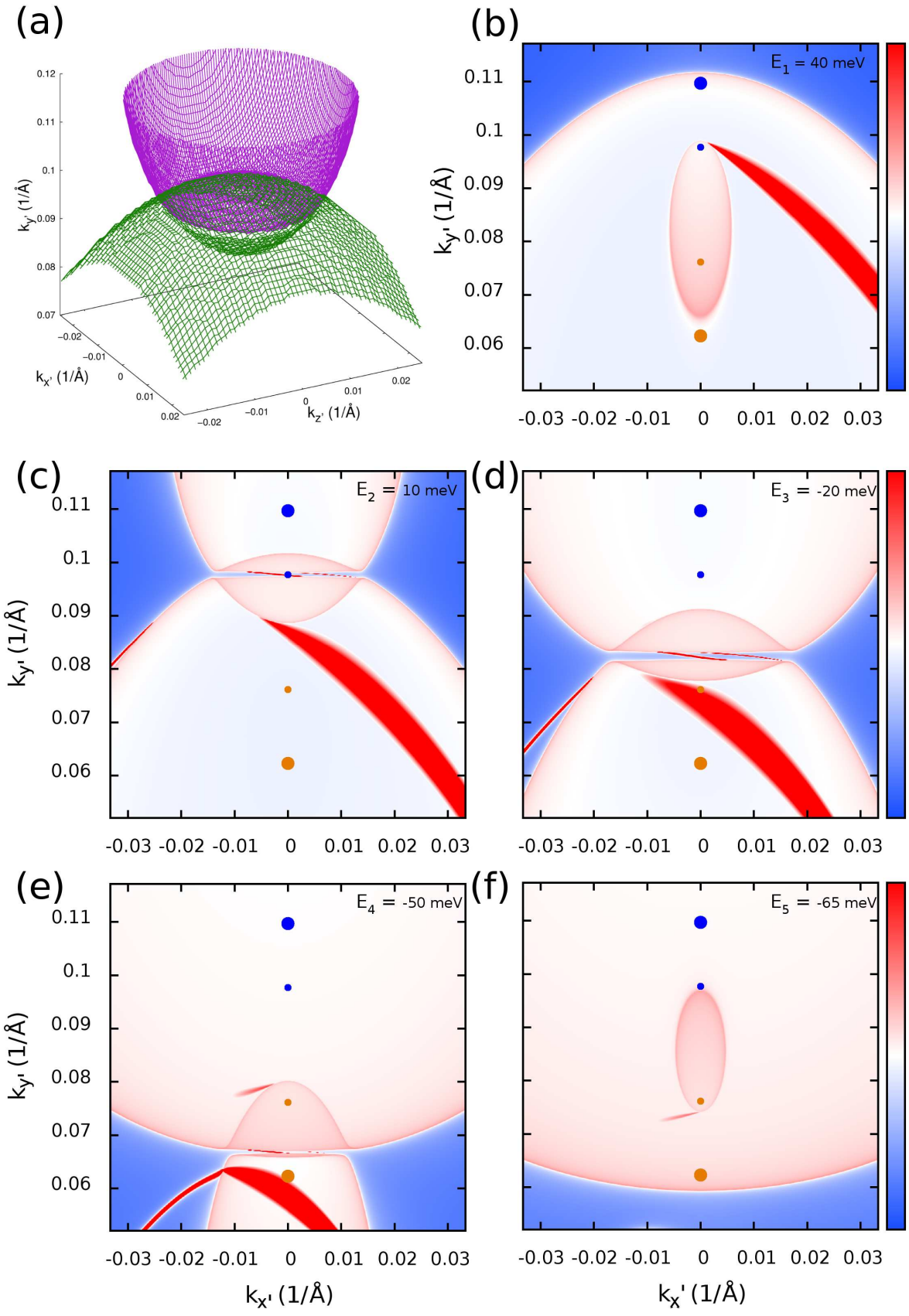

Figure 4.13: (Caption on page 94.)

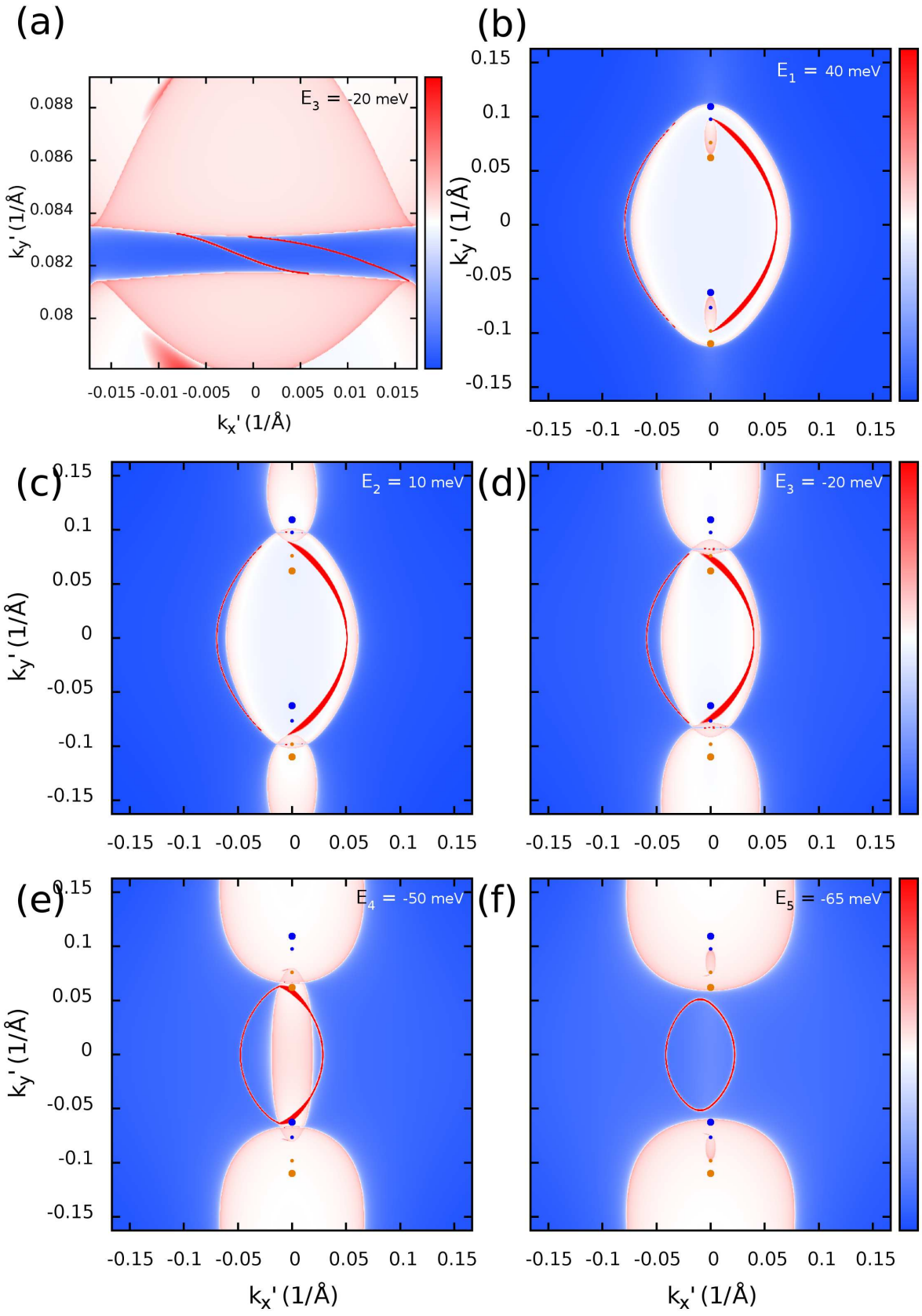

Figure 4.14: (Caption on page 94.)

Figure 4.12: Bulk Fermi surface sheets in an applied magnetic field. (a) Band structure of Na_3Bi with an applied magnetic field of 25 meV. Single and double Weyl nodes are emphasized with smaller and larger open circles, respectively. The colors of the bands correspond to the subsequent panels, and the marked energies correspond to the subsequent panels in descending order. All energies are relative to the Fermi level. (b-f) Bulk fermi surface projection onto the $(1\bar{2}0)$ plane, magnified near to the Weyl nodes at energies $E_1 - E_5$ respectively, which are +40, +10, -20, -50 and -65 meV. The colorscale is a logscale for the spectral density of the bulk Green's function, with blue being negligible weight and red being substantial weight.

Figure 4.13: Fermi arcs in an applied magnetic field. (a) Bulk Fermi surface of Na_3Bi with an applied magnetic field of 25 meV at an energy of +10 meV relative to the Fermi level. The three-dimensional "crumpled-nosecone" of bands 24 (magenta) and 25 (green) is apparent. (b-f) Fermi arcs on the $(1\bar{2}0)$ surface, magnified near to the Weyl nodes at energies $E_1 - E_5$ respectively, which are +40, +10, -20, -50 and -65 meV. The colorscale is a chimera of the spectral densities of the bulk and surface Green's functions: significant weight of the bulk Green's function appears white or light red, and weight on the Fermi arc surface states appears as strictly the darkest red. This makes it apparent that many of the surface states attach tangentially to the bulk Fermi surface.

Figure 4.14: Fermi arcs and surface states in a wider view of the Brillouin zone. (a) Zoom-in on the two Fermi arc states at E_3= -20 meV connecting C_{24}=+2 and C_{25}=0 Fermi surface sheets. (b-f) Fermi arcs and other surface states on the $(1\bar{2}0)$ in an area one quarter of the full BZ area. The panels show $E_1 - E_5$ respectively, which are +40, +10, -20, -50 and -65 meV. The colorscale is a chimera of the spectral densities of the bulk and surface Green's functions: significant weight of the bulk Green's function appears white or light red, and weight on the Fermi arc surface states appears as strictly the darkest red. This makes it apparent that many of the surface states attach tangentially to the bulk Fermi surface, and at low enough energy the surface states are disconnected from the bulk Fermi surface.

Chapter 5

Conclusion

This dissertation has endeavored to emphasize and demonstrate the rich, promising, and expansive research into topological materials. Density functional theory is among the most powerful tools to predict, model, and further characterize future topological systems in condensed matter physics. As mentioned throughout, there is still a large frontier to be explored, particularly for experimental confirmation of an avalanche of materials which are predicted to host topological states.

In Chapter 2, we used DFT to construct side-surfaces of the topological insulator Bi_2Se_3. We detailed a qualitative discrepancy between our findings and the results of the model Hamiltonian approach. Importantly, the effects of the side surface symmetries and surface reconstruction were included in our DFT calculations, in contrast to the effective model Hamiltonian approach based on linear and quadratic terms in momentum. Further, the model Hamiltonian is effective only very near to Γ for surfaces which contain a mirror axis, whereas our DFT treatment naturally takes into account all of the surface symmetries even without a mirror axis. We found that the spin and spin-orbital textures of the Dirac cones for the two different surfaces differ from each other and from those for the easy-cleaving (111) surface. Interestingly, the $(1\bar{1}0)$ surface showed a combination of Rashba- and Dresselhaus-like spin texture, and there exists spin-momentum-locking, just not orthogonal spin-momentum-locking. For the $(1\bar{2}0)$ surface showed Rashba- and Dresselhaus-like spin texture near to the Γ point only, and Dresselhaus-like spin texture near the Y point. These are important differences that one must consider if the topological surface state on the side surface is to be exploited for spintronic or other purposes.

In Chapter 3, we used DFT to construct thin films of a topological Dirac semimetal Na_3Bi and investigated the topological bulk and surface properties in the presence of asymmetric charge transfer. Though we simulated K- or Na-adsorbed films for the $(1\bar{2}0)$ surface, the amount of charge transfer is the relevant variable, and we found that gapless crossing are induced at exactly the projection of the 3D Dirac node despite the existence of the band gap in the bulk. The topological states on the top- and bottom-surfaces are separated by the

charge transfer, yet are pinned by the projections of the topologically robust 3D Dirac nodes. We showed that the constant-energy-contours and spin textures at the band crossing energy can be modified by varying the amount of charge transfer, and the qualitative features of our findings can be applied to other topological Dirac semimetals. This kind of asymmetric charge transfer can be expected at interfaces of heterostructures involving Dirac semimetals, and will be relevant for future devices composed of such heterostructures.

In Chapter 4, we developed a Wannier-function-based tight-binding model for the topological Dirac semimetal Na_3Bi from ab initio DFT calculations. The Wannier functions are atom-centered even though they are not maximally localized, and the tight-binding model reproduces the DFT-calculated band structure well while preserving the symmetries of the cyrstal. We applied a magnetic field and found that each Dirac node splits into multiple Weyl nodes: one pair with Chern numbers of ± 1 and a second pair with Chern numbers of ± 2. By carefully considering the Chern number of associated Fermi surface sheets, we detailed the interesting development of Fermi arc and other topological surface states as a function of chemical potential consistent with the topological charges of the Weyl nodes. The existence of the double Weyl nodes with Chern number ± 2 confirms the significance of cubic bulk-symmetry-respecting terms in the low energy $\mathbf{k} \cdot \mathbf{p}$ model Hamiltonian. Our tight-binding model can be used to calculate the novel transport properties induced by nonzero Berry curvature (e.g. anomalous Nernst response), and its qualitative features can be applied to other topological Dirac semimetals, such as Cd_3As_2.

References

[1] P. A. M. Dirac, Proc. R. Soc. Lond. A **123**, 714-733 (1929).

[2] A. Pribram-Jones, D. A. Gross, and K. Burke, Ann. Rev. Phys. Chem. **66**, 283-304 (2015).

[3] P. Hohenberg and W. Kohn, Phys. Rev. **136**, B864 (1964).

[4] W. Kohn and L. J. Sham, Phys. Rev. **140**, A1133 (1965).

[5] J. P. Perdew and Y. Wang, Phys. Rev. B **45**, 13244 (1992).

[6] J. P. Perdew, J. A. Chevary, S. H. Vosko, K. A. Jackson, M. R. Pederson, D. J. Singh, and C. Fiolhais, Phys. Rev. B **46**, 6671 (1992).

[7] J. P. Perdew, K. Burke, and M. Ernzerhof, Phys. Rev. Lett. **77**, 3865 (1996).

[8] D. Vanderbilt, Phys. Rev. B **41**, 7892(R) (1990).

[9] K. Laasonen, R. Car, C. Lee, and D. Vanderbilt, Phys. Rev. B **43**, 6796(R) (1991).

[10] D. R. Hamann, M. Schlüter, and C. Chiang, Phys. Rev. Lett. **43**, 1494 (1979).

[11] P. E. Blöchl, Phys. Rev. B. **50**, 17953 (1994).

[12] J. Hafner, J. Comput. Chem. **29**, 2044-2078 (2008).

[13] D. D. Koelling and B. N. Harmon, J. Phys. C: Solid State Phys. **10**, 3107 (1977).

[14] L. Kleinman, Phys. Rev. B **21**, 2630 (1980).

[15] G. B. Bachelet and M. Schlüter, Phys. Rev. B **25**, 2103 (1982).

[16] N. Marzari, A. A. Mostofi, J. R. Yates, I. Souza, and D. Vanderbilt, Rev. Mod. Phys. **84**, 1419 (2012).

[17] N. Marzari and D. Vanderbilt, Phys. Rev. B **56**, 12847 (1997).

[18] I. Souza, N. Marzari, and D. Vanderbilt, Phys. Rev. B **65**, 035109 (2001).

[19] A. A. Mostofi, J. R. Yates, G. Pizzi, Y. S. Lee, I. Souza, D. Vanderbilt, and N. Marzari, Comput. Phys. Commun. **185**, 2309 (2014).

[20] R. Sakuma, Phys. Rev. B **87**, 235109 (2013).

[21] R. Wang, E. A. Lazar, H. Park, A. J. Millis, and C. A. Marianetti, Phys. Rev. B **90**, 165125 (2014).

[22] D. J. Thouless, J. Phys. C: Solid State Phys. **17**, 325-327 (1984).

[23] T. Thonhauser and D. Vanderbilt, Phys. Rev. B **74**, 235111 (2006).

[24] A. A. Soluyanov and D. Vanderbilt, Phys. Rev. B **83**, 035108 (2011).

[25] G. W. Winkler, A. A. Soluyanov, and M. Troyer, Phys. Rev. B **93**, 035453 (2016).

[26] J. I. Mustafa, S. Coh, M. L. Cohen, and S. G. Louie, Phys. Rev. B **94**, 125151 (2016).

[27] J. Jung and A. H. MacDonald, Phys. Rev. B **87**, 195450 (2013).

[28] S. Fang, R. K. Defo, S. N. Shirodkar, S. Lieu, G. A. Tritsaris, and E. Kaxiras, Phys. Rev. B **92**, 205108 (2015).

[29] M. Z. Hasan and C. L. Kane, Rev. Mod. Phys. **82**, 3045 (2010).

[30] X.-L. Qi and S.-C. Zhang, Rev. Mod. Phys. **83**, 1057 (2011).

[31] J. E. Moore, Nature **464**, 194-198 (2010).

[32] Y. Ando, J. Phys. Soc. Jpn. **82**, 102001 (2013).

[33] L. Fu, C. L. Kane, and E. J. Mele, Phys. Rev. Lett. **98**, 106803 (2007).

[34] R. Roy, Phys. Rev. B **79**, 195322 (2009).

[35] K. v. Klitzing, G. Dorda, and M. Pepper, Phys. Rev. Lett. **45**, 494-497 (1980).

[36] R. B. Laughlin, Phys. Rev. B **23**, 5632-5633 (1981).

[37] D. J. Thouless, M. Kohmoto, M. P. Nightingale, and M. d. Nijs, Phys. Rev. Lett. **49**, 405-408 (1982).

[38] I. Garate and M. Franz, Phys. Rev. Lett. **104**, 146802 (2010).

[39] A. A. Burkov and D. G. Hawthorn, Phys. Rev. Lett. **105**, 066802 (2010).

[40] F. Mahfouzi, N. Nagaosa, and B. K. Nikolić, Phys. Rev. Lett. **109**, 166602 (2012).

[41] F. Mahfouzi, J. Fabian, N. Nagaosa, and B. K. Nikolić, Phys. Rev. B **85**, 054406 (2012).

[42] M. Rodriguez-Vega, G. Schwiete, and E. Rossi, Phys. Rev. B **96**, 235419 (2017).

[43] A. R. Mellnick, J. S. Lee, A. Richardella, J. L. Grab, P. J. Mintun, M. H. Fischer, A. Vaezi, A. Manchon, E.-A. Kim, N. Samarth, and D. C. Ralph, Nature **511**, 449-451 (2014).

[44] Y. Fan, P. Upadhyaya, X. Kou, M. Lang, S. Takei, Z. Wang, J. Tang, L. He, L.-T. Chang, M. Montazeri, G. Yu, W. Jiang, T. Nie, R. N. Schwartz, Y. Tserkovnyak, and K. L. Wang, Nat. Mat. **13**, 699-704 (2014).

[45] P. B. Ndiaye, C. A. Akosa, M. H. Fischer, A. Vaezi, E.-A. Kim, and A. Manchon, Phys. Rev. B **96**, 014408 (2017).

[46] Y. Wang, D. Zhu, Y. Wu, Y. Yang, J. Yu, R. Ramaswamy, R. Mishra, S. Shi, M. Elyasi, K.-L. Teo, Y. Wu, and H. Yang, Nat. Commun. **8**, 1364 (2017).

[47] L. Fu and C. L. Kane, Phys. Rev. Lett. **102**, 216403 (2009).

[48] T. Yokoyama, Phys. Rev. B **86**, 075410 (2012).

[49] A. R. Akhmerov, J. Nilsson, and C. W. J. Beenakker, Phys. Rev. Lett. **102**, 216404 (2009).

[50] Y. Tanaka, T. Yokoyama, and N. Nagaosa, Phys. Rev. Lett. **103**, 107002 (2009).

[51] A. A. Burkov and L. Balents, Phys. Rev. Lett. **107**, 127205 (2011).

[52] L. Fu and C. L. Kane, Phys. Rev. B **76**, 045302 (2007).

[53] B. Zumino, J. Math. Phys. **3**, 1055 (1962).

[54] J. E. Moore and L. Balents, Phys. Rev. B **75** 121306(R) (2007).

[55] D. Hsieh, D. Qian, L. Wray, Y. Xia, Y. S. Hor, R. J. Cava, and M. Z. Hasan, Nature **452**, 970-974 (2008).

[56] Y. Xia, D. Qian, D. Hsieh, L. Wray, A. Pal, H. Lin, A. Bansil, D. Grauer, Y. S. Hor, R. J. Cava, and M. Z. Hasan, Nat. Phys. **5**, 398-402 (2009).

[57] H.-J. Noh, H. Koh, S.-J. Oh, J.-H. Park, H.-D. Kim, J. D. Rameau, T. Valla, T. E. Kidd, P. D. Johnson, Y. Hu, and Q. Li, Europhys. Lett. **81** 57006 (2008).

[58] J. C. Y. Teo, L. Fu, and C. L. Kane, Phys. Rev. B **78**, 045426 (2008).

[59] H. Zhang, C.-X. Liu, X.-L. Qi, X. Dai, Z. Fang, and S.-C. Zhang, Nature Phys. **5**, 438 (2009).

[60] C.-X. Liu, X.-L. Qi, H. Zhang, X. Dai, Z. Fang, and S.-C. Zhang, Phys. Rev. B **82**, 045122 (2010).

[61] L. C. Lew Yan Voon and M. Willatzen, Method of Invariants in: *The $k \cdot p$ Method*, (Springer, Berlin, Heidelberg 2009).

[62] L. Fu, Phys. Rev. Lett. **103**, 266801 (2009).

[63] H. Weyl, Proc. Natl. Acad. Sci. U.S.A. **15**, 323 (1929).

[64] X. Wan, A. M. Turner, A. Vishwanath, and S. Y. Savrasov, Phys. Rev. B **83**, 205101 (2011).

[65] S.-Y. Xu, I. Belopolski, N. Alidoust, M. Neupane, G. Bian, C. Zhang, R. Sankar, G. Chang, Z. Yuan, C.-C. Lee, S.-M. Huang, H. Zheng, J. Ma, D. S. Sanchez, B. Wang, A. Bansil, F. Chou, P. P. Shibayev, H. Lin, S. Jia, and M. Z. Hasan, Science **349**, 613-617 (2015).

[66] B. Q. Lv, H. M. Weng, B. B. Fu, X. P. Wang, H. Miao, J. Ma, P. Richard, X. C. Huang, L. X. Zhao, G. F. Chen, Z. Fang, X. Dai, T. Qian, and H. Ding, Phys. Rev. X **5**, 031013 (2015).

[67] H. B. Nielsen and M. Ninomiya, Phys. Lett. B **130**, 389-396 (1983).

[68] A. A. Soluyanov, D. Gresch, Z. Wang, Q. S. Wu, M. Troyer, X. Dai, and B. A. Bernevig, Nature **527**, 495-498 (2015).

[69] S. L. Adler, Phys. Rev. **177**, 2426 (1969).

[70] J. S. Bell and R. Jackiw, Nuovo Cimento A **60**, 47-61 (1969).

[71] A. M. Bernstein and B. R. Holstein, Rev. Mod. Phys. **85**, 49 (2013).

[72] A. A. Burkov, J. Phys. Condens. Matter **27**, 113201 (2015).

[73] C. Fang, M. J. Gilbert, X. Dai, and B. A. Bernevig, Phys. Rev. Lett. **108**, 266802 (2012).

[74] M. V. Berry, Proc. R. Soc. Lond. A **392**, 45-57 (1984).

[75] A. C. Potter, I. Kimchi, and A. Vishwanath, Nat. Commun. **5**, 5161 (2014).

[76] P. J. W. Moll, N. L. Nair, T. Helm, A. C. Potter, I. Kimchi, A. Vishwanath, and J. G. Analytis, Nature **535**, 266-270 (2016).

[77] C. Zhang, A. Narayan, S. Lu, J. Zhang, H. Zhang, Z. Ni, X. Yuan, Y. Liu, J.-H. Park, E. Zhang, W. Wang, S. Liu, L. Cheng, L. Pi, Z. Sheng, S. Sanvito, and F. Xiu, Nat. Commun. **8**, 1272 (2017).

[78] H. Weng, C. Fang, Z. Fang, B. A. Bernevig, and X. Dai, Phys. Rev. X **5**, 011029 (2015).

[79] X. Huang, L. Zhao, Y. Long, P. Wang, D. Chen, Z. Yang, H. Liang, M. Xue, H. Weng, Z. Fang, X. Dai, and G. Chen, Phys. Rev. X **5**, 031023 (2015).

[80] N. Kiyohara, T. Tomita, and S. Nakatsuji, Phys. Rev. Applied **5**, 064009 (2016).

[81] H. Yang, Y. Sun, Y. Zhang, W.-J. Shi, S. S. P. Parkin, and B. Yan, New J. Phys. **19**, 015008 (2017).

[82] J. Liu and L. Balents, Phys. Rev. Lett. **119**, 087202 (2017).

[83] K. Deng, G. Wan, P. Deng, K. Zhang, S. Ding, E. Wang, M. Yan, H. Huang, H. Zhang, Z. Xu, J. Denlinger, A. Fedorov, H. Yang, W. Duan, H. Yao, Y. Wu, S. Fan, H. Zhang, X. Chen, and S. Zhou, Nat. Phys. **12**, 1105-1110 (2016).

[84] F. C. Chen, H. Y. Lv, X. Luo, W. J. Lu, Q. L. Pei, G. T. Lin, Y. Y. Han, X. B. Zhu, W. H. Song, and Y. P. Sun, Phys. Rev. B **94**, 235154 (2016).

[85] J. Jiang, Z. K. Liu, Y. Sun, H. F. Yang, C. R. Rajamathi, Y. P. Qi, L. X. Yang, C. Chen, C.-C. Hwang, S. Z. Sun, S.-K. Mo, I. Vobornik, J. Fujii, S. S. P. Parkin, C. Felser, B. H. Yan, and Y. L. Chen, Nat. Commun. **8**, 13973 (2017).

[86] D. Di Sante, P. K. Das, C. Bigi, Z. Ergönenc, N. Gürtler, J. A. Krieger, T. Schmitt, M. N. Ali, G. Rossi, R. Thomale, C. Franchini, S. Picozzi, J. Fujii, V. N. Strocov, G. Sangiovanni, I. Vobornik, R. J. Cava, and G. Panaccione, Phys. Rev. Lett. **119**, 026403 (2017).

[87] W. Zhang, Q. Wu, L. Zhang, S.-W. Cheong, A. A. Soluyanov, and W. Wu, Phys. Rev. B **96**, 165125 (2017).

[88] P. Li, Y. Wen, X. He, Q. Zhang, C. Xia, Z.-M. Yu, S. A. Yang, Z. Zhu, H. N. Alshareef, and X.-X. Zhang, Nat. Commun. **8**, 2150 (2017).

[89] K. Koepernik, D. Kasinathan, D. V. Efremov, S. Khim, S. Borisenko, B. Büchner, and J. van den Brink, Phys. Rev. B **93**, 201101(R) (2016).

[90] I. Belopolski, P. Yu, D. S. Sanchez, Y. Ishida, T.-R. Chang, S. S. Zhang, S.-Y. Xu, H. Zheng, G. Chang, G. Bian, H.-T. Jeng, T. Kondo, H. Lin, Z. Liu, S. Shin, and M. Z. Hasan, Nat. Commun. **8**, 942 (2017).

[91] E. Haubold, K. Koepernik, D. Efremov, S. Khim, A. Fedorov, Y. Kushnirenko, J. van den Brink, S. Wurmehl, B. Büchner, T. K. Kim, M. Hoesch, K. Sumida, K. Taguchi, T. Yoshikawa, A. Kimura, T. Okuda, and S. V. Borisenko, Phys. Rev. B **95**, 241108(R) (2017).

[92] G. Xu, H. Weng, Z. Wang, X. Dai, and Z. Fang, Phys. Rev. Lett. **107**, 186806 (2011).

[93] C. Fang, H. Weng, X. Dai, and Z. Fang, Chinese Phys. B **25**, 117106 (2016).

[94] L. S. Xie, L. M. Schoop, E. M. Seibel, Q. D. Gibson, W. Xie, and R. J. Cava, APL Materials **3**, 083602 (2015).

[95] Y.-H. Chan, C.-K. Chiu, M. Y. Chou, and A. P. Schnyder, Phys. Rev. B **93**, 2015132 (2016).

[96] T. Bzdušek, Q. Wu, A. Rüegg, M. Sigrist, and A. A. Soluyanov, Nature **538**, 75-78 (2016).

[97] R. Yu, Q. Wu, Z. Fang, and H. Weng, Phys. Rev. Lett. **119**, 036401 (2017).

[98] S. M. Young, S. Zaheer, J. C. Y. Teo, C. L. Kane, E. J. Mele, and A. M. Rappe, Phys. Rev. Lett. **108**, 140405 (2012).

[99] Z. Wang, Y. Sun, X.-Q. Chen, C. Franchini, G. Xu, H. Weng, X. Dai, and Z. Fang, Phys. Rev. B **85**, 195320 (2012).

[100] Z. K. Liu, B. Zhou, Y. Zhang, Z. J. Wang, H. M. Weng, D. Prabhakaran, S.-K. Mo, Z. X. Shen, Z. Fang, X. Dai, Z. Hussain, Y. L. Chen, Science **343**, 864-867 (2014).

[101] S.-Y. Xu, C. Liu, S. K. Kushwaha, R. Sankar, J. W. Krizan, I. Belopolski, M. Neupane, G. Bian, N. Alidoust, T.-R. Chang, H.-T. Jeng, C.-Y. Huang, W.-F. Tsai, H. Lin, P. P. Shibayev, F.-C. Chou, R. J. Cava, and M. Z. Hasan, Science **347**, 294-298 (2015).

[102] Z. K. Liu, J. Jiang, B. Zhou, Z. J. Wang, Y. Zhang, H. M. Weng, D. Prabhakaran, S.-K. Mo, H. Peng, P. Dudin, T. Kim, M. Hoesch, Z. Fang, X. Dai, Z. X. Shen, D. L. Feng, Z. Hussain, and Y. L. Chen, Nat. Mater. **13**, 677-681 (2014).

[103] Z. Wang, H. Weng, Q. Qu, X. Dai, and Z. Fang, Phys. Rev. B **88**, 125427 (2013).

[104] M. Kargarian, M. Randeria, and Y.-M. Lu, Proc. Natl. Acad. Sci. U.S.A. **113**, 8648 (2016).

[105] M. Kargarian, Y.-M. Lu, M. Randeria, arXiv:1712.03982 (2017).

[106] C. Le, X. Wu, S. Qin, Y. Li, R. Thomale, F. Zhang, and J. Hu, arXiv:1801.05719v1 (2018).

[107] C.-Z. Xu, Y.-H. Chan, Y. Chen, P. Chen, X. Wang, C. Dejoie, M.-H. Wong, J. A. Hlevyack, H. Ryu, H.-Y. Kee, N. Tamura, M.-Y. Chou, Z. Hussain, S.-K. Mo, and T.-C. Chiang, Phys. Rev. Lett. **118**, 146402 (2017).

[108] W. Cao, P. Tang, Y. Xu, J. Wu, B.-L. Gu, and W. Duan, Phys. Rev. B **96**, 115203 (2017).

[109] T.-R. Chang, S.-Y. Xu, D. S. Sanchez, W.-F. Tsai, S.-M. Huang, G. Chang, C.-H. Hsu, G. Bian, I. Belopolski, Z.-M. Yu, S. A. Yang, T. Neupert, H.-T. Jeng, H. Lin, and M. Z. Hasan, Phys. Rev. Lett. **119**, 026404 (2017).

[110] H. Huang, S. Zhou, and W. Duan, Phys. Rev. B **94**, 121117(R) (2016).

[111] N. P. Armitage, E. J. Mele and A. Vishwanath, Rev. Mod. Phys. **90**, 015001 (2018).

[112] M. Z. Hasan, S.-Y. Xu, I. Belopolski, and S.-M. Huang, Annu. Rev. Condens. Matter Phys. **8**, 289-309 (2017).

[113] A. Bansil, H. Lin, and T. Das, Rev. Mod. Phys. **88**, 021004 (2016).

[114] A. M. Turner and A. Vishwanath, *Topological Insulators* **6**, 293-324 (2013).

[115] S. Wang, B.-C. Lin, A.-Q. Wang, D.-P. Yu, and Z.-M. Liao, Advances in Physics: X **2**, 518-544 (2017).

[116] J. W. Villanova and K. Park, Phys. Rev. B **93**, 085122 (2016).

[117] L. Fu, Phys. Rev. Lett. **106**, 106802 (2011).

[118] H. Zhang, C.-X. Liu, and S.-C. Zhang, Phys. Rev. Lett. **111**, 066801 (2013).

[119] Z.-H. Zhu, C. N. Veenstra, G. Levy, A. Ubaldini, P. Syers, N. P. Butch, J. Paglione, M. W. Haverkort, I. S. Elfimov, and A. Damascelli, Phys. Rev. Lett. **110**, 216401 (2013).

[120] A. T. Lee, M. J. Han, and K. Park, Phys. Rev. B **90**, 155103 (2014).

[121] L. Miao, Z. F. Wang, M.-Y. Yao, F. Zhu, J. H. Dil, C. L. Gao, C. Liu, F. Liu, D. Qian, and J.-F. Jia, Phys. Rev. B **89**, 155116 (2014).

[122] H. Peng, K. Lai, D. Kong, S. Meister, Y. Chen, X.-L. Qi, S.-C. Zhang, Z.-X. Shen, and Yi Cui, Nat. Mat. **9**, 225 (2009).

[123] D. Kong, W. Dang, J. J. Cha, H. Li, S. Meister, H. Peng, Z. Liu, and Y. Cui, Nano Lett. **10**, 2245 (2010).

[124] Y. Zou, Z.-G. Chen, Y. Huang, L. Yang, J. Drennan, and J. Zou, J. Phys. Chem. C **118**, 20620 (2014).

[125] L. A. Jauregui, M. T. Pettes, L. P. Rokhinson, L. Shi, and Y. P. Chen, Sci. Rep. **5**, 8452 (2015).

[126] A. Zhuang, J.-J. Li, Y.-C. Wang, X. Wen, Y. Lin, B. Xiang, X. Wang, and J. Zeng, Angew. Chem. Int. Ed. **53**, 6425 (2014).

[127] C.-Y. Moon, J. Han, H. Lee, and H. J. Choi, Phys. Rev. B **84**, 195425 (2011).

[128] Z. Xu, X. Guo, M. Yao, H. He, L. Miao, L. Jiao, H. Liu, J. Wang, D. Qian, J. Jia, W. Ho, and M. Xie, Adv. Mat. **25**, 1557 (2013).

[129] F. Zhang, C. L. Kane, and E. J. Mele, Phys. Rev. B **86**, 081303(R) (2012).

[130] P. G. Silvestrov, P. W. Brouwer, and E. G. Mishchenko, Phys. Rev. B **86**, 075302 (2012).

[131] P.-H. Chang, F. Mahfouzi, N. Nagaosa, and B. K. Nikolić, Phys. Rev. B **89**, 195418 (2014).

[132] K. Momma and F. Izumi, J. Appl. Crystallogr. **44**, 1272-1276 (2011).

[133] S. Nakajima, J. Phys. Chem. Sol. **24**, 479 (1963).

[134] G. Kresse and D. Joubert, Phys. Rev. B **59**, 1758 (1999).

[135] K. Park, C. De Beule, and B. Partoens, New J. Phys. **15**, 113031 (2013).

[136] Y. A. Bychkov and E. I. Rashba, JETP Lett. **39**, 78 (1984).

[137] G. Dresselhaus, Phys. Rev. **100**, 580 (1955).

[138] C. H. Li, O. M. J. van 't Erve, J. T. Robinson, Y. Liu, L. Li, B. T. Jonker, Nature Nanotech. **9** 218 (2014).

[139] J. W. Villanova, E. Barnes, and K. Park, Nano Lett. **17**, 963-972 (2017).

[140] B.-J. Yang and N. Nagaosa, Nat. Commun. **5**, 4898 (2014).

[141] S. Murakami, New. J. Phys. **9**, 356 (2007).

[142] H. Li, H. He, H.-Z. Lu, H. Zhang, H. Liu, R. Ma, Z. Fan, S.-Q. Shen, and J. Wang, Nat. Commun. **7**, 10301 (2016).

[143] J. Xiong, S. K. Kushwaha, T. Liang, J. W. Krizan, M. Hirschberger, W. Wang, R. J. Cava, and N. P. Ong, Science **350**, 413-416 (2015).

[144] A. Chen and M. Franz, Phys. Rev. B **93**, 201105(R) (2016).

[145] F. Katmis, V. Lauter, F. S. Nogueira, B. A. Assaf, M. E. Jamer, P. Wei, B. Satpati, J. W. Freeland, I. Eremin, D. Heiman, P. Jarillo-Herrero, and J. S. Moodera, Nature **533**, 513-516 (2016).

[146] L. Fu and C. L. Kane, Phys. Rev. Lett. **100**, 096407 (2008).

[147] J. Hellerstedt, M. T. Edmonds, N. Ramakrishnan, C. Liu, B. Weber, A. Tadich, K. M. O'Donnell, S. Adam, and M. S. Fuhrer, Nano Lett. **16**, 3210 (2016).

[148] D. T. Son and B. Z. Spivak, Phys. Rev. B **88**, 104412 (2013).

[149] Y. Chen, S. Wu, and A. A. Burkov, Phys. Rev. B **88**, 125105 (2013).

[150] A. A. Zyuzin and A. A. Burkov, Phys. Rev. B **86**, 115133 (2012).

[151] S.-M. Huang, S.-Y. Xu, I. Belopolski, C.-C. Lee, G. Chang, B. Wang, N. Alidoust, G. Bian, M. Neupane, C. Zhang, S. Jia, A. Bansil, H. Lin, and M. Z. Hasan, Nat. Commun. **6**, 7373 (2015).

[152] A. Narayan, D. Di Sante, S. Picozzi, and S. Sanvito, Phys. Rev. Lett. **113**, 256403 (2014).

[153] J. Ruan, S.-K. Jian, H. Yao, J. Zhang, S.-C. Zhang, and D. Xing, Nat. Commun. **7**, 11136 (2016).

[154] Y. Sun, S.-C. Wu, and B. Yan, Phys. Rev. B. **92**, 115428 (2015).

[155] M. T. Edmonds, J. Hellerstedt, K. M. O'Donnell, A. Tadich, and M. S. Fuhrer, ACS Appl. Mater. Interfacs **8**, 16412-16418 (2016).

[156] G. Kresse and J. Furthmüller, Phys. Rev. B **54**, 11169 (1996).

[157] G. Kresse and J. Furthmüller, Comp. Mat. Sci. **6**, 15-50 (1996).

[158] J. P. Perdew, K. Burke, and M. Ernzerhof, Phys. Rev. Lett. **77**, 3865 (1996).

[159] G. Kresse and D. Joubert, Phys. Rev. B **59**, 1758 (1999).

[160] E. V. Gorbar, V. A. Miransky, I. A. Shovkovy, and P. O. Sukhachov, Phys. Rev. B **91**, 235138 (2015).

[161] X. Cheng, R. Li, Y. Sun, X.-Q. Chen, D. Li, and Y. Li, Phys. Rev. B **89**, 245201 (2014).

[162] G. Z. Jenkins, C. Lane, B. Barbiellini, A. B. Sushkov, R. L. Carey, F. Liu, J. W. Krizan, S. K. Kushwaha, Q. Gibson, T.-R. Chang, H.-T. Jeng, H. Lin, R. J. Cava, A. Bansil, and H. D. Drew, Phys. Rev. B **94**, 085121 (2016).

[163] Y. Zhang, Z. Liu, B. Zhou, Y. Kim, Z. Hussain, Z.-X. Shen, Y. Chen, and S.-K. Mo, Appl. Phys. Lett. **105**, 031901 (2014).

[164] S.-Y. Xu, C. Liu, I. Belopolski, S. K. Kushwaha, R. Sankar, J. W. Krizan, T.-R. Chang, C. M. Polley, J. Adell, T. Balasubramanian, K. Miyamoto, N. Alidoust, G. Bian, M. Neupane, H.-T. Jeng, C.-Y. Huang, W.-F. Tsai, T. Okuda, A. Bansil, F. C. Chou, R. J. Cava, H. Lin, and M. Z. Hasan, Phys. Rev. B **92**, 075115 (2015).

[165] K. Park, C. De Beule, and B. Partoens, New. J. Phys. **15**, 113031 (2013).

[166] K. Govaerts, J. Park, C. De Beule, B. Partoens, and D. Lamoen, Phys. Rev. B **90**, 155123 (2014).

[167] L. Miao, Z. F. Wang, W. Ming, M.-Y. Yao, M. Wang, F. Yang, Y. R. Song, F. Zhu, A. V. Fedorov, Z. Sun, C. L. Gao, C. Liu, Q.-K. Xue, C.-X. Lin, F. Liu, D. Qian, and J.-F. Jia, Proc. Natl. Acad. Sci. U.S.A. **110**, 2758 (2013).

[168] M. N. Ali, Q. Gibson, S. Jeon, B. B. Zhou, A. Yazdani, and R. J. Cava, Inorg. Chem. **53**, 4062 (2014).

[169] T. Liang, Q. Gibson, M. N. Ali, M. Liu, R. J. Cava, and N. P. Ong, Nat. Mater. **14**, 280 (2015).

[170] W.-Y. Shan, H.-Z. Lu, and S.-Q. Shen, New. J. Phys. **12**, 043048 (2010).

[171] C. Fang, M. J. Gilbert, X. Dai, and B. A. Bernevig, Phys. Rev. Lett. **108**, 266802 (2012).

[172] G. Sharma, P. Goswami, and S. Tewari, Phys. Rev. B **93**, 035116 (2016).

[173] Y. Zhang, D. Bulmash, P. Hosur, A. C. Potter, and A. Vishwanath, Sci. Rep. **6**, 23741 (2016).

[174] L. X. Yang, Z. K. Liu, Y. Sun, H. Peng, H. F. Yang, T. Zhang, B. Zhou, Y. Zhang, Y. F. Guo, M. Rahn, D. Prabhakaran, Z. Hussain, S.-K. Mo, C. Felser, B. Yan, and Y. L. Chen, Nat. Phys. **11**, 728-732 (2015).

[175] J. Cano, B. Bradlyn, Z. Wang, M. Hirschberger, N. P. Ong, and B. A. Bernevig, Phys. Rev. B **95**, 161306(R) (2017).

[176] Z. Wang, Y. Sun, X.-Q. Chen, C. Franchini, G. Xu, H. Weng, X. Dai, and Z. Fang, Phys. Rev. B **85**, 195320 (2012).

[177] J. C. Slater and G. F. Koster, Phys. Rev. **94**, 1498 (1954).

[178] M. P. López Sancho, J. M. López Sancho, and J. Rubio, J. Phys. F: Met. Phys. **15**, 851-858 (1985).

[179] D. Gosálbez-Marínez, I. Souza, and D. Vanderbilt, Phys. Rev. B **92**, 085138 (2015).

[180] Q. Wu, S. Zhang, H.-F. Song, M. Troyer, and A. A. Soluyanov, Comput. Phys. Commun. **224**, 405-416 (2017).

[181] W. Zhang, R. Yu, H.-J. Zhang, X. Dai, and Z. Fang, New J. Phys. **12** 065013 (2010).

[182] S. Jeon, B. B. Zhou, A. Gyenis, B. E. Feldman, I. Kimchi, A. C. Potter, Q. D. Gibson, R. J. Cava, A. Vishwanath, and A. Yazdani, Nat. Mat. **13**, 851-856 (2014).

[183] P. Giannozzi *et al*, J. of Physics: Condens. Matt. **29**, 465901 (2017).

[184] E. Küçükbenli, M. Monni, B. I. Adetunji, X. Ge, G. A. Adebayo, N. Marzari, S. de Gironcoli, and A. Dal Corso, arXiv:1404.3015 (2014).

[185] A. A. Zyuzin, M. D. Hook, and A. A. Burkov, Phys. Rev. B **83**, 245428 (2011).

[186] S. S. Pershoguba and V. M. Yakovenko, Phys. Rev. B **86**, 165404 (2012).

[187] F. D. M. Haldane, arXiv:1401.0529v1 (2014).

[188] Á. González, Math Geosci. **42**, 49-64 (2010).

[189] R. Swinbank and R. J. Purser, Q. J. R. Meteorol. Soc. **132**, 1769-1793 (2006).

[190] M. K. Arthur, Army Research Laboratory, Tech. Rep. ARL-TR-7333 (2015).

Appendices

Appendix A

A.1 Rotation of Spinors about an Axis

It is necessary to develop the matrix representation of a rotation about an axis in the basis of states with definite angular momentum. This is crucial for using the *method of invariants* to develop the terms allowed in a model Hamiltonian; this is well-developed by Liu *et al.* [60] when the rotation axis is the z-axis, but it is perhaps less obvious when the rotation axis does not coincide with the z-axis yet one prefers to work in the basis of states specified by $|j, m_j\rangle$ (e.g. Cd_3As_2).

A.1.1 Wigner D-matrix

For a particular angular-momentum (j) sub-block of the Hamiltonian, the rotation matrix about associated with a particular axis and angle is simply given by $R_{\hat{n}}(\theta) = e^{-i\theta\hat{n}\cdot\vec{J}}$. But this is in general difficult to compute by hand in a specific basis since the angular momentum matrices are non-commuting. We can instead write this as a series of rotations about different axes, noting that we would like to stay in the basis of states $|j, m_j\rangle$. We choose the succession of axes as z-y-z so that $R_{\hat{n}}(\theta) = e^{-i\alpha J_z}e^{-i\beta J_y}e^{-i\gamma J_z}$, and the exterior matrices are easy to evaluate since their eigenvalues are already encoded in the choice of basis. What is left is the middle matrix dependent on J_y, as below.

$$\begin{aligned}\langle j, m'|R|j, m\rangle &= \langle j, m'|e^{-i\alpha J_z}e^{-i\beta J_y}e^{-i\gamma J_z}|j, m\rangle \\ &= e^{-im'\alpha}\langle j, m'|e^{-i\beta J_y}|j, m\rangle e^{-im\gamma} \\ &= e^{-im'\alpha}d^j_{m',m}(\beta)e^{-im\gamma},\end{aligned} \tag{A.1}$$

The set $\{\alpha, \beta, \gamma\}$ are the associated *Euler angles*, and will be related to the axis of rotation but perhaps in a complicated fashion. $d^j_{m',m}(\beta)$ is the Wigner D-matrix, which contains all that complicated dependency relating our basis to that middle matrix dependent on J_y. Happily, Wigner calculated this matrix:

$$d^j_{m',m}(\beta) = \sqrt{(j+m')!(j-m')!(j+m)!(j-m)!} \times \sum_{s=0}^{s^*} \frac{(-1)^{m'-m+s}(\cos(\frac{\beta}{2}))^{2j+m-m'-2s}(\sin(\frac{\beta}{2}))^{m'-m+2s}}{s!(j+m-s)!(m'-m+s)!(j-m'-s)!}, \quad \text{(A.2)}$$

where the sum over s goes over only those values that keep all of the factorials in the denominator nonnegative. Thus there is a maximum value for s, s^*, over which the sum is performed. Practically speaking, it is easier to populate the rotation matrix if one keeps $m' > m$, and then uses the following properties to populate the rest of the matrix:

$$\begin{aligned} d^j_{m',m} &= (-1)^{m-m'} d^j_{m,m'} \\ d^j_{m',m} &= d^j_{-m,-m'} \end{aligned} \quad \text{(A.3)}$$

Now since we have the Wigner D-matrix the only thing we need is the set of Euler Angles, $\{\alpha, \beta, \gamma\}$, for the rotation matrix $R_{\hat{n}}(\theta)$. This is given by the *Rodrigues rotation formula* around an axis specified by a unit vector $\hat{n} = n_x\hat{x} + n_y\hat{y} + n_z\hat{z}$:

$$R_{\hat{n}}(\theta) = \begin{pmatrix} n_x^2(1-\cos\theta)+\cos\theta & n_xn_y(1-\cos\theta)-n_z\sin\theta & n_xn_z(1-\cos\theta)+n_y\sin\theta \\ n_xn_y(1-\cos\theta)+n_z\sin\theta & n_y^2(1-\cos\theta)+\cos\theta & n_xn_y(1-\cos\theta)-n_x\sin\theta \\ n_xn_z(1-\cos\theta)-n_y\sin\theta & n_yn_z(1-\cos\theta)+n_x\sin\theta & n_z^2(1-\cos\theta)+\cos\theta \end{pmatrix}, \quad \text{(A.4)}$$

Now Eq. (A.4) is to be compared to the Euler angle prescription,

$$\begin{aligned} R_{\hat{n}}(\theta) &= R_z(\alpha)R_y(\beta)R_z(\gamma) \\ &= \begin{pmatrix} \cos\alpha\cos\beta\cos\gamma - \sin\alpha\sin\gamma & -\sin\alpha\cos\gamma - \cos\alpha\cos\beta\sin\gamma & \cos\alpha\sin\beta \\ \sin\alpha\cos\beta\cos\gamma + \cos\alpha\sin\gamma & \cos\alpha\cos\gamma - \sin\alpha\cos\beta\sin\gamma & \sin\alpha\sin\beta \\ -\sin\beta\cos\gamma & \sin\beta\sin\gamma & \cos\beta \end{pmatrix}, \end{aligned} \quad \text{(A.5)}$$

and so the set $\{\alpha, \beta, \gamma\}$ can be extracted by comparison. Because the rotation matrix for the angle γ acts on the state first, one should choose $\gamma \in [-\pi, \pi] \neq 0$ before choosing α. Armed with the Euler angles, the answer is immediately found from Eq. (A.1).

A.1.2 An Example for Cd_3As_2

Among the bulk symmetries of the Dirac semimetal Cd_3As_2 which one must consider when building the four-band model Hamiltonian is a threefold rotation around the [111] crystallographic direction [175], $C_{3,[111]}$ or $R_{[111]}(\frac{2\pi}{3})$. The four-band basis consists of the states $\{|\frac{3}{2}, +\frac{3}{2}\rangle, |\frac{3}{2}, +\frac{1}{2}\rangle, |\frac{3}{2}, -\frac{1}{2}\rangle, |\frac{3}{2}, -\frac{3}{2}\rangle\}$.

Using the Rodrigues formula for $\hat{n} = \frac{1}{\sqrt{3}}(\hat{x} + \hat{y} + \hat{z})$ gives

$$R_{[111]}\left(\tfrac{2\pi}{3}\right) = \begin{pmatrix} 0 & 0 & 1 \\ 1 & 0 & 0 \\ 0 & 1 & 0 \end{pmatrix} \tag{A.6}$$

from which we identify the Euler angles $\{\alpha = 0, \beta = \frac{\pi}{2}, \gamma = \frac{\pi}{2}\}$. The Wigner D-matrix elements (with $s^* = \{0, 1\}$ for $m' = \{\frac{3}{2}, \frac{1}{2}\}$, respectively) are:

$$\begin{aligned}
d^{3/2}_{\frac{3}{2},\frac{3}{2}}(\beta) &= \cos^3(\frac{\beta}{2}) \\
d^{3/2}_{\frac{3}{2},\frac{1}{2}}(\beta) &= -\sqrt{3}\cos^2(\frac{\beta}{2})\sin(\frac{\beta}{2}) \\
d^{3/2}_{\frac{3}{2},\frac{-1}{2}}(\beta) &= \sqrt{3}\cos(\frac{\beta}{2})\sin^2(\frac{\beta}{2}) \\
d^{3/2}_{\frac{3}{2},\frac{-3}{2}}(\beta) &= -\sin^3(\frac{\beta}{2}) \\
d^{3/2}_{\frac{1}{2},\frac{1}{2}}(\beta) &= \frac{1}{2}(3\cos\beta - 1)\cos(\frac{\beta}{2}) \\
d^{3/2}_{\frac{1}{2},\frac{-1}{2}}(\beta) &= -\frac{1}{2}(3\cos\beta + 1)\sin(\frac{\beta}{2})
\end{aligned} \tag{A.7}$$

Plugging $\beta = \frac{\pi}{2}$ into Eq. (A.7): $d^{3/2}_{\frac{3}{2},\frac{3}{2}} = \frac{\sqrt{2}}{4}$, $d^{3/2}_{\frac{3}{2},\frac{1}{2}} = -\sqrt{3}\frac{\sqrt{2}}{4}$, $d^{3/2}_{\frac{3}{2},\frac{-1}{2}} = \sqrt{3}\frac{\sqrt{2}}{4}$, $d^{3/2}_{\frac{3}{2},\frac{-3}{2}} = -\frac{\sqrt{2}}{4}$, $d^{3/2}_{\frac{1}{2},\frac{1}{2}} = -\frac{\sqrt{2}}{4}$, and $d^{3/2}_{\frac{1}{2},\frac{-1}{2}} = -\frac{\sqrt{2}}{4}$.

So using the properties of the Wigner D-matrix in Eq. (A.3), and factoring out $e^{-i\pi/4}$ from the factor $e^{-im\gamma}$, one arrives at the matrix representation,

$$C_{3,[111]} = \frac{\sqrt{2}}{4}e^{-i\pi/4}\begin{pmatrix} -i & -\sqrt{3} & i\sqrt{3} & 1 \\ -i\sqrt{3} & -1 & -i & -\sqrt{3} \\ -i\sqrt{3} & 1 & -i & \sqrt{3} \\ -i & \sqrt{3} & i\sqrt{3} & -1 \end{pmatrix}. \tag{A.8}$$

Now one can use this in the method of invariants to find those terms which are allowed in the Hamiltonian by this symmetry. That is by satisfying the statement,

$$C_{3,[111]}H(\vec{k})C^{-1}_{3,[111]} = H(R_{[111]}\left(\tfrac{2\pi}{3}\right)\vec{k})$$

or

$$C_{3,[111]}H(k_x, k_y, k_z)C^{-1}_{3,[111]} = H(k_z, k_x, k_y), \tag{A.9}$$

if one replaces the active rotation matrix with that from Eq. (A.6).

A.2 A Program to Uniformly Sample a Sphere

We determine the chiral charge of Weyl nodes by enclosing each in spheres of successively smaller radius and calculating the Berry Curvature flux,

$$\chi_n = \frac{1}{2\pi} \oint_S dS \; \hat{\boldsymbol{n}} \cdot \boldsymbol{\Omega}_n(\boldsymbol{k}). \tag{A.10}$$

We perform the surface integral numerically by selecting points which are separated by a fixed, irrational distance along a spiral connecting the poles of a sphere centered on the Weyl node. This provides a nearly uniformly sampled sphere [188–190] without having to perform Monte Carlo integration for a large number of samples (it is just not practical to apply Monte Carlo integration in two dimensions, requiring one million points to reduce the standard deviation to an acceptable range).

We used spheres with varying numbers of points ($3{\cdot}10^3$,$\cdot 10^4$,$\cdot 10^5$) and found that a sphere with $N{=}3{\cdot}10^4$ was an excellent compromise of speed and precision. Hence we calculated the Berry Curvature at each point on a sphere of fixed radius which is small enough to enclose only each Weyl point and no others. Upon assigning each point on the sphere a uniform area, $\frac{4\pi R^2}{N}$, the surface integral of Equation A.10 is easily numerically evaluated.

```
NMAX = 3001;
```

In[22]:=
```
node = Table[{0, 0, 0}, {i, 1, NMAX - 1}];
dlong = Pi * (3 - Sqrt[5]);
dz = 2. / NMAX;
long = 0.;
zee = (1. - dz / 2.);
For[k = 0, k ≤ (NMAX - 1), k++,
  ruff = Sqrt[1 - zee * zee];
  node[[k, 1]] = Cos[long] * ruff;
  node[[k, 2]] = Sin[long] * ruff;
  node[[k, 3]] = zee;
  zee = zee - dz;
  long = long + dlong;
 ];
Graphics3D[Point[node], Axes → True, AxesLabel → {"x", "y", "z"}]
Export["3001_unif-unitsphere.tab", node, "Table"]
```

Out[28]=

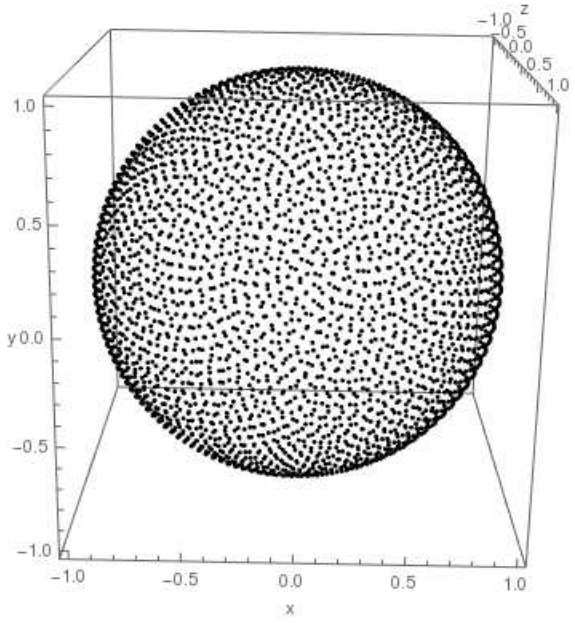

Out[29]= 3001_unif-unitsphere.tab